Endoscopic Fiber-Based Chemiluminescence Diagnostics in Real-Scale High-Pressure Gas Turbine Combustor Test Rigs

Von der Fakultät für Ingenieurwissenschaften,
Abteilung Maschinenbau und Verfahrenstechnik
der
Universität Duisburg-Essen

zur Erlangung des akademischen Grades
eines
Doktors der Ingenieurwissenschaften
Dr.-Ing.

genehmigte Dissertation

von

Simon Görs
aus
Herdecke

Gutachter: Prof. Dr. rer. nat. Christof Schulz
Prof. Dr.-Ing. Alois Herkommer

Tag der mündlichen Prüfung: 16.12.2022

Abstract

The combustion system of modern gas turbines has to meet a large number of requirements, diametrically opposed in some cases, and are therefore intensely investigated in elaborate high-pressure tests. The associated effort and costs are immense; thus it is desired to achieve the highest possible information density during each test. The optical measurement techniques used to date to increase information density are regularly based on optical access to the combustion chamber by means of rigid probes, which were specifically designed for each specific application and are therefore difficult to apply to different test rigs and difficult to adapt to other measurement methods. Consequently, in this thesis a modular, fiber-based flexible endoscopic probe was developed to enable optical access to various test rig configurations, allowing for a more frequent use of optical measurement techniques. Due to its robustness and simplicity, chemiluminescence imaging was selected as optical measurement technique and the probe developed on this basis. The probe has been successfully operated on consecutive days at pressures up to 1.6 MPa and temperatures of 750 K at air mass flow rates of 32.5 kg/s. As a result of the modular design concept, the probe was also successfully utilized in wall temperature measurements in studies by Nau et al.

Chemiluminescence imaging measurements were carried out at three different test rigs, namely the NDP-1, the HBK-4, and the CEC under atmospheric (NDP-1) or high-pressure conditions. For each measurement, the signal was filtered for OH^* or CH^*, respectively, via the corresponding band-pass filters.

Some measurements were directed at investigating the flame length and flame position inside the combustion chamber. For this purpose, a post-processing routine was developed to identify the flame within the recorded chemiluminescence images, combining the thresholding method developed by Otsu with calculations of the image entropy to identify the optimal threshold that most accurately characterizes the flame object. The optimal threshold met the constrains of the lowest standard deviation of the calculated flame length and highest image entropy at the transition region between flame and background. The routine was found to reliably detect the flame within the images even for poor SNR. In addition, statistical evaluations of the flame length or its standard deviation and of the CO or NO_x emission were performed. Moreover, the flame of an additional fuel stage downstream of the main stage flame was visualized for the first time in a high-pressure single combustor test.

For the investigation of the spatial origin of flame-induced oscillations, measurements were performed using high-speed imaging. A post-processing routine used a signal-analytical approach, i.e., coherence analysis, to determine the correlation between the chemiluminescence intensity fluctuations and the pressure fluctuations and to avoid misinterpretation of intensity fluctuations within the chemiluminescence signal. By dividing each image into a set of submatrices and analyzing the images submatrix-wise, the routine enables the spatial identifications of regions of high coherence, indicating a strong coupling between pressure and chemiluminescence intensity fluctuations as a marker for heat release fluctuations. The studies performed at atmospheric conditions at the NDP-1 indicated CH^* as a more suitable marker for the heat release rate than OH^* under the given experimental conditions.

The modularity of the probe design was demonstrated by using the probe for wall-temperature measurements using thermographic phosphors.

Zusammenfassung

Das Verbrennungssystem moderner Gasturbinen muss eine Vielzahl von zum Teil diametral entgegengesetzten Anforderungen erfüllen und wird daher in aufwändigen Hochdruckversuchen intensiv untersucht. Der damit verbundene Aufwand und die Kosten sind immens, daher ist es erwünscht, bei jedem Test eine möglichst hohe Informationsdichte zu erreichen. Die bisher eingesetzten optischen Messverfahren zur Erhöhung der Informationsdichte basieren regelmäßig auf dem optischen Zugang durch starrer Sonden, die speziell für die jeweilige konzipiert wurden und daher nur schwer auf unterschiedliche Prüfstände übertragbar und an andere Messverfahren adaptierbar sind. Daher wurde eine modulare, faserbasierte, flexible endoskopische Sonde entwickelt, die den optischen Zugang zu verschiedenen Prüfstandskonfigurationen ermöglicht und damit eine häufigere Anwendung optischer Messtechniken erlaubt. Aufgrund ihrer Robustheit und Einfachheit wurde die Chemilumineszenz-Bildgebung als optische Messtechnik ausgewählt und die Sonde auf dieser Grundlage entwickelt. Die Sonde wurde an aufeinanderfolgenden Tagen erfolgreich bei Drücken bis zu 1,6 MPa und Temperaturen von 750 K bei Luftmassenströmen von 32,5 kg/s betrieben. Aufgrund des modularen Konzepts konnte die Sonde auch erfolgreich für Wandtemperaturmessungen in Studien von Nau et al. Eingesetzt werden.

Bildgebende Chemilumineszenzmessungen wurden an drei verschiedenen Prüfständen, nämlich dem NDP-1, dem HBK-4 und dem CEC, unter atmosphärischen (NDP-1) oder Hochdruckbedingungen durchgeführt. Bei jeder Messung wurde das Signal mit entsprechenden Bandpassfiltern zur Selektion von OH^* bzw. CH^* gefiltert.

Einige Messungen dienten der Untersuchung der Flammenlänge und der Flammenposition innerhalb der Brennkammer. Zu diesem Zweck wurde eine Nachbearbeitungsroutine zur Identifizierung des Flammenobjekts in den aufgenommenen Chemilumineszenzbildern entwickelt, die die von Otsu eingeführte Schwellenwertmethode mit Berechnungen der Bildentropie kombiniert, um den optimalen Schwellenwert zu ermitteln, welcher das Flammenobjekt am besten charakterisiert. Der optimale Schwellenwert erfüllte die Bedingungen der geringsten Standardabweichung der berechneten Flammenlänge und der höchsten Bildentropie im Übergangsbereich zwischen Flamme und Hintergrund. Es wurde festgestellt, dass die Routine das Flammenobjekt in den Bildern auch bei schlechtem SNR zuverlässig erkennt. Darüber hinaus wurden statistische Auswertungen der Flammenlänge bzw. deren Standardabweichung und der CO-

bzw. NO_x-Emissionen durchgeführt. Außerdem wurde die Flamme einer zusätzlichen Brennstoffstufe unterhalb der Hauptstufenflamme erstmals in einem Hochdruck-Einzelbrennertest visualisiert.

Zur Untersuchung des räumlichen Ursprungs der flammeninduzierten Oszillationen wurden Messungen als Hochgeschwindigkeitsaufnahmen durchgeführt. Die entwickelte Nachbearbeitungsroutine nutzte einen signalanalytischen Ansatz, die Kohärenzanalyse, um die Korrelation zwischen den Chemilumineszenz-Intensitätsschwankungen und den Druckschwankungen zu bestimmen und eine Fehlinterpretation der Intensitätsschwankungen innerhalb des Chemilumineszenzsignals zu vermeiden. Indem jedes Bild in eine Reihe von Submatrizen unterteilt und die Bilder submatrixweise analysiert werden, ermöglicht die Routine die räumliche Identifizierung von Regionen hoher Kohärenz, was auf eine starke Kopplung zwischen Druck- und Chemilumineszenz-Intensitätsschwankungen, die als Marker für Wärmefreisetzungsschwankungen dienen, hindeutet. Die unter atmosphärischen Bedingungen am NDP-1 durchgeführten Studien zeigen, dass CH^* unter den gegebenen experimentellen Bedingungen ein besser geeigneter Marker für die Wärmefreisetzungsrate ist.

Die Modularität des entwickelten Sondenkonzepts konnte durch den Einsatz der Sonde bei der Messung der Wandtemperatur mit thermografischen Phosphoren demonstriert werden.

Acknowledgement

The work presented in this thesis has been carried out during my time at the Institute for Combustion and Gas Dynamics – Reactive Fluids at the University of Duisburg-Essen. I would like to express my gratitude to Prof. Dr. Christof Schulz for giving me the opportunity to work under his supervision and for his patience as well as to Prof. Dr. Herkommer for acting as the second examiner. I also would like to thank Dr. Torsten Endres for his support during my work and the many inspiring discussions. I'm also thankful for his and Dr. Erdal Akyildiz' tremendous support during the measurement campaigns, literally from dusk till dawn, and beyond. Furthermore, I am grateful as well as to Dr. Matthias Beuting and Dr. Philipp Niegemann, for your friendship.

Another very special thanks goes to Dr. Benjamin Witzel, without his support a probe would probably never have seen the inside of a test rig. You were nothing less than a mentor to me during my doctoral studies. I also owe a special thanks to André and Martin from the Siemens Clean Energy Center for their tireless efforts way beyond duty during the time-consuming preparation for the final measurements. This also applies to Gabriel Rodriguez-Vega, who was willing to properly mess up the schedule of the high-pressure measurements for me. Furthermore, I would like to thank my other former Siemens colleagues such as Alexander Rambach and Dr. Lars Terjung for the recommissioning of the NDP-1 as well as Martin Lenze and Stephan Buch for their support of the pressure vessel modifications. This also includes Dr. Boris F. Kock, without whom I probably would never have established the good connection to Siemens. This also applies to the team of the mechanical workshop of the University of Duisburg-Essen and especially to Michael Eisenhut, who had to save the quite tight schedules by his support more often than either one of us had hoped.

I would also like to thank my former students Abbas El Moussawi, André Müller, Jonathan Schöler, and Jize Sun, whose supervision I have never regretted and whose work is an important part of this thesis. Another heartfelt thank you goes to all my former colleagues at the university, especially the knights of the morning coffee table like Dr. Mustafa Fikri, Dieter Hermanns, Dr. Jürgen Herzler, Ludger Jerig, Dr. Sebastian Peukert, Dr. Paul Sela, Dr. Ralf Starke, and Dr. Siavash Zabeti. Markus Röder and Apl. Prof. Dr. Thomas Dreier also deserve special thanks for the careful familiarization at the beginning of my work. I would also like to thank the good soul of the Institute, Mrs. Barbara Nota.

Finally, I would like to thank my wife for her understanding, unwavering support and motivation.

Table of Content

Nomenclature

Latin symbols

Symbol	Unit	Description
A	m^2	Flame area
$\boldsymbol{A}$	pixel	Image submatrix
A	-	Reactant
AB	-	Reaction intermediate
B	-	Reactant
C	-	Product
C	-	Threshold class within an image
c	J kg^{-1} K^{-1}	Specific heat capacity
c	m s^{-1}	Speed of light
D	-	Damköhler number
D	-	Product
D	m^2 s^{-1}	Thermal diffusivity
D_B	pixel	Burner diameter in image space
$\mathcal{F}$	-	Fourier transformation
f	mm	Focal length
f	Hz	Frequency
H	-	Image entropy
h	Js	Plank's constant
$\boldsymbol{Im}$	pixel	Image matrix
I	-	Intensity
k	-	Threshold level
k_f	mol cm^{-3} s^{-1}	Reaction rate
$\overline{k}$		Turbulent kinetic energy
Ka	-	Karlovitz number
l	mm	Length
l_F	mm	Flame length
l_f	-	Normalized flame length
$\dot{m}$	kg s^{-1}	Mass flow

n	-	Refraction index
P	-	Products
P	-	Probability of pixels at gray level
p	Pa	Pressure
R	-	Cross-correlation
r	m	Radius
Re	-	Reynolds number
S	-	Spectral density
s	m s^{-1}	Flame speed
T	K	Temperature
T	s	Time period
t	s	Time
V	m^3	Volume
w	pixel	Image matrix size
x	pixel	Image *x*-coordinate
y	pixel	Image *y*-coordinate
Y	-	Mass fraction
Z	-	Mixture fraction

Greek symbols

Symbol	Dimension	Description
γ^2	-	Coherence
ε	-	Discriminant criterion
$\bar{\varepsilon}$	m s^{-3}	Eddy dissipation rate
η	m	Kolmogorov length
λ	-	Air factor (ϕ^{-1})
λ	nm	Wavelength
ν	-	Stoichiometric coefficient
ν	Hz	Photon frequency
ρ	kg m^{-3}	Density
σ^2	-	Standard deviation
σ_B	-	Between-class variance
σ_T	-	Total variance
τ	s	time
ϕ	-	Equivalence ratio (λ^{-1})

Superscripts

*	Electronically excited state
$+$	Optimal
$'$	Reactants
$'$	Fluctuation value

$''$	Products
$\bar{}$	Mean value

Subscripts

b	Burned state
c	Chemical
CL	Chemiluminescence
F	Flame
f	Fuel
HR	Heat release
Im	Image
L	Laminar
max	Maximum
n	Normal direction
ox	Oxidizer
p	Pressure
per	Period
st	Stoichiometric
T	Turbulent
Th	Thermal
u	Unburned state
u, st	Unburned stoichiometric state

Abbreviations

3D	3-dimensional
BP	Band-pass filter
CAR	Cooling-air reduced combustion chamber
CARS	Coherent anti-Stokes Raman spectroscopy
CBO	Cylindrical burner outlet
CCD	Charge-coupled device
CEC	Clean Energy Center
CFD	Computational fluid dynamics
CHT	Circular Hough transformation
CMOS	Complementary metal oxide semiconductor
CTC	Computed tomography of chemiluminescence
DGV	Doppler global velocimetry
DLR	Deutsches Zentrum für Luft- und Raumfahrt
DNS	Direct numerical simulation
FOV	Field of view
FRS	Filtered Rayleigh scattering
GGI	General grid interfaces

GT	Gas turbine
HBK-4	Hochdruck-Brennkammer-Prüfstand 4
HFD	High frequency dynamics
IRO	Intensified relay optics
LDV	Laser Doppler velocimetry
LIF	Laser-induced fluorescence
LII	Laser-induced incandescence
LoS	Line of sight
PDV	Phase Doppler velocimetry
PIV	Particle image velocimetry
SNR	Signal-to-noise ratio
TBC	Thermal barrier coating
TDC	Top dead center
TIT	Turbine inlet temperature
ULN	Ultra-low NO_x
UV	Ultraviolet

1 Introduction

1.1 Challenges for Gas Turbine Combustion

The world's demand for electricity is continuously increasing and an annual growth of 2.1 % up to 2040 is expected in some scenarios, reaching more than 40,000 TWh in total, wherein the installed capacity of gas turbines (GTs) may grow from the currently 6,000 to 9,000 TWh (stated policy scenario), as shown in Figure 1.1.

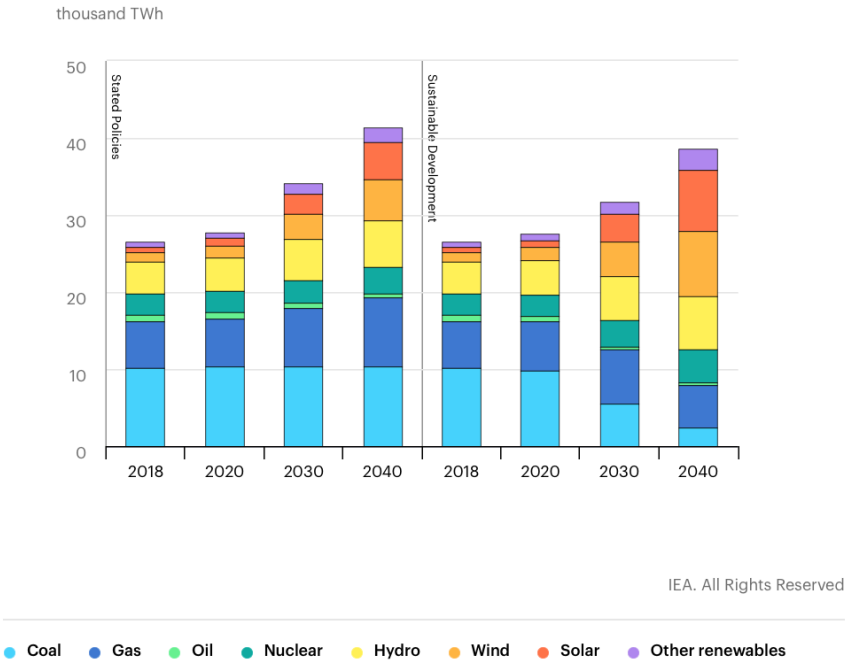

Figure 1.1: Predicted gross electricity production in OECD countries 2018–2040 by source for the stated policy scenario (left) and for the sustainable development (right) [1].

Due to this growing demand for electricity, the transition towards renewable energy sources, decarbonization, and the simultaneous increase in the effects of climate change, the requirements for the combustion systems of stationary gas turbines (GTs) are becoming increasingly

complex. In essence, the global gas turbine market is demanding improvements in terms of power output, full- and part-load efficiency, emissions, fuel flexibility, operational flexibility such as start-up time, ramping rates and turndown capability, and specific cost (€/kW). All these demands increase the complexity of the combustion system development process, e.g., due to diametrically opposed requirements. For example, the operation range of a stationary GT is defined by the allowed carbon monoxide (CO) and nitrogen oxides (NO_x) emission limits, as presented in Figure 1.2.

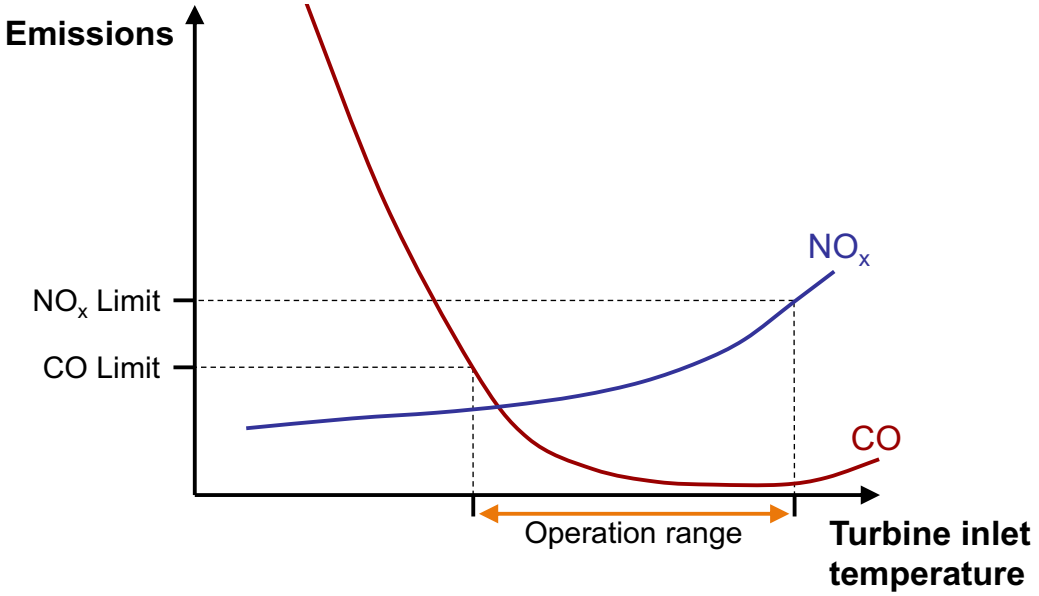

Figure 1.2: Schematic illustration of the operation range of a gas turbine, confined by the emission limits for CO and NO_x [2].

The turbine inlet temperature is correlated to the load of the GT and is strongly affected by the flame temperature. As it can be seen from the figure, the CO increases with a decreasing flame temperature as the NO_x emissions increase with higher flame temperatures. In particular, the reduction of NO_x emission was subject of the development of GT combustion systems in the past. The production of NO_x strongly correlates with the flame temperature and the residence time in hot areas, thus the combustion system was changed from elongated combustion chambers equipped with diffusion burners to compact combustion chambers with premix burners. To achieve low NO_x emission, these systems are operated at lean and thoroughly premixed fuel/air conditions. In consequence, the combustion systems are characterized by their compact design, high turbulent flows and high-power densities. This development is shown in Figure 1.3 for Siemens gas turbine combustors.

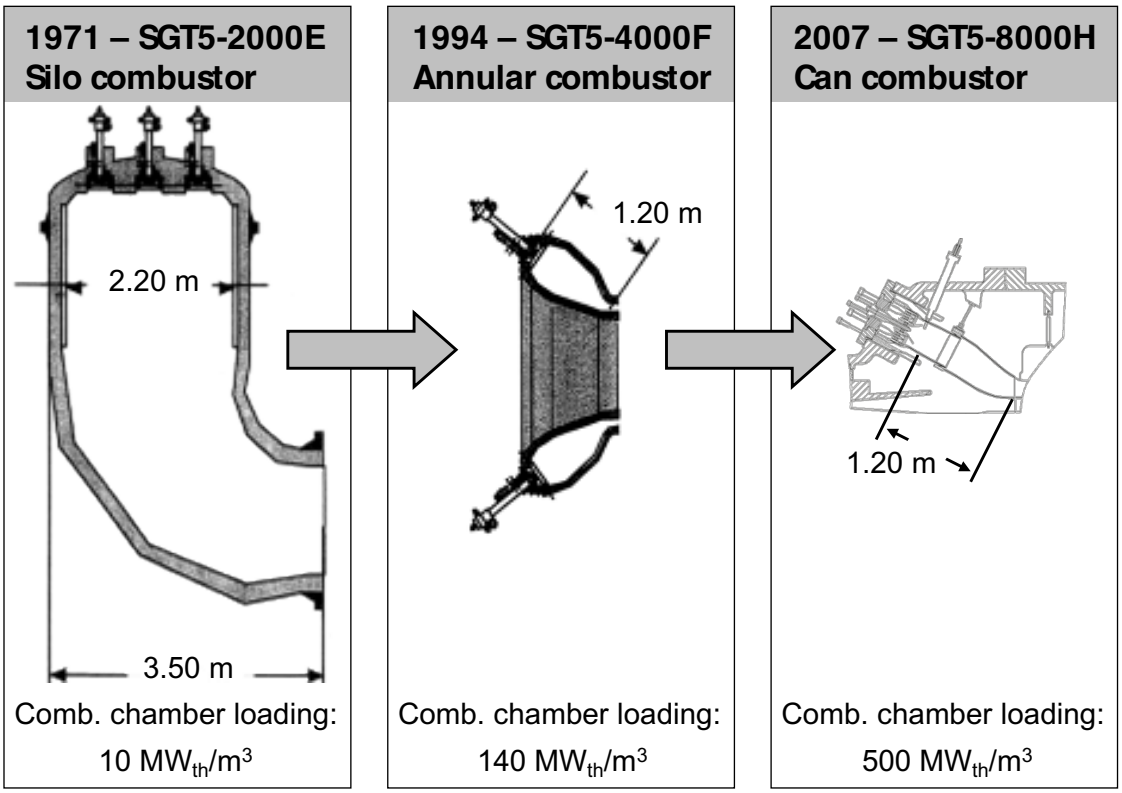

Figure 1.3: Combustor development from large silo to compact annular and can type designs with indicated magnitude of thermal load in MW_{th}/m^3 [2].

Due to the highly turbulent and lean premixed conditions, these systems are prone to combustion instabilities known as thermoacoustics or combustion-induced oscillations and exhibit reduced damping capabilities in consequence of their compactness [3, 4], which affects the operation of the engine in terms of flame blow-off, increased wear, structural damage or engine trips [3]. Hence, the stability of the combustion process of a particular combustor design has to be considered during the development process of combustors [3, 5–9] and during operations of the engine [10, 11].

Additional requirements for the combustion system result from the decarbonization process, in which fuels such as syngas, hydrogen and ammonia are envisaged as substitute fuels. These differ from natural gas in particular in terms of density, lower heating value, adiabatic flame temperature and laminar flame speed [12]. Recently, in order to solve the problems imposed on the combustion system, systems have been developed which have an axially staged fuel injection, also known as fuel staging, and thus feature an additional combustion zone downstream. In combination with specifically designed main burner stages, such designs can mitigate the risk of flashbacks, reduce combustion chamber oscillations by axially staged heat release, and

lower NO_x emissions by shortening residence time in high-temperature regions. Two such systems, the GE AFS (axial fuel staging) and the Siemens DCS (distributed combustion system) are shown in Figure 1.4 below.

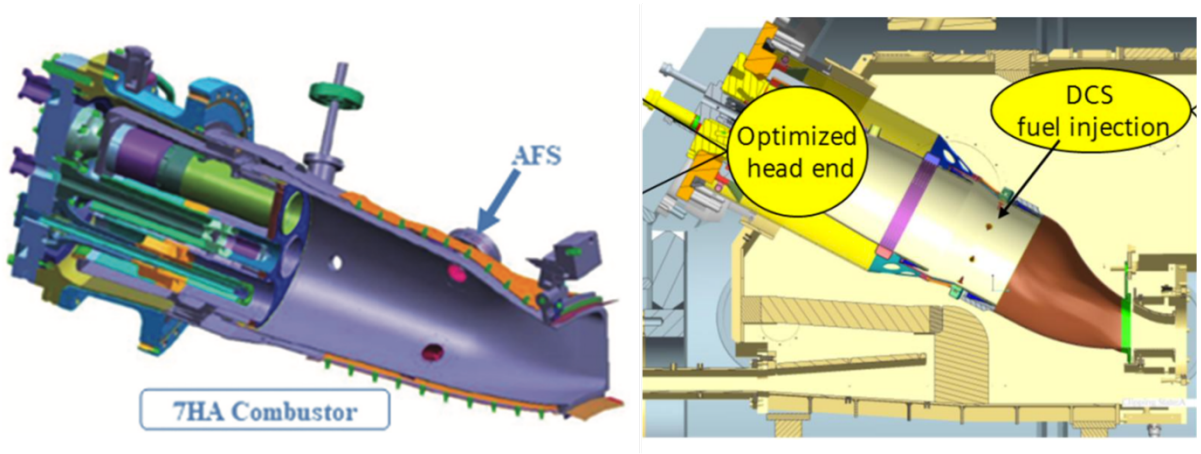

Figure 1.4: GE AFS concept for the 7HA combustor with fuel/air injection in the transition piece (left) [13] and Siemens DCS concept with an additional fuel stage in the basket (right) [14].

The additional air/fuel (AFS concept) or fuel (DCS concept) injection stages are also referred to as cross-stage.

1.2 High-Pressure Combustion Rig Testing as Development Tool

In consequence of the above presented requirements, newly developed or slightly altered combustor designs are subject to a multi-step validation procedure (Figure 1.5), including intense combustion testing of the design under atmospheric, i.e., low-pressure, and high-pressure conditions (steps 2 and 3). While the atmospheric combustion tests of a full-scale, single burner already provide initial conclusions about the performance of the burner design in terms of, e.g., ignition behavior, emissions and thermoacoustics, the full-scale single burner high-pressure combustion tests play a key role in the validation process. These tests allow for investigations of the single combustor under elevated pressure levels up to full engine pressure.

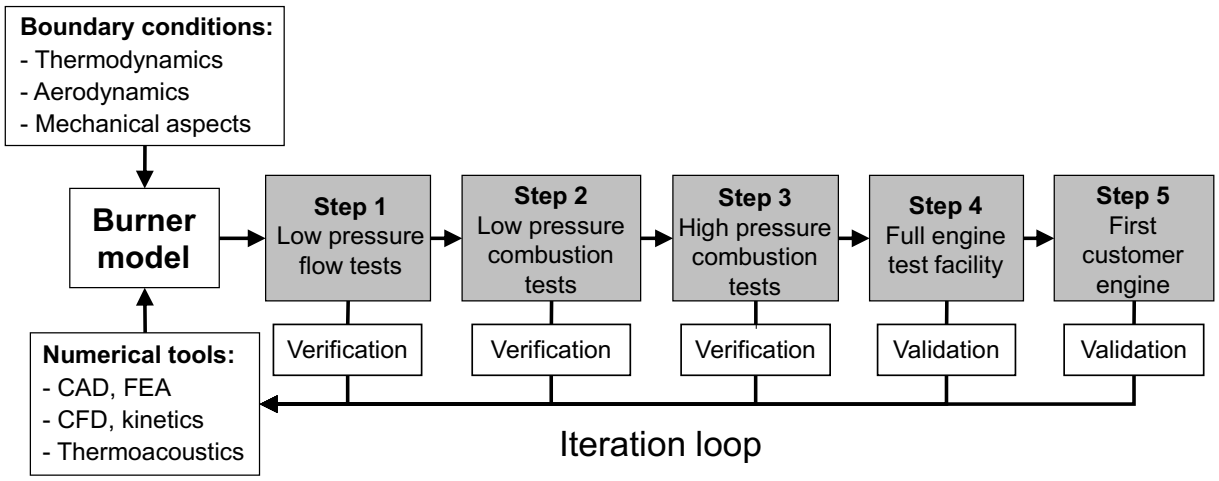

Figure 1.5: Siemens industrial gas turbine combustion system validation procedure [2].

These tests are conducted at specifically designated test centers, like the DLR in Cologne or the Clean Energy Center in Ludwigsfelde. These test sites feature the appropriate facilities, such as compressors, air preheaters, gas supply equipment, etc., to provide the required boundary conditions. The burner under investigation is placed in a pressure vessel, which is regularly equipped with an exchangeable so-called flow box, which simulates the flow conditions prevailing for the burner in the real machine by mimicking engine features like the compressor exit diffuser, the first turbine guide vane, and the engine mid frame. For data acquisition, the test rigs are equipped with traditional sensors like thermocouples, pressure transducers, flow meters and the like. A disadvantage of tests at these sites are the associated high costs, so that a maximum of information content should be obtained from each test. In contrast to atmospheric rigs or scaled high-pressure rigs, the full-scale high-pressure test rigs or more precisely the pressure vessels employed have no or only limited optical access, making the use of optical measurement techniques, which is, however, almost indispensable for the detailed investigation of complex flow or combustion processes, difficult. Access through optical windows, as it is possible for example with atmospheric test rigs, is not feasible at the high prevailing pressures and temperatures in combination with the required dimensions of the test rigs. Thus, optical access is usually achieved via cooled rigid endoscopic probes, which, for example, transmit the measurement signal via optical fibers or lenses/mirror systems [2, 15–17]. Although the rigid endoscopic probes employed to date allow optical access to the test rig, they have the disadvantage that they can only be fed through the pressure barrier, i.e., the pressure vessel, at certain locations and hence can only reach certain positions within the test rig. Thus, their application is usually limited to a combination of burner and flow box determined prior to the design of the feedthrough or probe. Consequently, they cannot be used after a change to a different burner

hardware, where a different flow box must also be used, or only after costly modification of the probe or the feedthrough. Rigid probes can also not be used, or only with great effort, with burner hardware whose components experience different thermal expansion during the experiments compared to the pressure vessel. In addition to the limited optical access, the use of optical measurement techniques is further complicated by the harsh conditions in or next to the test rig, due to high acoustic pressure or vibrations (easily reaching 150 dB [17]), which may damage the sensitive measurement or electronic equipment, such as the recording system (e.g., CCD/CMOS cameras and image intensifier), lasers or computers.

1.3 Research Objective

Following the high costs of high-pressure tests and the complexity of various combustion phenomena, respectively, and the desire to obtain as much information as possible per test and to apply optical measurement techniques in order to investigate the combustion process inside the combustion chamber in more detail, the main goal of the present work was the development of an optical access to the high-pressure test rigs, which would meet the various requirements for the application on these very test rigs and, at the same time, would enable the use of certain optical measurement methods in a way that would allow the regular and comparatively simple application of the measurement methods. To achieve this goal, a probe was to be developed, which protects the sensitive optics from the harsh conditions inside the combustion chamber, limits the impact of the probe on the test rig by a compact design and features a high mechanical flexibility to enable its application at different test rigs and mounting positions. Moreover, the newly developed probe shall offer a modular design to allow the use of different optical measurement techniques. In addition, evaluation routines were developed to determine the location of the heat release zone in the combustion chamber and to investigate the thermoacoustic behavior of the burner in order to evaluate the potential contribution of imaging chemiluminescence measurements during high-pressure measurements in the development of new burner designs and concepts.

1.4 Thesis Outline

The theoretical principles of technical combustion in gas turbines and of flame-induced oscillations (thermoacoustics) are presented in chapter 2 of this thesis, as are the optical measurement methods used in the context of flame diagnostics.

The development of the fiber-based endoscopic probe and the optical access ports of the test rigs is presented in chapter 3 and 4. The development is divided into the design of the input and output optics (chapter 3), the design of the modular probe head for the NDP-1, the HBK-4 and the CEC test rig and the design of the associated probe heat sinks and water supply, as well as the modifications that were necessary on the test rigs in order to use the developed probe. The thermodynamic performance of the developed probe and the results of subsequent inspection after its operation on two consecutive days at the CEC test rig at rig pressures of up to 1.6 MPa and air temperatures of 750 K is briefly presented afterwards (chapter 4).

Chapter 5 deals with the fiber-based measurements conducted at the full-scale test rigs. The measurements are divided into imaging chemiluminescence measurements for the determination of flame length, flame position and for the investigation of flame oscillations for burners of the Siemens SGT5-4000F and SGT5-8000H engines under atmospheric conditions at the NDP-1 test rig and under high-pressure conditions with pressures up to 1.6 MPa at the HBK-4 (flame oscillation only) and CEC test rig, respectively. After a description of the experimental setups and the developed post-processing routines, the results are presented and discussed. Chapter 5 also includes a brief summary of the experimental setup and the results of fiber-based wall temperature measurements using thermographic phosphors at the CEC test rig, for which use was made of the probe access implemented in this work and of a modification of the developed probe.

The thesis concludes with a summary and an outlook for future work in chapter 6.

2 Theoretical Background

2.1 Introduction

This chapter presents a brief introduction to the theoretical background of the thesis. First, the fundamentals of technical combustion and the mechanisms underlying flame-induced oscillations are discussed. Subsequently, an overview of the optical measurement techniques regularly used in scaled combustion experiments is presented. Finally, a more detailed description of flame chemiluminescence follows, as it was selected as a robust measurement technique for use in this work.

2.2 Combustion Fundamentals

Combustion is the conversion of the reactants A and B, i.e., fuel and oxidizer, into the products C and D via an exothermic reaction. As a simplified one-step reaction, it is described by

$$\nu'_{\mathrm{A}}\mathrm{A} + \nu'_{\mathrm{B}}\mathrm{B} \overset{k_{\mathrm{f}}}{\rightarrow} \nu''_{\mathrm{C}}\mathrm{C} + \nu''_{\mathrm{D}}\mathrm{D} \qquad 2.1$$

with ν' as the stoichiometric coefficient of reactants and ν'' as of the products. The reaction rate coefficient for the above stated forward reaction is referred to as k_{f}.

In general, a distinction is made between two types of combustion, which differ in terms of the supply of fuel and oxidizer to the combustion process. The first type is characterized by the

separate supply of fuel and oxidizer to the combustion process and referred to as non-premixed combustion. The second type, where fuel and oxidizer are mixed prior to and supplied as mixture to the process, is termed premixed combustion. However, in technical combustion systems, particularly in gas turbines, the hybrid form known as partially premixed combustion often occurs, in which both types are present at the same time.

In non-premixed combustion, the mixing of fuel and oxidizer is driven by the diffusion of the reactants into the reaction zone, where the combustion, i.e., the conversion into the products, takes place. As the diffusion time scale τ_d is larger than the chemical time scale τ_c, such combustion is also referred to as mixing controlled. The temperature in the burned state T_b is affected by the temperature of the unburned reactants T_u and the heating value of the selected fuel.

The mixing of fuel and oxidizer is described by the mixture fraction. For a system comprising only an inlet stream of fuel $\dot{m}_\mathrm{f}$ and oxidizer $\dot{m}_\mathrm{ox}$, the mixture fraction is given by [18]

$$Z = \frac{\dot{m}_\mathrm{f}}{\dot{m}_\mathrm{f}+\dot{m}_\mathrm{ox}} \tag{2.2}$$

According to this definition, the mixture fraction for the fuel stream is $Z = 1$ and for the oxidizer stream hence $Z = 0$. The mixture fraction where fuel and oxidizer are consumed completely during the combustion process is called the stoichiometric mixture fraction and is defined by [18][1]

$$Z_{st} = \frac{Y_{\mathrm{O}_2,2}}{\nu Y_{\mathrm{f},1} + Y_{\mathrm{O}_2,2}} \tag{2.3}$$

with ν as the stoichiometric mass ratio, $Y_{\mathrm{f},1}$ as the mass fraction of fuel in the fuel stream and $Y_{\mathrm{O}_2,2}$ as the mass fraction of oxygen in the oxidizer stream. The location of the layer of the stoichiometric mixture fraction might define flame dimensions such as flame height of idealized laminar diffusion flames as presented in [18].

[1] The complete mathematical deduction results from the so-called coupling function and is shown in [18].

The advantage of non-premixed flames is their high stability as well as their easy controllability. The disadvantage is the high flame temperature caused by the stoichiometric mixture in the flame front and the resulting high emissions, as well as the low efficiency compared to premixed flames. Nowadays, non-premixed flames are mainly used for the combustion of low calorific or liquid fuels as well as for the start-up of gas turbines or at low loads [3].

However, premixed flames are predominantly used in natural gas-fired stationary gas turbines for power generation, as they feature a more favorable emission behavior. The stoichiometry of the premixed mixture of fuel and air can be described by means of the equivalence ratio in terms of mixture fraction [19]

$$\phi = A\frac{Z}{1-Z} \tag{2.4}$$

with A as the stoichiometric air-fuel-ratio or in terms of mass fraction [20].

$$\phi = \frac{(Y_\mathrm{f}/Y_\mathrm{ox})_\mathrm{u}}{(Y_\mathrm{f}/Y_\mathrm{ox})_\mathrm{u,st}} \tag{2.5}$$

In equation 2.5, subscripts refer to the unburned state (u) and the unburned stoichiometric state (u, st). Although the description of the structure of premixed flames is complex, three different regimes are separable as suggested by Zeldovich and Frank-Kamenetzkii [18, 21], namely a preheat, an inner reaction and a recombination zone. A schematic illustration of a one-dimensional, lean laminar premixed flame with high activation energy and assumed one-step global reaction and without heat loss is presented in Figure 2.1 and displays the distribution of Temperature T, the mass fraction of O_2 (Y_{O_2}), fuel (Y_B) and the products (Y_P) as well as the chemical reaction rate $\dot{m}_\mathrm{i}$. The preheat zone expands up to until the inflection point of the temperature profile T_i, where the reaction zone begins, followed by the recombination zone, after the temperature has reached its final value for the burned state T_b.

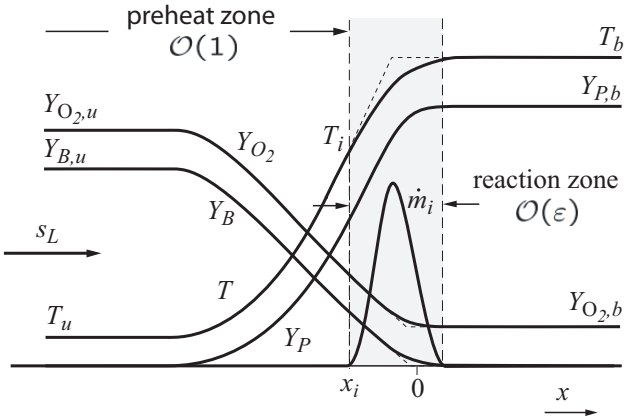

Figure 2.1: Schematic illustration of a one-dimensional, lean premixed flame with one-step global reaction and without heat loss [18].

During the combustion, the temperature increases from the unburned temperature T_u to the adiabatic flame temperature of the given mixture T_b. The arriving mixture is preheated by thermal fluxes from the reaction zone. Reaction products diffuse into the upstream flow as well as fuel and oxidizer into the reaction zone, while the chemistry is slow. The main chemical reaction, i.e., the fuel decomposition, occurs in the inner layer. Combustion radicals such as OH and CH are formed and the emergence of CO and NO_x, as well as the conversion of combustion intermediates into products like H_2O and CO_2, begins. The reaction rate $\dot{m}_\mathrm{i}$ reaches zero in the transit to the recombination layer after all fuel has been consumed. In the recombination zone, NO_x is further produced slowly, and the composition reaches its equilibrium state.

The extension of the flame front in the normal direction is often approximated by means of the thermal flame thickness, which according to equation 2.6 results in [20]

$$l_\mathrm{F} = \frac{T_\mathrm{b} - T_\mathrm{u}}{\max\left(\left|\frac{dT}{dn}\right|\right)} \qquad 2.6$$

and is thus given by the temperature gradient between the burned and unburned state. The flame front propagates normal to itself. In general, the thermal flame thickness of premixed flames is smaller than the thermal flame thickness of a diffusion flame as can be seen from the profiles in Figure 2.2.

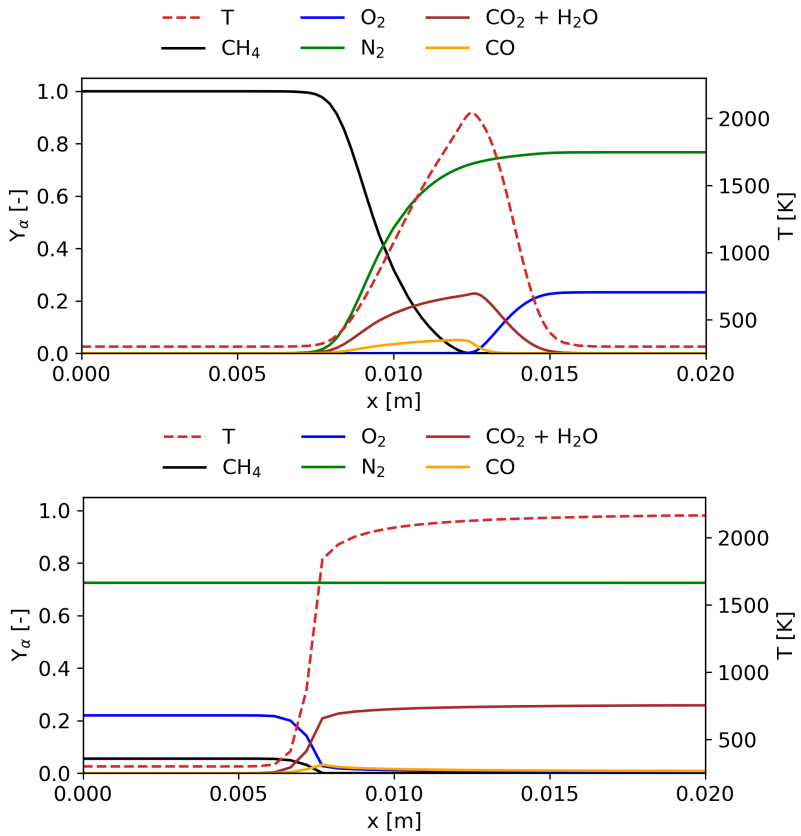

Figure 2.2: Spatial profiles of temperature, methane, oxygen, nitrogen, carbon monoxide, carbon dioxide and water mass fractions for a 1D laminar non-premixed (left) and premixed (right) flame at ambient conditions [19].

The speed of propagation is often referred to as the burning velocity. In case of a laminar premixed flame, the conservation of mass leads to [18]

$$(\rho v_\mathrm{n})_\mathrm{u} = (\rho v_\mathrm{n})_\mathrm{b} \tag{2.7}$$

with v_n as the normal velocity and ρ as the density for the unburned (u) and burned (b) mixture. In case of a steady flame front, the laminar burning velocity must be equal to the normal velocity of the unburned mixture [18]

$$s_\mathrm{L} = \mathrm{v}_\mathrm{n,u}. \tag{2.8}$$

The laminar burning velocity depends on reactant fuel species, equivalence ratio, temperature of the unburned mixture, heat loss, pressure, and aerodynamic strain. Under the assumption of a one-step reaction with one chemical time scale τ_c[2], the laminar burning velocity is given by [18]

$$s_L = \left(\frac{D}{\tau_c}\right)^{1/2}. \tag{2.9}$$

In equation 2.9, D is the thermal diffusivity defined as [18]

$$D = \frac{\lambda}{\rho_u c_p} \tag{2.10}$$

with the thermal conductivity λ and the specific heat capacity c_p of the burned and the density ρ_u of the unburned state. In the case of turbulent premixed flames, as predominantly present in modern gas turbines, the properties of the laminar premixed flames, in particular the laminar flame velocity and the flame thickness, are coupled with the properties of turbulent flows such as velocity fluctuations and characteristic length scale. In consequence, the assumption of a laminar smooth and continuous flame may fail and the magnitude of impact on the flame front thus depends on the overall turbulence field. To categorize this impact, Borghi [23] and Peters [24] have proposed a regime diagram relating the velocity and length scale ratios, which is shown in Figure 2.3.

[2] The chemical time scale also considers the structure of the flame. Its detailed definition is given in [22].

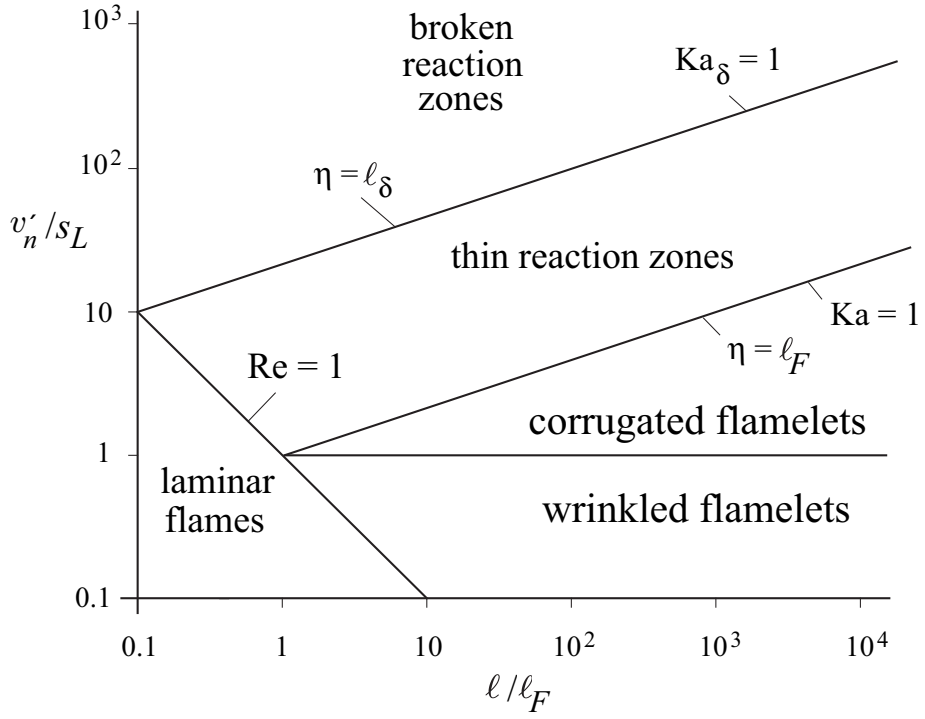

Figure 2.3: Regime diagram of premixed combustion [18].

In the diagram, the interaction between the turbulence and the flame is described by dimensionless numbers, which are derived in the following. Locally, the turbulence field can be characterized by the velocity fluctuation defined as [22]

$$v' = \left(\frac{2\bar{k}}{3}\right)^{1/2} \tag{2.11}$$

The turbulent kinetic energy $\bar{k}$ in the equation above is defined as [22]

$$\bar{k} = \frac{1}{2}\overline{v'^2_\beta}, \qquad \beta = 1,2,3. \tag{2.12}$$

In this context, the decay rate of the turbulent kinetic energy is the eddy dissipation rate with l_T as the turbulent length scale [22]

$$\bar{\varepsilon} = c_1 \frac{\bar{k}^{3/2}}{l_\mathrm{T}} \tag{2.13}$$

Considering l as the integral and η as the Kolmogorov length scale, additional definitions for the turbulent Reynolds number [22]

$$Re_\mathrm{T} = \frac{\nu' l}{s_\mathrm{L} l_\mathrm{F}} \tag{2.14}$$

the turbulent Damköhler number, which correlates the integral time τ to the flame time τ_F [22]

$$Da_\mathrm{T} = \frac{\tau}{\tau_\mathrm{F}} = \frac{s_\mathrm{L} l}{\nu' l_\mathrm{F}} \tag{2.15}$$

and two turbulent Karlovitz numbers, one for the integral length scale as the ratio of the flame time to the Kolmogorov time τ_η and thus the ratio of flame thickness to the Kolmogorov length [22]

$$Ka = \frac{\tau_\mathrm{F}}{\tau_\eta} = \frac{l_\mathrm{F}^2}{\eta^2} \tag{2.16}$$

and the second one for the ratio of the inner thickness l_δ to the Kolmogorov length [22]

$$Ka_\delta = \frac{l_\delta^2}{\eta^2} \tag{2.17}$$

might be used to classify the different regimes. The regimes indicated in Figure 2.3 can be characterized based on Re_T, Da_T, Ka, Ka_δ, the ratio of velocity fluctuation v', and the laminar burning velocity s_L. The different regimes are [22]

- Laminar flames ($Re_T < 1$): This regime represents the laminar flames.
- Wrinkled flamelets ($Re_T>1$, $Da_T>1$, $Ka<1$, $Ka_\delta<1$, $v'/s_L<1$): The flames are slightly wrinkled by low-intensity turbulent fluctuations, yet the flame thickness is thinner than the turbulent length scales.
- Corrugated flamelets ($Re_T>1$, $Da_T>1$, $Ka<1$, $Ka_\delta<1$, $v'/s_L>1$): The laminar flame speed is lower than the turbulent fluctuations and the flame front is significantly wrinkled. Small, isolated flames within the length scale of turbulent eddies may occur.
- Thin reaction zones ($Re_T>1$, $Da_T>1$, $Ka>1$, $Ka_\delta<1$, $v'/s_L>1$): The eddy size is within the range of the preheating zone and the diffusivity exchange with the reaction zone as well as the curvature of the thin reaction zone increases.
- Broken reaction zone ($Re_T>1$, $Da_T>1$, $Ka>1$, $Ka_\delta<1$, $v'/s_L>1$): The turbulence length scale is within the scale of the thin reaction zone and the chemical reaction collapses due to convective removal of combustion radicals from the inner flame layer.

Already for the corrugated flames, the flame front is partially moved by turbulent fluctuation and propagates with the turbulent rather than the laminar burning velocity s_T into the unburned mixture. Under the assumption that the turbulent flame is an ensemble of laminar flames, the conservation of mass ($\dot{m} = \text{const.}$) leads to [22]

$$s_T A \bar{\rho}_u = s_L A_T \rho_u \qquad 2.18$$

with A and A_T as the flame surface in the laminar and the turbulent case, respectively and $\bar{\rho}_u$ as the average density of the unburned mixture. The increase of the burning velocity with turbulence allows for more compact designs of the combustion chamber.

2.3 Flame-Induced Oscillations

The trend towards increasingly compact combustion systems and lean premix flames with intense mixing has resulted in combustion systems prone to combustion-induced oscillations, also referred to as thermoacoustics, due to the resulting coupling of heat and sound, i.e., pressure fluctuations. They represent an inherent property of the combustion process, yet are uncritical, if they occur irregularly. However, the resulting fluctuations, which propagate in a wave-like manner, can be reflected by the walls in enclosed systems, such as the combustion chamber of GT. As a result, they may cause flow or mixing fluctuations, which themselves result in a fluctuation of the heat release, triggering new pressure fluctuations and thus closing the feedback loop, as shown in Figure 2.4. For a system to become unstable due to these fluctuations, i.e., for an energy influx to the acoustic field to occur, the criterion named after Lord Rayleigh [25] must be fulfilled that the fluctuation of the heat release rate is in phase with the pressure fluctuations. The result can be severe damage to the mechanical structure of the combustor or gas turbine if the energy added during the closed feedback loop is greater than the energy loss due to dissipation or through system boundaries. The criterion may be written for the case of premixed gas turbine combustion systems as [6]

$$R(t) = \frac{\int_t^{t+T_{\mathrm{per}}} \int_{V_{\mathrm{HR}}} p'(\vec{r},t) q'(\vec{r},t)\, d\vec{r}\, dt}{\bar{p}\bar{q} V_{\mathrm{HR}} T_{\mathrm{per}}} \qquad 2.19$$

with p' as the pressure and q' as the heat release fluctuations, $\bar{p}$ and $\bar{q}$ as the mean values of pressure and heat release, respectively, V_{HR} as region of the heat release and T_{per} as the oscillation period.

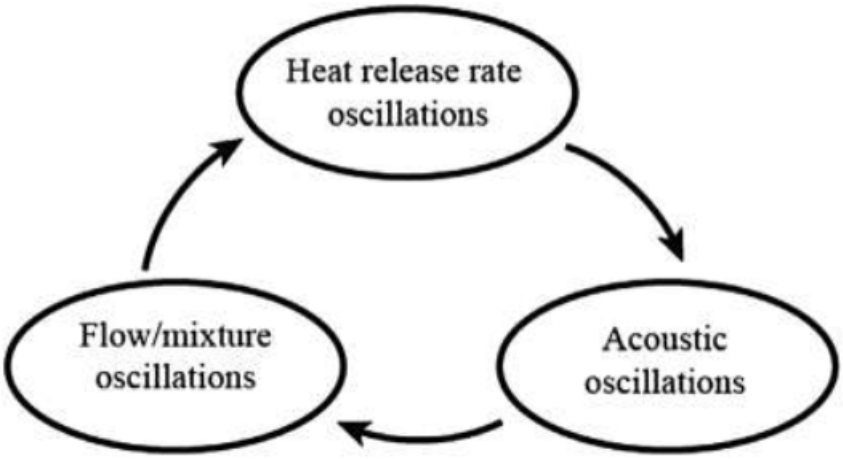

Figure 2.4 Thermoacoustic feedback loop [26].

Several driving mechanisms for the oscillation may be identified in GT combustors and several different mechanisms may occur and be superimposed within such systems. In literature, mainly six different mechanism were identified, as summarized by Sharifi [27]. The different mechanisms are:

Flame/Vortex Coupling Mechanism

The flame area is periodically extended due to vortex structure shedding, resulting in a fluctuation in heat release.

Equivalence Ratio Coupling Mechanism (Fuel Time-Lag Mechanism)

The pressure fluctuations reach the upstream fuel and air supply and affect the mixture distribution. In consequence, perturbations occur within the premixed mixture and are consumed in different locations in the flame, hence, at different moments, leading to significant fluctuations of the local heat release rate.

Pressure/Density Coupling Mechanism

The heat release rate is proportional to the density of the reactants in the unburned mixture. In consequence, pressure fluctuations propagate upstream into the unburned mixture, leading to reactants density fluctuation, thus to heat release rate oscillations.

Pressure/Chemistry Coupling Mechanism

The acoustic field affects the local flame speed and the enthalpy of the reaction, varying the local heat release rate.

Flame Stretch Coupling Mechanism

The fluctuation in heat release rate is caused by the altering flame stretch due to velocity gradients as a result of pressure fluctuations, which impacts the local flame speed.

Flame Displacement Mechanism

In tubular single burner combustor setups, the so-called flame displacement was observed, where the flame itself was periodically displaced due to pressure oscillations.

Despite the variety of possible driving mechanisms, many studies have identified local and temporal fuel/air distribution fluctuations, i.e., the equivalence ratio coupling, as the most dominant influencing parameter in lean premixed combustion systems [28–31].

2.4 Optical Measurements Techniques

During high-pressure rig testing, the test rig as well as the combustor hardware under investigation are equipped with numerous sensors such as thermocouples, pressure transducer, flow meters etc., which provide an information density allowing for initial statements regarding performance, emissions as well as stability. However, they usually cannot provide detailed information about transient processes such as flame behavior during combustion-induced oscillations or temporal and spatial invariants like hot pockets or local flame quenching. For the investigation of such phenomena, optical measurement techniques are well suited, which are nowadays used in a multitude of applications, albeit partly only on a laboratory scale. These measurement techniques include laser-based techniques such as laser-induced fluorescence (LIF) for the detection of atoms or molecules in liquid and gaseous flows [32–34], filtered Rayleigh scattering (FRS) for the simultaneous detection of pressure, temperature and velocity [35, 36], particle image velocimetry (PIV) and techniques based on the Doppler effect (phase Doppler velocimetry (PDV) [37], laser Doppler velocimetry (LDV) [38], Doppler global velocimetry (DGV) [39, 40]) for velocity measurements, laser-induced incandescence (LII) for the determination of the soot volume fraction [41, 42], tunable diode laser absorption spectroscopy

(TDLAS) for species concentration measurements [43], coherent anti-Stokes Raman spectroscopy (CARS) for temperature detection of the gas phase [44] as well as phosphor thermometry for wall temperature measurements [45, 46]. Examples of techniques utilizing a flame-inherent emission include pyrometry [47] as well as chemiluminescence [48, 49], the latter of which is widely used in the study of flames due to its simplicity and robustness and will be described in more detail in the following section.

An overview of the suitability of the various measurement techniques for application in high-pressure test rigs is given in [17].

2.4.1 Chemiluminescence

Chemiluminescence is the emission of light[3] due to a chemical reaction, which also takes place in flames. The effect is based on the formation of an excited intermediate during the combustion process and its radiative decay to the final products as given by

$$\mathrm{A} + \mathrm{B} \rightarrow \mathrm{AB}^{*} \rightarrow \mathrm{P} + h\nu \tag{2.20}$$

with the reactants A and B, the intermediate state AB^{*}[4], the final products P and the dissipated energy, described by h as the Planck constant multiplied by the photon frequency ν. By using the coherence of the frequency and the wavelength of light

$$h\nu = \frac{hc}{\lambda} \tag{2.21}$$

with c as the speed of light and λ as the specific wavelength and considering the fact that only specific transitions are spin allowed for each species, chemiluminescence can be used in combustion diagnostics, enabling wavelength-selective detection and signal discrimination against background radiation from hot walls or soot. In methane or natural gas-air combustion, the predominant chemiluminescence species used for diagnostics, as can be seen from the representative emission spectrum in Figure 2.5, are OH^{*} (characteristic emission at 285 nm and

[3] Throughout this thesis, the term light encompasses the wavelength region from 180 to 1000 nm of the electromagnetic spectrum.
[4] The asterisk denotes the excited state.

310 nm), CH^* (main peak at 430 nm and secondary peak at 388 nm), C_2^*, with its three characteristic peaks between 430–520 nm, as well as the broad-band emission of CO_2^*(mostly assumed in the range of 270 to 550 nm), although in particular for the latter, further chemiluminescent species such as HCO^* and CH_2O^* need to be considered [50].

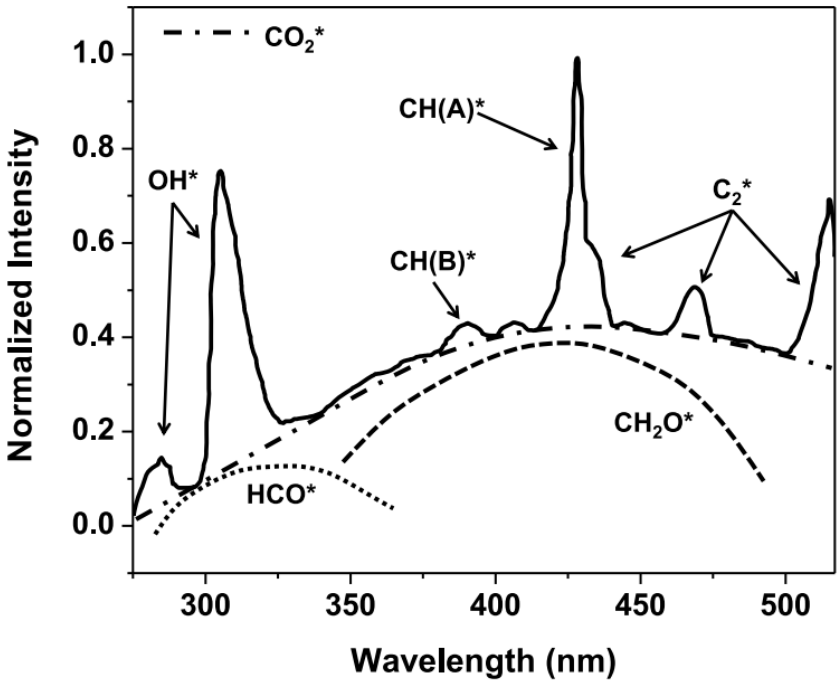

Figure 2.5: Typical mission chemiluminescence spectrum of a natural gas-air flame with indicated broadband emission of CO_2^*, HCO^* and CH_2O^* [50].

Figure 2.6 presents the reaction pathway diagram for a premixed methane-air flame. The main carbon path is indicated by the green arrows. Although the production of the species OH^*, CH^* and CO_2^* (encircled in red) only occurs in the side paths of the reaction process, as indicated by the dashed arrows, and with low production rates [51], the signal is in general strong enough for detection and discrimination of the desired species. Nonetheless, the shape of the spectrum shown in the figure depends on the local and global combustion properties and boundary conditions such as pressure [52, 53], temperature [54, 55], equivalence ratio [56–58], strain rate [59], etc. In particular, some studies have found a significant increase in broadband emissions (especially of CO_2^*) at the pressure levels prevailing in GT combustors, as well as significant reabsorption of OH^* emissions by ground-state OH [54, 60], which occurs particularly in the exhaust path or oxidation zone. However, this appears to be at least partially conditioned by the flame geometry, the exhaust gas composition and the angle of observation, as the problem was not observed in other studies at elevated pressure [15, 16, 55]. The reaction mechanisms of the

predominant species have been studied in detail both experimentally and numerically in a variety of studies, e.g. in shock tubes [61, 62].

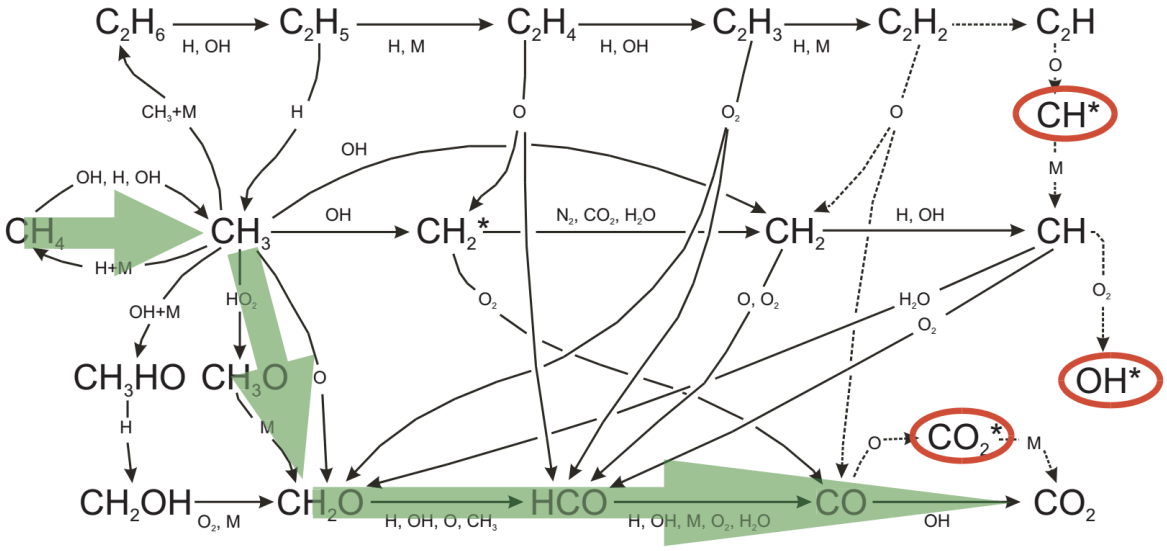

Figure 2.6: Reaction pathways for CH_4-air combustion and the occurrence of OH^*, CH^* and CO_2^*. The main reaction pathway is indicated by green arrows [63].

Compared to other optical measurement methods, especially the simplicity and robustness of this measurement technique predestines the use of imaging chemiluminescence measurements on scaled and unscaled combustion test rigs to provide information on the flame position and shape. Short exposure or high-speed imaging measurements also allow the investigation of transient processes such as the ignition behavior [64–66], the flame propagation [67] or flame-induced oscillations [68–70]. In the latter case, the so-called phase-averaging approach [54, 71, 72] or the optical transfer function [72–74] can contribute significantly to the understanding of such phenomena in specific burners.

Although the qualitative evaluation of imaging chemiluminescence measurements usually causes little problems, quantitative assessments are rendered difficult by the integration of the signal along the line of sight. Reconstruction mechanisms such as the Abel deconvolution [75–77] are limited to strictly rotationally symmetric systems – a constraint rarely satisfied by technical premixed flames. A more promising approach is the use of tomographic reconstruction methods, also referred to as computed tomography of chemiluminescence [78, 79], which have already been successfully used on technical flames and allow a detailed investigation of the three-dimensional flame geometry [80, 81]. However, these reconstruction methods currently

still require a large number of different observation angles for the flame object, which still prevents their use in the case of limited optical accessibility.

2.5 Conclusions

In this chapter, the fundamentals of the combustion process in GT burners were briefly presented, as well as an overview of flame-induced oscillations, since they represent one of the major challenges in lean, premixed and turbulent combustion regimes prevailing in modern GT combustors. This was followed by a brief overview of the most common optical measurement methods, which are regularly used in the investigation of combustion processes in technical flames. Finally, a more detailed introduction to the possibilities of chemiluminescence measurements in the context of the study of technical flames were presented as robust optical measurement the and central optical measurement technique used in this work.

3 Fiber-Based Imaging Sensors

3.1 Introduction

A Fiber-based chemiluminescence detection inside GT combustors holds several unique requirements for the optics development, resulting in a set of design parameters which had to be considered throughout the process. The first design parameter for the optics was the operating wavelength. In general, the focus of this thesis was on two major chemiluminescent species, namely CH^* and OH^*. While the dominant emission of CH^* originates from the $A^2\Delta$ [60] transit with a peak wavelength at 430 nm and therefore lies in the visible range, the strongest OH^* emission at 310 nm stems from the $A^2\Sigma^+$ [60] transit. As a consequence, the desired operation wavelength region ranged from the UV to the visible range, thus narrowing down useable optics material to UV transparent media for the lenses and the fiber bundles. The second and third design parameters were the working distance – which includes the depth of field – and the resulting field of view (FOV) inside the combustors. The fourth parameter originated from the demand to minimize the size of the probe head in order to reduce the disturbance of the experiment, hence, a compact design was required. However, small optics may lead to a high f-number and therefore to slow optics, i.e., low throughput of light. This defined, in combination with the weak signal and high absorbance of UV transmission within the fibers, and the required intensification, the number of lenses as the fifth design parameter.

Another challenge was to image relatively extended objects, i.e., a large area of the combustion chamber, onto a small image area, in this case the input face of the fiber bundle, while maintaining good optical properties, such as low distortion and other aberrations like defocus, coma, astigmatism, chromatic aberration and the like[5], and conversely to project a small image (the

[5] Detailed information on aberrations within optics are presented for example in [82–86]

output face of the fiber bundle) onto a comparatively large detector (camera or image intensifier chip).

The optical system used throughout this thesis can be divided into three parts, namely the fiber bundle, the input, and the output optics. First, the input optics for mapping the object onto the fiber bundle are located in the probe head, the second one is the fiber bundle itself to transport the image with minimal internal loss such as absorption or cross talk, and third and last the output optics, imaging the fiber bundle exit surface onto a detector, e.g., an image intensifier or a camera, located outside of the test rig.

The design of the lens systems shown in this chapter was performed by Dr. Taimoor Talpur at the Institute of Applied Optics, University of Stuttgart.

3.2 Optical Fibers

The usage of optical fibers within this work plays a key role for the desired flexibility of the developed probe, as they enable the signal transport, i.e., the image, from inside the combustor to the detector, without the limitation of a common line-of-sight, as in lens-based systems. Although imaging fiber bundles are common in many applications, the availability of imaging fiber bundles suitable for this work is limited to UV transparent material such as fused silica since, as mentioned above, the emission of OH^* as perhaps the most important species in lean premixed natural gas flames lies in the UV spectrum. Despite the general transmission of UV light in fused silica fibers, fibers doped with OH feature lower attenuation as the more common fibers of low OH content. The attenuation of three different fused silica fibers manufactured by Fujikura in the wavelength range of 200–2000 nm is shown in Figure 3.1.

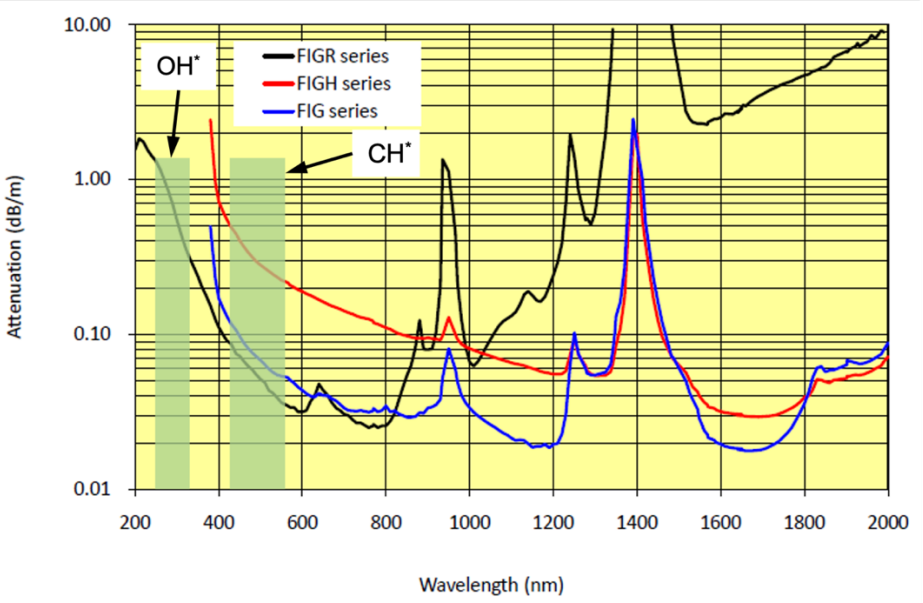

Figure 3.1: Attenuation[6] for different silica fibers manufactured by Fujikura Ltd with the exemplary optical filter windows for detecting the emission of OH^* and CH^* indicated in green [88].

As can be seen from the figure, the *Fujikura FIGR series* represents the most suitable fiber for the detection of OH^* and even CH^*. The high OH doping can be inferred by the overtone at 1400 nm of the characteristic vibrational resonance of OH (2.8 µm) [89]. Two types of fiber bundles were used in this thesis. For each of them, specialized input and output optics were developed. The first bundle was the *Fujikura FIGR 30k* bundle from *Fujikura Ltd.* with 30,000 single fibers with an outer diameter of 6 µm, and with a resulting imaging diameter of 1.8 mm. The second one was a bundle containing 20,000 single fibers from *Nanjing Chunhui Science & Technology Industrial Co, Ltd*, hereinafter referred to as *Nanjing 20k*, with a core diameter of 15 µm, resulting in an imaging diameter of 2.4 mm. An image of the face of each bundle is presented in Figure 3.2.

[6] The attenuation measures the ratio of output and input power and is defined as $dB_{\mathrm{Att}} = -10\log_{10}(P_{\mathrm{out}}/P_{\mathrm{in}})$ [87]

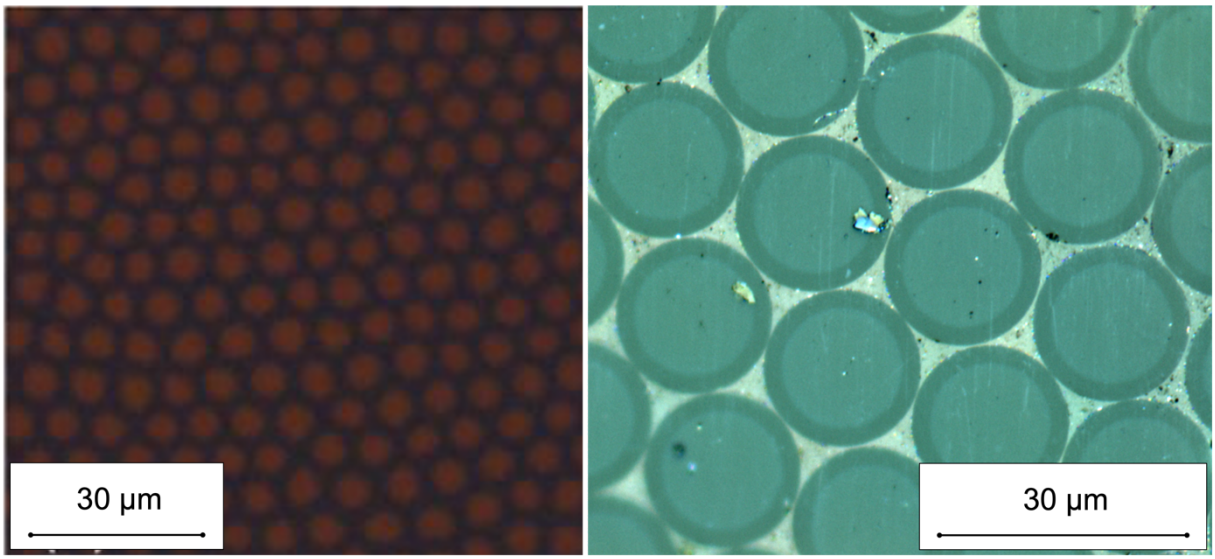

Figure 3.2: Close-up of the faces of *Fujikura FIGR 30k* (left) [90] and *Nanjing 20k* (right). The scale of magnification is indicated in the images.

In addition to those design parameters already mentioned, the two bundles differ from each other in terms of their structure. The *Fujikura FIGR 30k* bundle is formed from fused individual fibers, so that several fibers feature a common cladding, as can be seen in the figure (black space between the fibers). This has the advantage of reduced light loss in comparison to individual arranged fibers, due to the loss of light falling onto the cladding or space between the individual fibers. Due to the fusion, the bundle features a minimum bending radius of 450 mm, strongly limiting its flexibility. The *Nanjing 20k* bundle, on the other hand, consists of individual arranged fibers that are only glued together in the area of the end surfaces, but not fused. Thus, each fiber has its own cladding (darker green rings in Figure 3.2), which suppresses the so-called crosstalk, i.e., light from one fiber passes through the common cladding and enters an adjacent fiber. Furthermore, with this arrangement, the minimum bending radius of the fiber bundle is determined by the minimum bending radius of the individual fiber (100 mm), thus making the bundle significantly more flexible. However, light falling onto the space between the fibers (light green in the figure) is lost and the resolution respectively the fiber density over the image area lower.

3.3 Optics Design

3.3.1 Input Optics

As mentioned above, five design parameters for the input optics were identified. Considering the selected chemiluminescence species, the wavelength range was set to 270–600 nm. For the working distance, the geometrical properties of the test rig geometries available at this stage of the thesis were considered and set to 180 mm. The field of view significantly influences the area of the combustion chamber that can be covered by means of the probe, so that in principle the largest possible field of view was aspired. However, a large field of view sometimes leads to a deterioration of the recorded image. The concept of a modular probe did not require the field of view to be fixed to one value. Rather than that, optics with a field of view of 10°, 25°, and 40° (for the *Fujikura FIGR 30k* bundle only) were developed[7]. To obtain the most compact system possible or the input optics, the maximum allowable lens diameter was set to 10 mm and the maximum axial length, i.e., the length from the front surface of the first optical element to the front face of the fiber bundle, to 50 mm. Finally, the maximum number of lenses was limited to 6.

In spite of specific requirements, the above-mentioned parameters do not define a stop criterion to end the design process. Accordingly, optics of any complexity can be developed with sophisticated lens shapes and high manufacturing costs, hence an additional parameter, suitable to judge the quality, was required. Useful in such context is the often-used spatial image resolution, commonly expressed in lp/mm[8]. In modern optics, high complex aspheric and minuscule lenses allow for spatial resolutions in the range of 200 lp/mm and above and are adapted to high resolution detectors such as CMOS-based cameras, yet their design is laborious and expensive. As an example of such an elaborate system, a first lens design with a FOV of 25° is shown in Figure 3.3. The system features a total of six customized fused silica lenses. The diameter of the front lens is 10 mm and the axial length of the lens system approximately 29.4 mm, thus meeting the criterion of the maximum number of lenses and compactness. The impact of the chromatic aberration was neglected as they a small compared to the spherical aberrations.

[7] Throughout this thesis the term “field of view” refers to half the opening angle in the object space.
[8] The spatial image resolution describes the amount of detail an image can hold, i.e., the ability to separate structures in the object space [91].

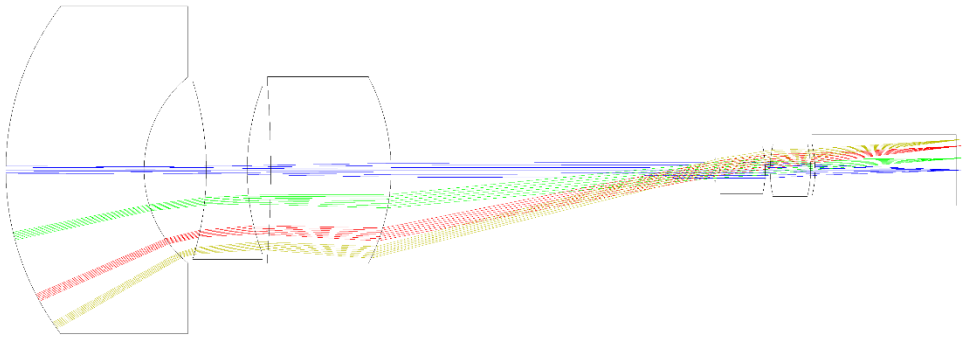

Figure 3.3: Sketch of a customized 25° lens design for the *Fujikura FIGR 30k* bundle [92].

Although the design fulfilled all requirements and seemed to be suitable, the costs associated with the realization of the design are in the range of several thousand Euros, which seems to be unsuitable for a lens design that shall be used inside a combustion test bench and can be easily damaged. This even more holds true if one considers the maximum achievable resolution of the fiber bundles, which feature a cut-off frequency of only 17.8 lp/mm[9] [94] for the better performing *Fujikura FIGR 30k* bundle, as the finite diameter of the included single fibers confine the maximum spatial resolution[10]. As the maximum achievable resolution is defined by the lowest cut-off frequency within the optical path, the fiber bundles limit the overall optical performance. Thus, it is sufficient to couple a sufficiently sharp image into the fiber bundle on the input side and to couple it out on the output side. In consequence, simpler optic designs based on available standard lenses (referred to as off-shelf lenses) may still meet the requirements in terms of achievable spatial resolution. Regardless of the cut-off frequency imposed by the fiber bundle, the remaining issue is the basis on which the required optical performance is determined. This can be seen in Figure 3.4 below, which compares the optical performance of an ideal system (left) with an error-prone system (right).

Figure 3.4: Comparison of optical performance of an ideal (left) and error-prone system (right) [95].

[9] Calculated by $f_{\mathrm{cut}} = \frac{1}{2d_{\mathrm{cc}}}$ [93] with d_{cc} as the center-to-center pitch (28 µm for the *Fujikura FIGR-30k* [94])

[10] Image points smaller than the core diameter of a single fiber mixes inside the fiber and lead to information loss.

As can be seen from the figure, both systems achieve the same cut-off frequency, but feature differences in optical performance in terms of contrast between each line pair. The contrast is the relationship between the maximum and minimum intensity within an image, also referred to as modulation. How well the local contrast of an object is preserved by an optic is often described by means of the so-called modulation transfer function (MTF), which represents the absolute value of the optical transfer function (OTF) derived from the point spread function (PSF) [86]. It ranges from 1 (perfect preservation of contrast) to 0 at the cut-off frequency of the systems, thus, a higher MTF value at a given spatial resolution represents a sharper image with higher contrast. Figure 3.5 shows the diffraction limit[11] (solid black) and the performance, in terms of calculated MTF[12], of a fully customized lens design (dashed lines) of Figure 3.3 and for the selected off-shelf 25° input optics design (solid lines) for the *Fujikura FIGR-30k* bundle (the selected designs are presented in Figure 3.6). In Figure 3.5, the green lines represent the center ray at 0° and the blue ones the MTF the outer ray at 25°, respectively. The calculated cut-off frequency of 17.8 lp/mm of the bundle is indicated by the dashed vertical line.

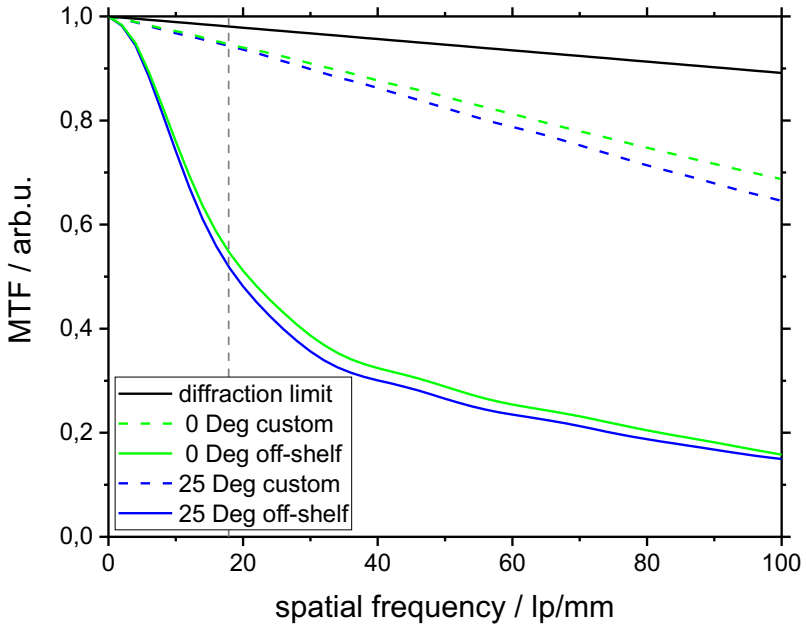

Figure 3.5: Comparison of the optical performance of an off-shelf lens and customized lens design.

[11] The diffraction limit represents the resolution for an ideal optical system due to the limit of diffraction without any aberration [96].
[12] The calculations were performed with *ZEMAX*.

Both systems showed MTF levels above 0.5 at *Fujikura FIGR-30k* cut-off frequency and are therefore suitable for the application. Although the customized optics would perform approximately 1.7 times as well as the off-shelf lenses, the cheaper optics will still produce acceptable images, since an MTF above 0.5 is generally considered sharp [95]. As a consequence, the off-shelf designs were favored and finally selected due to the advantageous price and the sufficient optical performance. For the *Fujikura FIGR-30k* bundle, a total of four different input optics was designed, which are shown in Figure 3.6. In the top row of the figure, the one lens (left) and three lens (right) 10° design are presented. These designs feature a maximum outer diameter of 6 mm and an axial length of approximately 8.3 mm and 14.2 mm, respectively. The design comprises only commercially available fused silica lenses from *Edmund Optics Inc*. (The exact product name of each lens is listed in the Appendix). The other designs presented in the bottom row of the figure are the 25° (left) and the 40° (right) design. These designs require a larger front lens (outer diameter of 10 mm) due to the high acceptance angle. The axial length is 29.5 and 29.4 mm respectively. The fused silica lenses were available at *Edmund Optics Inc*. and *OptoSigma Europe SAS*. The detailed specifications are presented in the Appendix.

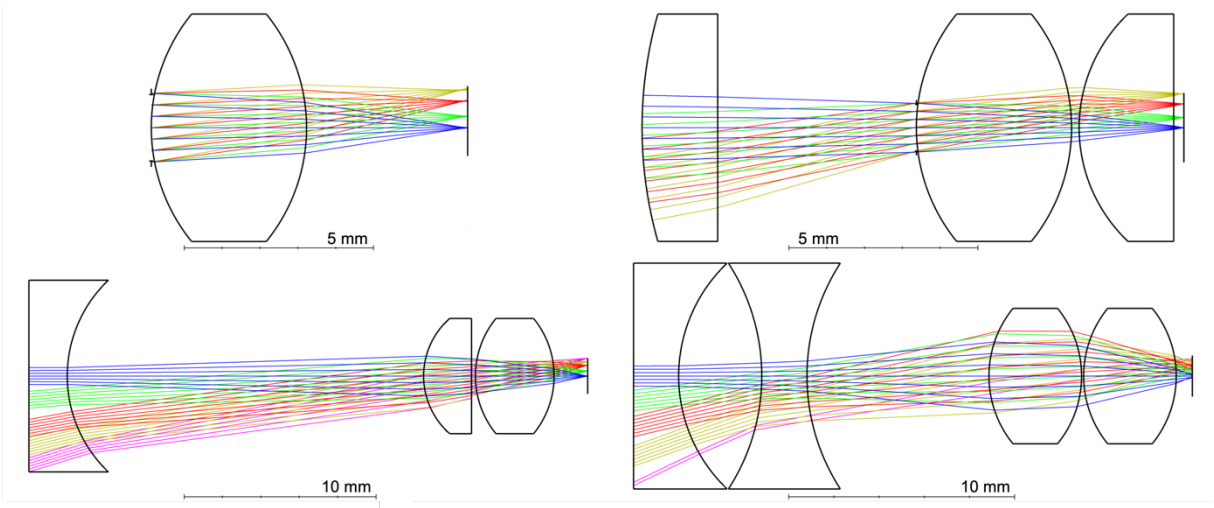

Figure 3.6: Overview of the different input optics for the *Fujikura FIGR-30k* bundle. Top row: 10° single (left) and multiple lens (right) design. Bottom row: 25° (left) and 40° (right) lens design.

For the *Nanjing 20k* bundle, only a 10° and 25° input optics were designed, as presented in Figure 3.7. The 10° design (top) consists of two 5 mm lenses available at *Edmund Optics Inc*. and features a total axial length of approximately 15.5 mm. The 25° design comprises three fused silica lenses (again from *Edmund Optics Inc*.) and is approximately 14.8 mm long (axially) in total. Detailed information is given in the Appendix.

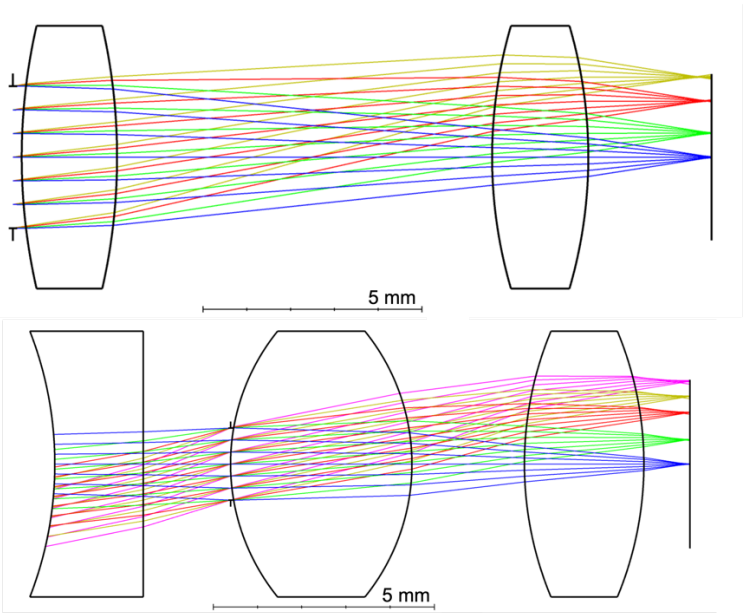

Figure 3.7: 10° (top) and 25° (bottom) input optics for the *Nanjing 20k* bundle.

To ensure the correct distance between the lenses and between the lens system to the fiber bundle, special lens holders were developed, which were inserted into the probe head and fixed there (see section 4.2).

3.3.2 Output Optics

The output optics are located outside the combustion test rig and thus outside of the endoscopic probe. Thus, the conditions imposed on the coupling optics with respect to the compactness of the optics are negligible. The working distance could also be largely arbitrary, since the distance between the optics and the recording system could in principle be selected as desired (however, a small distance is still preferable for reasons of practicality), so that the output coupling optics only had to fulfill the requirements concerning the wavelength range, the smallest possible number of lenses, and the cut-off frequency of the fiber bundle. Since these requirements were met by the various input designs, these were reused for as output design and only the spacing of the individual lenses was adjusted accordingly. Since high-speed image detection of chemiluminescence were of particular interest in the context of this work, the properties of the high-speed image intensifier (IRO) to be used from *LaVision* (cf. chapter 5) were used as the practical basis for adapting the optics. The IRO itself features a circular sensor with a diameter of 25 mm and a similar cut-off frequency of 17.5 lp/mm [97]. The designs are presented in Figure 3.8.

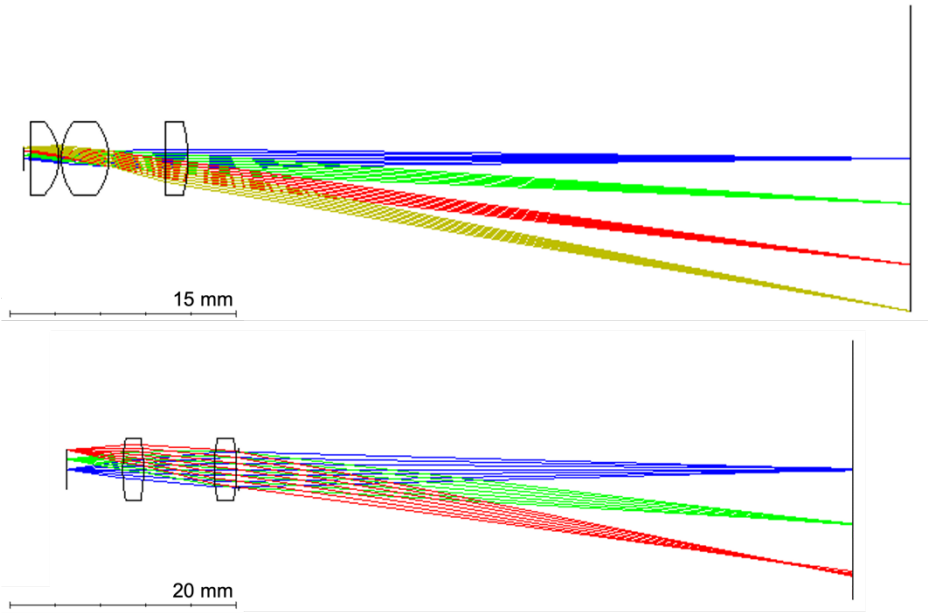

Figure 3.8: Output optics for *Fujikura FIGR-30k* (top) bundle and *Nanjing 20k* (bottom) bundle.

The output design for the *Fujikura FIGR-30k* (top in Figure 3.8) was based on the 25° three lens design with adjusted intermediate distances between each lens and a total length, i.e., the length from the fiber bundle end face to the detector, of approximately 58.5 mm. Similarly, the output design for the *Nanjing 20k* bundle used the respective 25° input design (bottom in Figure 3.8). The total length of the adjusted system is approximately 69.2 mm. Again, the large total length of the output optics was determined by the size ratio of fiber bundle face to sensor area and is acceptable as these optics are located outside the test rig during use.

3.4 Conclusions

In this chapter, the selected imaging fiber bundles as well as the input and output optics designs for each bundle were presented.

As a consequence of the chemiluminescing species selected, in particular OH^* with its characteristic UV emission, the choice of available imaging fiber bundles was limited to bundles made of fused silica single fibers with high levels of OH content to reduce the internal attenuation of the signal. Eventually, two suitable fiber bundles, namely the *Fujikura FIGR-30k* and the *Nanjing 20k*, could be purchased. The former offers a higher resolution due to the smaller inner diameter of the individual fibers, but turned out to be comparatively rigid due to its internal structure with a resulting minimum bending radius of 450 mm. In contrast, the bending radius

of the *Nanjing 20k* bundle is limited only by the bending radius of the individual fibers (minimum radius of 100 mm).

The fiber bundles used were identified to be limiting the quality of the optical resolution. In the best case, i.e., for the *Fujikura FIGR-30k* bundle, they provide a cut-off frequency of 17.8 lp/mm, so that significantly higher performing optics are not necessary. Accordingly, designs were created based on low-cost and readily available standard lenses. Nevertheless, the developed optics met the following requirements:

- Working wavelength range of 200–600 nm
- Working distance of 180 mm for the input optics
- Varying FOV between 10 and 40°
- A maximum compactness of the input optics with a maximum outer lens diameter of 10 mm and a maximum axial length below 30 mm
- A maximum of four optical elements in each design

Although the systems first developed based on a large number of custom-made lenses had an excellent imaging quality, it was shown that the systems developed based on off-shelf lenses still provided a sufficient imaging quality, i.e., an MTF value of above 0.5, at the aforementioned cut-off frequency of the fiber bundles.

Finally, the 25° input designs intended for each of the two fiber bundles were modified and used as output optics to map the fiber bundle end face onto the sensor of the recording system.

4 Flexible, Fiber-Based Probe for Industrial Combustor Test Rigs

4.1 Introduction

The application of optical diagnostics to full-scale GT combustor test rigs inheres numerous challenges, for example, the harsh experimental conditions such as high temperatures, high pressures and high flow velocities inside the test rigs or mechanical constraints like geometrical blockings along the optical path, limited access to the pressurized test rig, or a different thermal expansion of solid rig parts during operations. Additionally, the desire for nearly *in situ* measurements limits the outer diameter of the probe. Considering all challenges, the main requirements for the probe development can be derived:

- Protect sensitive optics from harsh environmental conditions
- Limit impact to the test rig and allowing application to existing test rigs
- Feature high mechanical flexibility to enable different access positions and to account for thermal expansion
- Provide compact design for *in situ* applications

Besides these already challenging demands, another set of requirements must be considered in the design of the probe, partly contradicting but partly derived from the aforementioned:

- Enable different optical configuration
- Provide enough space for light-efficient optics
- Maximize coolant flow section to ensure sufficient cooling

In the following chapter, the different design evolutions of the probe, which were developed during the present work, the test rigs at which measurements were performed and the necessary test rig modifications for the measurements are shown. In particular, the final probe design, generally referred to as the CEC design, fulfilled most of the aforementioned requirements or represented the best possible compromise and was successfully used for both chemiluminescence and wall temperature measurements using thermographic phosphors during high-pressure measurement campaigns (see chapter 5). Its thermodynamic performance during the chemiluminescence measurements is also presented in the following chapter.

4.2 Probe-Head Design

The design of the probe head follows the extensive requirements that had to be met in the development process and represents one of the most complex parts of the probe design. The first and foremost function of the head is to protect the sensitive optics against the harsh environment inside the combustion chamber as the tip of the head – when assembled – is flush with the inner combustor wall or even protruding into the exhaust gas flow, and thus requires adequate cooling. In addition, the probe head must be large enough to accommodate the selected optics (see chapter 3.3). However, the size of the probe head is limited by the fact that the measurements should distort the experiment as little as possible. Consequently, the part of the probe head that is flush with the combustion chamber wall must not be so large as to create a cold wall section that would measurably alter the thermodynamic conditions. As a further condition, the probe head should be as modular as possible, so that a wide variety of optics can be used, for example to enable different FOV, different viewing directions or the use for other measurement techniques.

Over the course of this thesis, three of the developed probe-head designs were manufactured and applied to the respective test rigs for which the different designs were developed. The first version was designed for the NDP-1 test rig, and was used to demonstrate the general concept, while the next generation was used at the HBK-4 test rig to demonstrate the applicability under real test conditions. The results led to the final design for the CEC test rig, which allows the application at combustion pressures up to 1.6 MPa and a co-flow temperature of 870 K. Figure 4.1 shows the different designs and indicates the difference in size and complexity. Further details of each design are provided in the following desction.

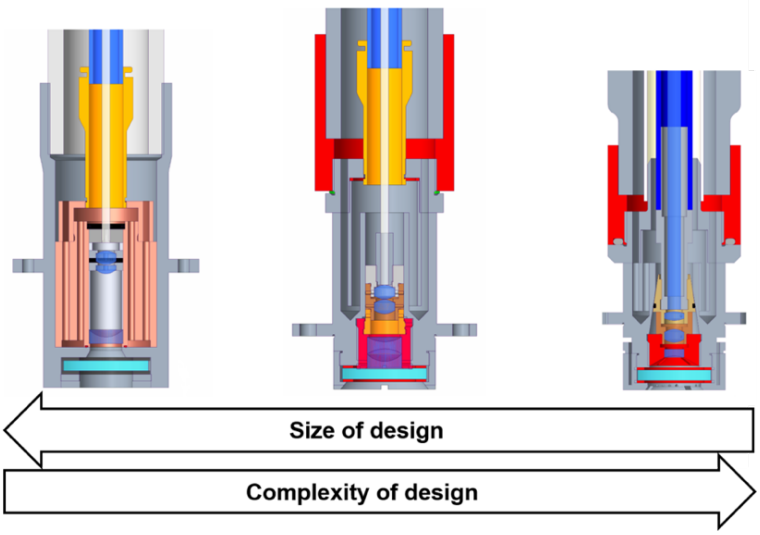

Figure 4.1: The developed main head designs of the fiber probe for the NDP-1 (left), the HBK-4 (middle), and the CEC (right) test rig and their relative size and complexity.

NDP-1 Design

The basic and common principle of all head designs is internal water cooling and the use of high-temperature alloys, the application of a material with high thermal conductivity for the optics holders and the use of a sapphire window at the probe tip. The design for the NDP-1 probe (hereinafter referred to NDP head) is the largest one with an outer diameter of 37 mm at the tip and an overall length – i.e., the distance from the tip of the probe head to the rear edge of the probe head – of 90 mm. A detailed cross-section with reference numbers and a part list are presented in Figure 4.2 and Table 4.1, respectively. The head comprises a main body (1), made of Alloy 800HT, a copper cooling insert (7) and a sapphire front window (4) of 3 mm thickness and an outer diameter of 25 mm. The cooling insert serves as the optics holder. The optics are interchangeable as the lenses and spacers (8–15) are loosely inserted into the cooling insert. The lens/spacer combination is held in place by a retaining ring (17) at the end of the optics section. The shown design is capable of accommodating optics with a maximum diameter of 10 mm. Regardless of the maximum FOV of the selected optics, the head allows for a maximum FOV of 50° due to the mechanical blocking of the shoulder which limits the optics holder section of the cooling insert in distal directions (in the cross section shown, the shoulder holds the first lens (8) in place).

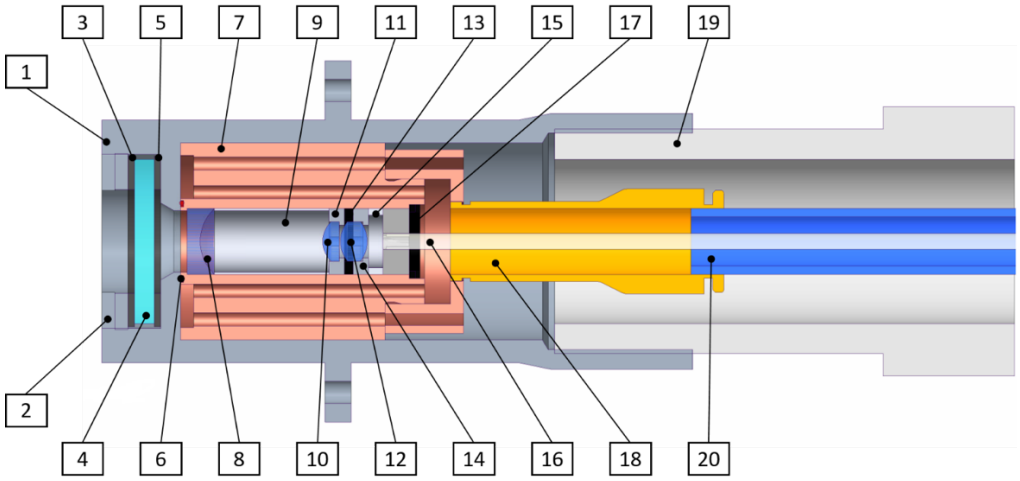

Figure 4.2: Cross-section of the NDP-1 head with annotations marking the essential parts of the head.

Table 4.1: Detailed part list NDP-1 head

Part number	Description	Part number	Description
1	Main body	11	Optics adapter
2	Window retaining nut	12	Fused silica lens
3	Graphite gasket	13	Spacer
4	Sapphire window	14	Optics adapter
5	Graphite gasket	15	Spacer
6	O-ring	16	Fiber bundle
7	Copper cooling insert	17	Retaining ring
8	Fused silica lens	18	Push-in fitting
9	Spacer	19	Connecting pipe socket
10	Fused silica lens	20	Inner tube

The head was designed to accommodate the *Fujikura FIGR 30k* fiber bundle with an outer diameter of 2.41 mm, thus allowing for an inner diameter for the inner tube (20) of only 15 mm. The main body features a self-sealing Whitworth internal thread for mounting the head to the connecting pipe socket (19), which features the corresponding outer thread.

In this concept, the cooling insert serves as a heat sink and guidance for the cooling water. For guiding the cooling water, the cooling insert possesses two rows of through holes, which are arranged on different diameters and extend from the rear end of the insert – the end facing away from the tip of the head – to the front end of the insert, whereby at the front end the two rows of holes are fluidically connected by a circumferential groove. The cooling water exits the push-

in fitting (18), enters the cooling insert through the inner row of holes, i.e., the row closer to the central axis of the cooling insert, and flows towards the tip of the probe. At the tip, the water exits the cooling insert, is redirected by the stop surface (the surface facing the cooling insert) of the main body and enters the cooling insert trough the outer row of holes, flowing towards the rear end, where it exits the probe head through the annular gap formed by the outer diameter of the inner tube and the inner diameter of the outer tube. The stop surface also serves as a stop for the cooling insert to fix the installation position. An O-ring (6), inserted in a circumferential groove, seals the optics arranged in the insert against the cooling water.

The head was tested at the NDP-1 test rig with chemiluminescence imaging and thermographic phosphorescence optics. As a consequence of the comparatively low thermal load on the NDP-1 due to the atmospheric combustion conditions and the cooling of the rig feedthrough (cf. section 4.4.1) itself, no water cooling of the head was required. The overall performance of the cooling head was found to be satisfactory, and the speed of the optics used was sufficient to detect flame position and size. The results of these measurements will be presented in section 5.2.2.
Simultaneously performed fiber-based thermographic phosphorescence measurements, which used a specifically adapted NDP-1 head in combination with a large single lens and a large-core single fiber, were not successful. An after-test inspection revealed some deposits on the first lens of the thermographic phosphorescence setup, leading to a significant noise addition to the signal. These deposits may originate from vaporized composites of the graphite gaskets as a consequence of insufficient cooling, as the water mass flow rate for the cooled feedthrough was temporarily below the minimum flow rate.

HBK-4 Design

The next head (HBK-4 head) was developed for the HBK-4 rig (cf. section 4.4.2) and was specified to be used at a rig pressure of 1.2 MPa and a co-flow temperature of 750 K, thus enabling the probe to be used in regular high-pressure combustion tests in the combustor development process. It was again designed for the *Fujikura FIGR 30k* fiber bundle and the corresponding input optics. In order to lower the impact on the experiments, the outer dimensions of the head, in particular the diameter of the tip, were reduced. As a consequence, the design was significantly altered. Figure 4.3 depicts the cross-section of the head with assembled optics (40° FOV) and Table 4.2 presents a detailed part list.

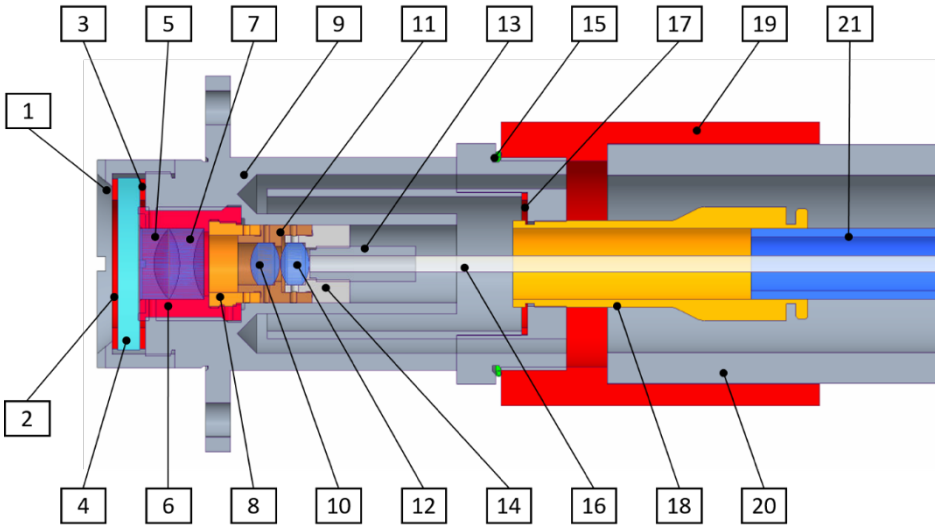

Figure 4.3: Cross-section of the HBK-4 head with annotations marking the essential parts of the head.

One measure was the integration of the cooling channels into the head's main body (9), thus rendering the copper cooling insert obsolete. The cooling channels were designed as arc-shaped slots at two different diameters, whereas the slots were separated by bars. In the vicinity of the probe tip, the cooling channels were fluidically connected by an annular cavity inside the main body as seen from the figure. To create the internal cooling channels, the probe was manufactured by selective laser beam melting, which enables the creation of complex internal structures. For this purpose, the corresponding allowances were considered when creating the 3D model, which served as a template for the manufacturing process. The shape of the distal end of the annular cavity had to be triangular due to the use of this additive manufacturing process. The main body consists of two parts to accommodate the graphite gasket (17). After the manufacturing of the raw body, the body was then machined to create the required functional surfaces, for example the threads and sealing surfaces. The two parts were then welded together. As a result of the incorporation of the cooling channels into the main body and the application of additive manufacturing, the outer tip diameter was reduced to 30 mm and the length shortened to 80 mm. The main body was made of the high-temperature alloy Hastelloy X to ensure safe operations (melting temperature range 1260–1355 °C) [98] and comparable thermal expansion as certain parts of the combustor hardware and the corresponding adapter (see section 4.4.2) are made from the same material.

Table 4.2: Detailed part list HBK-4 head

Part number	Description	Part number	Description
1	Window mount	12	Fused silica lens
2	Graphite gasket	13	Fiber adapter
3	Sapphire window	14	Optics adapter
4	Graphite gasket	15	Metal O-Ring seal
5	Fused silica lens	16	Fiber bundle
6	Optics adapter	17	Graphite gasket
7	Fused silica lens	18	Push-in fitting
8	Adjustment spacer	19	Connecting pipe socket
9	Main body	20	Neck outer cooling hose
10	Fused silica lens	21	Inner cooling tube
11	Optics adapter		

As consequence of the missing cooling insert, the optics were now directly mounted into the head with the help of small optics adapters and spacers (6, 8, 11, and 14). Each adapter was customized to the lenses in terms of diameter, shape, and distance to the next optical surface. The adjustment spacer (8) ensures the correct distance between the first pair of lenses (5, 7) and the second pair of lenses (10, 12). All adapters have narrow side holes to fix the lenses in place using a thermosetting two-component adhesive. In order to adjust the optics, the first optics adapter (6) and the adjustment spacer (8) as well as the rear optics adapter (14) and the fiber adapter (13) are each provided with an internal and an external fine thread, respectively, so that the distance of the first lens pair to the second lens pair and the distance of the input optics to the front surface of the fiber bundle can be adjusted. Furthermore, the first lens holder (6) features an external thread to mount the combined lens stack into the main body. All holders and spacers were made of AMPCOLOY 91 instead of copper, as this material benefits from a high elastic modulus of 130 GPa and an enhanced machinability, while still featuring a high thermal conductivity of 208 W/mK [99]. The front sapphire window (4) was, together with two graphite gaskets (2, 3), placed inside a separated window mount (1) and reduced to a diameter of 20 mm to account for the smaller diameter of the head. Another design change was the connection between the main body (9) and the connecting pipe socket (19), for which a pressurized metal O-ring seal (15) was chosen instead of a self-sealing thread.

The probe was used during a day of high-pressure testing at the HBK-4, but was already damaged during installation, partly due to certain design flaws, and partly due to handling errors so

that no successful measurements were carried out. However, since the probe was mounted during the entire test day, valuable findings for improving the overall probe design could be obtained in a subsequent inspection.

CEC Design

The probe head design for the CEC test rig (hereinafter referred to as CEC head) represents the final design of the probe head developed as a part of this dissertation. The design, like the HBK-4 design, was based on a Hastelloy X head manufactured by selective laser beam melting featuring internal cooling structures. The changes made to the design were based on the one hand on the changed boundary conditions which were expected during the experiments at the CEC. On the other hand, the adaptations were based on the experience gained during the tests of the HBK-4 design under high-pressure conditions and the thorough inspection of the probe afterwards. A cross-section of the design is shown in Figure 4.4 and a detailed part list is presented in Table 4.3.

During the experiments at the CEC, rig pressures of up to 1.6 MPa and temperatures of up to 750 K were expected. In addition, the position of the probe inside the combustor hardware was moved closer to the primary reaction zone of the flame to adapt the viewing angle to the changed hardware. The results of these changes were higher demands regarding pressure load and cooling capacity of the probe, in particular of the probe head. To increase the pressure load capacity, the connection between the head and the outer hose was improved by enlarging the diameter and thickness of the metal pressurized O-ring (13) and adapting the O-ring gland accordingly. In addition, the sealing interface design was modified as the O-ring gland was incorporated into the hose/head connector (14). A shoulder on the main body (11) was configured as the corresponding sealing surface of the O-ring and provided with the required surface finish. To apply the required mounting force, the aforementioned shoulder was provided with two opposing mounting surfaces to allow for an easy use of an open-end wrench during assembly. The modifications considered a possible negative pressure gradient, which occurs when the pressure inside the test rig, i.e., the combustion pressure, exceeds the internal cooling water pressure of the probe ($p_{comb} > p_{probe}$).

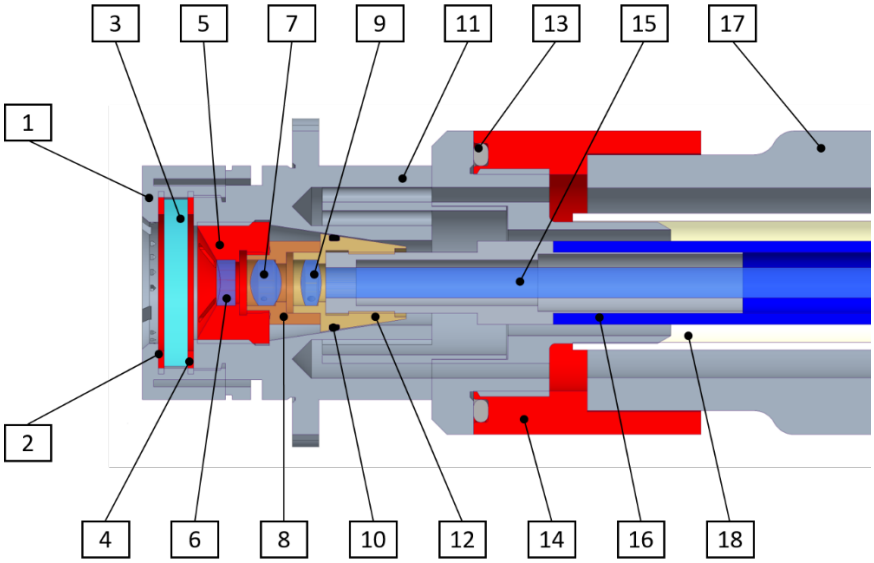

Figure 4.4: Cross-section of the CEC head with annotations marking the essential parts of the head.

To increase the cooling capacity of the probe tip to in order to account for the new mounting position, nitrogen cooling was implemented, which was also used to provide a nitrogen cooling and purging curtain for the sapphire window (3). To maintain the general design, an external supply through the adapter piece (see section 4.4.3) was chosen and thus, no modifications to the water channel design inside the main body were required. Moreover, this solution allows for nitrogen cooling for the adapter piece itself. As depicted in Figure 4.4, two lateral arcuate slots were provided in the main body through which the nitrogen can enter the main body. The nitrogen is then directed through the cooling channels provided in the main body and in the window mount (1) to the multiple outlet openings. Since the nitrogen flows into the combustion chamber, a minimum excess pressure of 0.5 MPa to the combustion pressure is mandatory ($p_{N_2} = p_{\mathrm{comb}} + 0.5\ \mathrm{MPa}$).

To further reduce the thermal load on the tip, the front surface of the window mount was provided with a protective layer of thermal barrier coating (TBC).

Table 4.3: Detailed part list CEC head

Part number	Description	Part number	Description
1	Window mount	10	O-ring seal
2	Graphite gasket	11	Main body
3	Sapphire window	12	Conical optics adapter
4	Graphite gasket	13	Metal O-ring seal
5	Optics adapter	14	Hose/Head connector
6	Fused silica lens	15	Fiber bundle
7	Fused silica lens	16	Fiber bundle pressure shell
8	Optics adapter	17	Neck outer cooling hose
9	Fused silica lens	18	Inner cooling tube

From the experience at the HBK-4, it could be inferred that the poor performance of the probe was due to insufficient flexibility. On the one hand, the applied fiber bundle proved to be too stiff, causing it to be damaged during installation of the flow box cover (see chapter 4.4.2), and on the other hand, the length of the probe head and the connector caused the probe head to tilt in the adapter piece. High mechanical force was required to move the head into the final mounting position, eventually damaging the front window of the probe.

The first reason was addressed by using the *Nanjing 20k* fiber bundle in the CEC design. This fiber bundle, as already described in chapter 3.2, is only glued together at the respective ends, and therefore offers greater flexibility or a significantly reduced minimum bending radius, respectively. However, the absence of a protective outer resin layer required an impervious outer hull. As consequence, the bundle has an outer diameter of 9 mm and 12 mm in the region of the two ends of the bundle, to each of which an external fine thread was attached. The larger diameter required the use of a larger inner cooling tube (18). The newly selected inner cooling tube had an inner diameter of 16 mm, as a result of which no push-in fitting was available to connect the tube to the head, due to the constraint of the maximum outer diameter of the head. Accordingly, an extension piece was provided instead at the proximal end of the main body, onto which the inner cooling tube can be plugged when assembling the probe. When using the *Nanjing* bundle together with the associated optics, it was found during a lab test of an intermediate design that the previous sealing concept of the optics section was inadequate and cooling water could enter the optics if the cooling water pressure exceeds a certain threshold (approximately 1 MPa). To enhance the sealing of the optics portion against the cooling water, the proximal

optics adapter (12) was redesigned, featuring a housing gland for an O-ring (10) and a conical shape. The required sealing force is provided via the outer thread of the first optics adapter (5), which features mounting slots at its front surface for a spanner wrench.

To avoid or lower the risk of tilting during the installation of the probe, the length of the head and the length of the hose/head connector (14) were shortened. The head in particular was shortened considerably, so that the entire length of the head, i.e., the main body plus the window mount, could be reduced to 66 mm.

4.3 Cooling Body and Water supply

When using flexible fiber-based probes on high-pressure test rigs, the probe cooling body plays an essential role. On the one hand, the cooling body enables the application of the sensitive fiber bundles, which have a maximum operating temperature of around 350 K, in a high-pressure combustion test rig, where high temperatures regularly prevail in addition to the high pressures. On the other hand, the geometry and the flexibility of the cooling body partly determine the resulting flexibility of the probe.

The predominantly used rigid probes, which are formed by two concentric pipes, allow efficient cooling and easily calculable fluid mechanical and thermodynamic conditions, but limit the use of the probe at different feedthrough positions or at different test rigs. Therefore, an alternative cooling body design was developed. The new probe consists of a previously presented head, a cooling body, and a water supply portion.

The improved flexibility of the probe results from the design of the cooling body, which for this purpose consists of two concentrically arranged tubes operating as a tube-in-tube heat exchanger. Here, the cool water coming from the cooling circuit of the test rig flows through the inner tube and thus along the fiber bundle towards the head, where it is diverted into the internal cooling channels and then flows back to the water supply portion in the annular gap formed between the inner and outer tube, absorbing most of the heat load. To withstand the harsh environment within the test rig, the outer tube is a corrugated metal hose. The inner tube is made from polytetrafluoroethylene for improved flexibility. The heat load to be absorbed by the probe is determined by the intrusion depth of the probe, the position of the probe head in relation to the flame, the temperature of the co-flow and the speed at which the co-flow passes along the probe. In total, the required cooling power for the probe was estimated to 69 kW, including a safety margin.

At the proximal end of the cooling body, the water supply portion is located, in which the connection for the cooling water inlet and the cooling water outlet are arranged together with thermocouples for monitoring the respective water temperature. Furthermore, a feed-through for the fiber bundle is provided at the rear end of the water supply portion, which is sealed with a stuffing box. An example of a water supply portion (the HBK-4 design) is presented in Figure 4.5. The flow direction of the cooling water is indicated by arrows.

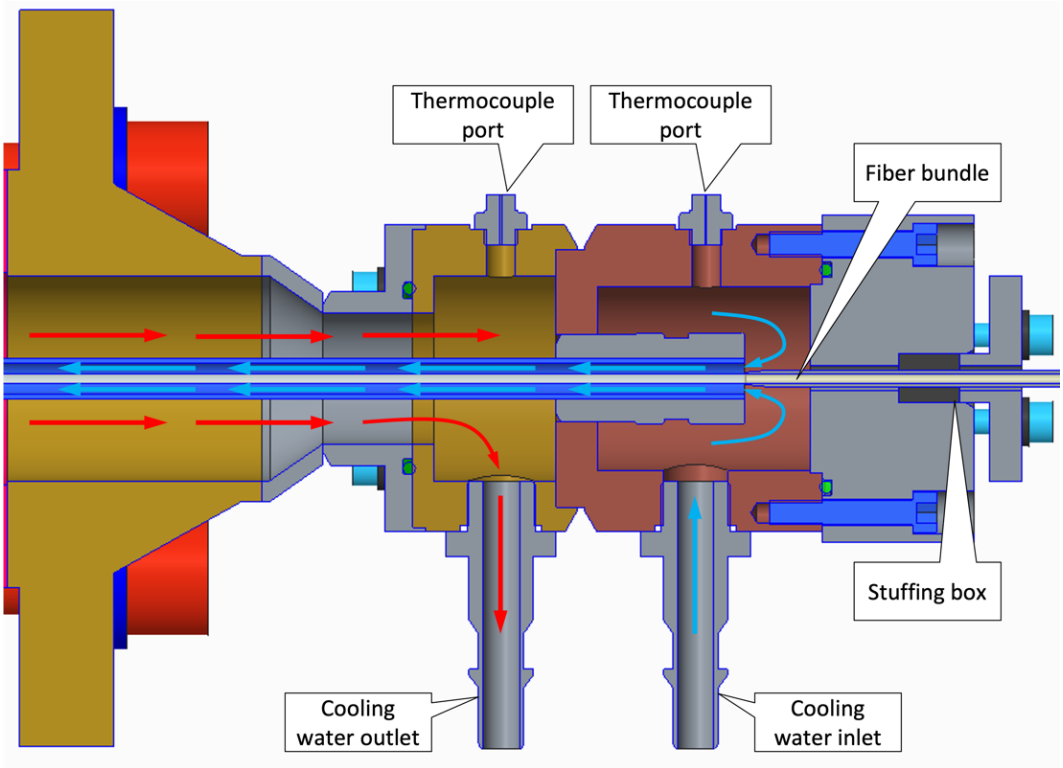

Figure 4.5: Water supply portion of the HBK-4-design with the flow direction of the cooling water indicated by blue (cold water) and red (hot water) arrows.

Another task of the cooling body or the probe head is to seal the probe access at the test rig. The sealing concept for the NDP-1 is based on a simple flat gasket arranged between the sealing surface on the probe head and the sealing surface of the insert, with the necessary sealing force being generated by four screws. The assembled probe is shown in Figure 4.6.

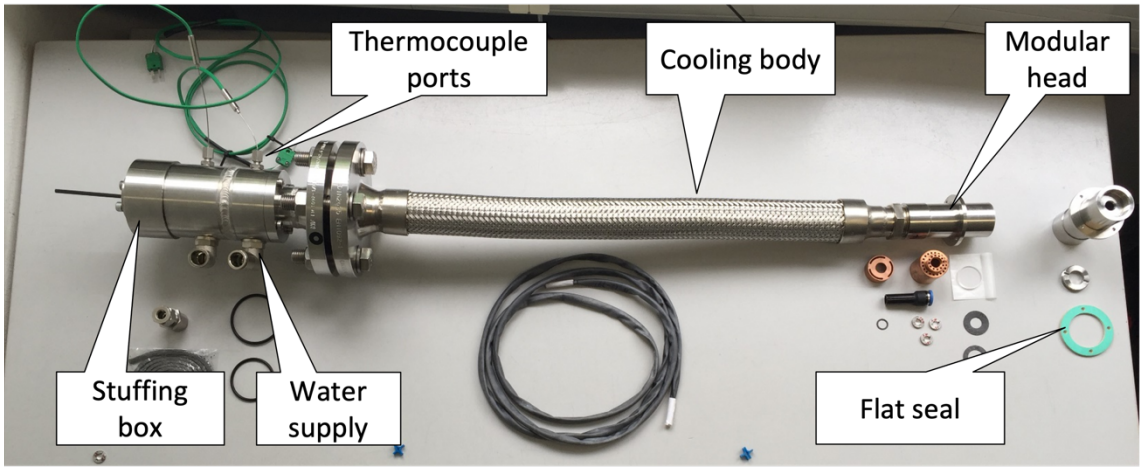

Figure 4.6: Assembled probe for the NDP-1.

The sealing concept of the HBK-4 probe is also based on a high-temperature flat gasket, but it is arranged between the manhole cover of the test rig and the distal flange (also referred to as sealing flange) of the cooling body (see Figure 4.7). The sealing force is generated by four M20 bolts screwed directly into the cover.

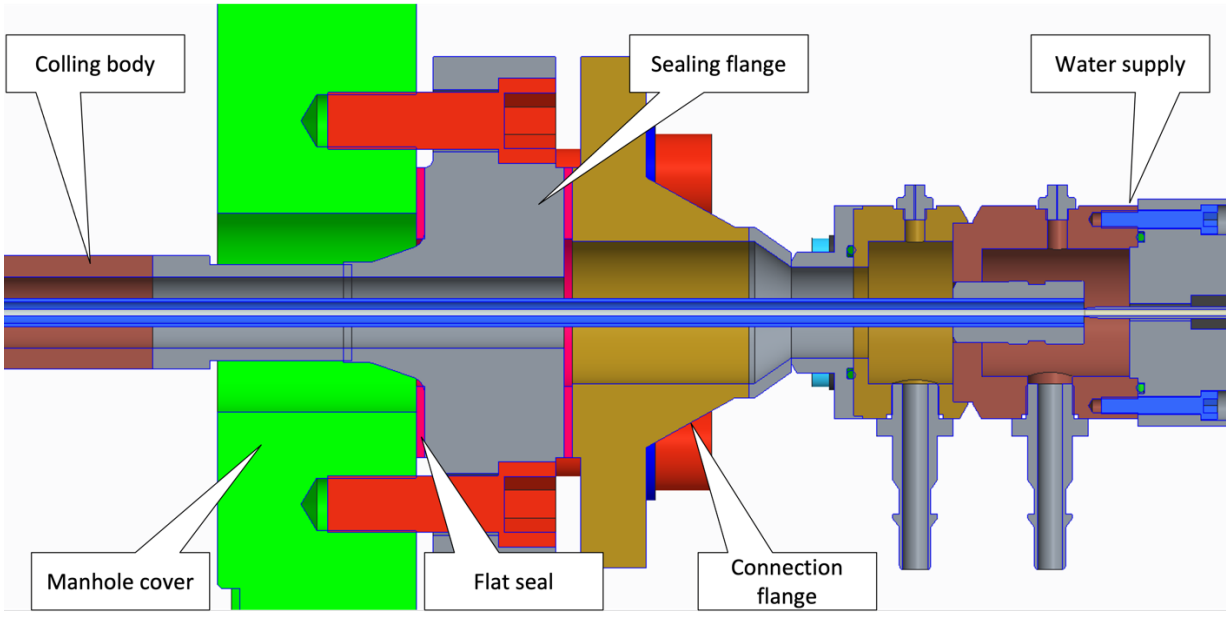

Figure 4.7: Sealing concept for the probe feed-through at the HBK-4.

This sealing concept requires a two-stage assembly of the probe, during which the probe head and the cooling body have to be mounted first followed by the water supply portion. The cooling body and the water supply portion are connected via a flange interface consisting of the sealing flange of the cooling body and a connection flange at the water supply portion. To adjust the

intrusion depth of the probe, spacers of certain lengths may be placed between the manhole cover and the sealing flange.

Based on the experience with the sealing system of the HBK-4 probe, the sealing concept of the CEC probe was improved and changed to a stuffing box whose radial sealing surface is provided by a rigid section of the cooling body of the probe, as can be seen in Figure 4.8.

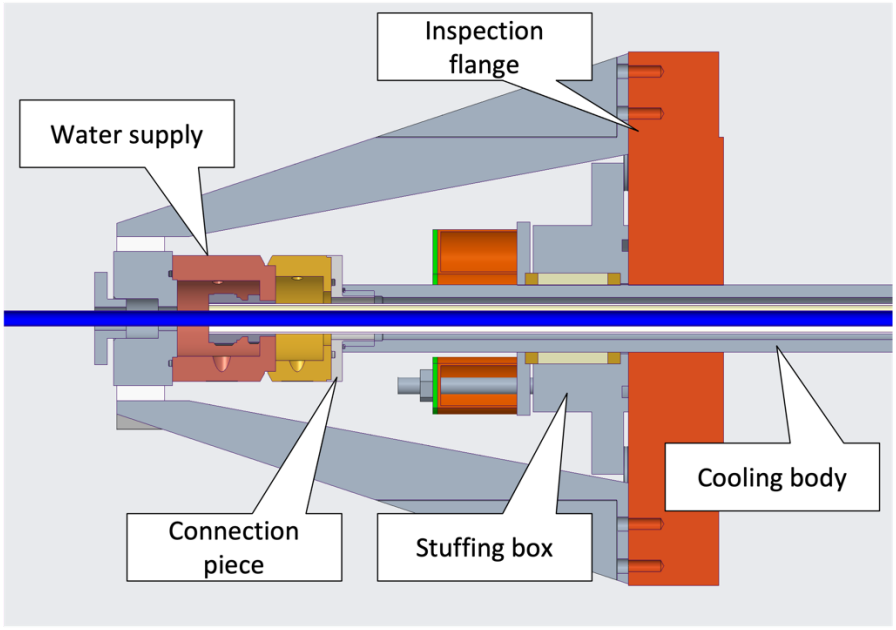

Figure 4.8: Sealing concept for the probe feed-through at the CEC.

This simplified the assembly process by allowing the probe to be fully assembled first and then to be mounted to the test rig. In consequence, the connection of the cooling body and the water supply portion was altered to a threaded connection consisting of a connection piece with an outer M30 thread, which is mounted to the water supply portion, and the corresponding inner thread at the distal end of rigid portion of the cooling body. The connection is sealed by an O-ring. The complete CEC probe is shown in Figure 4.9. To avoid modifications to the cooling body and the water supply portion, the nitrogen cooling for the head and the sapphire window was not integrated into these parts but rather into the adapter, which holds the probe head in place (see section 4.4.3). In consequence, a flexible metal hose with an outer diameter of 16 mm is guided alongside the cooling body when the probe is installed in the test rig.

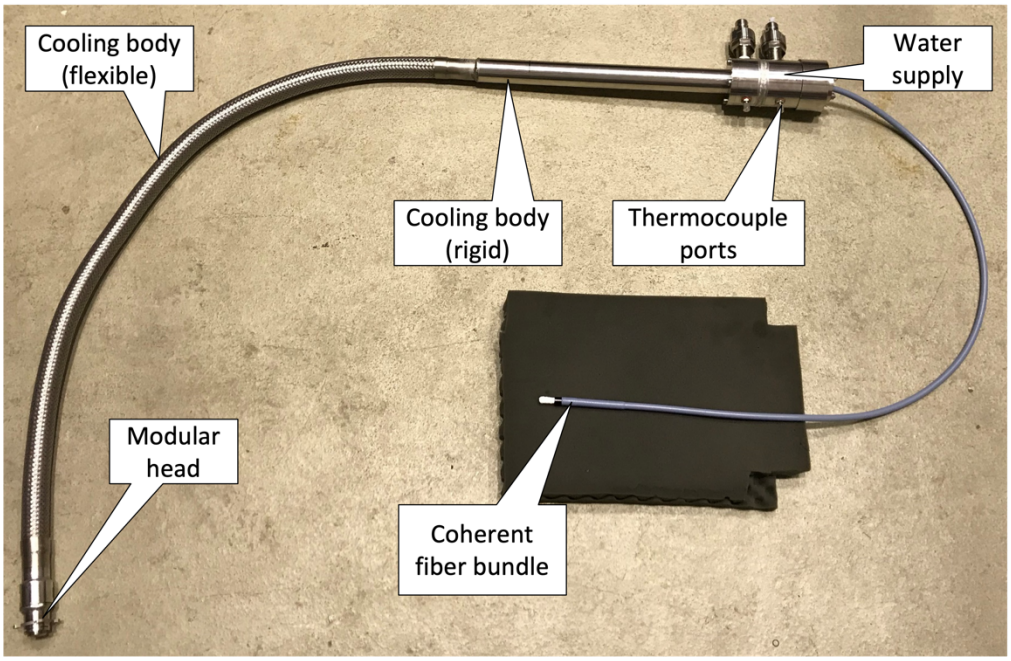

Figure 4.9: Assembled probe for the CEC.

4.4 Test Rig Access

Within the scope of this work, several test rigs were used to conduct the experiments presented in chapter 5. All of them have in common that they are designed to hold and support unscaled gas turbine combustors and, in some cases, provide real-engine thermodynamic boundary conditions and mimic the mid-frame section of the engine under investigation. The used test rigs were the atmospheric NDP-1 rig at the Siemens test facility in Mülheim a.d.Ruhr, the HBK-4 at the DLR in Cologne, and the CEC rig at the Siemens test facility in Ludwigsfelde. In the following chapter, the developed concepts for the implementation of the fiber-based probe as well as the modifications made to the respective test rig are presented.

4.4.1 NDP-1

The first modified test rig was the atmospheric NDP-1. It was used to test and demonstrate the newly developed fiber-based optics and to conduct numerous chemiluminescence imaging studies. The major advantages of this test rig are the existing optical access and the easy adaptability of fiber optics to the test rig. In addition, the air and gas mass flow rates are scaled to atmospheric conditions, thus reducing the costs of testing, and increasing the rig availability.

The rig, shown in Figure 4.10, is fed by an external fan, providing a maximum air mass flow of 1.2 kg/s air, externally preheated to a maximum inlet temperature of 720 K. The maximum gas mass flow is 0.1 kg/s of natural gas. The combustion test rig vessel is lined inside with a ceramic layer and the exhaust portion, i.e., the conical duct and the exhaust stack, features water cooling and air cooling, respectively.

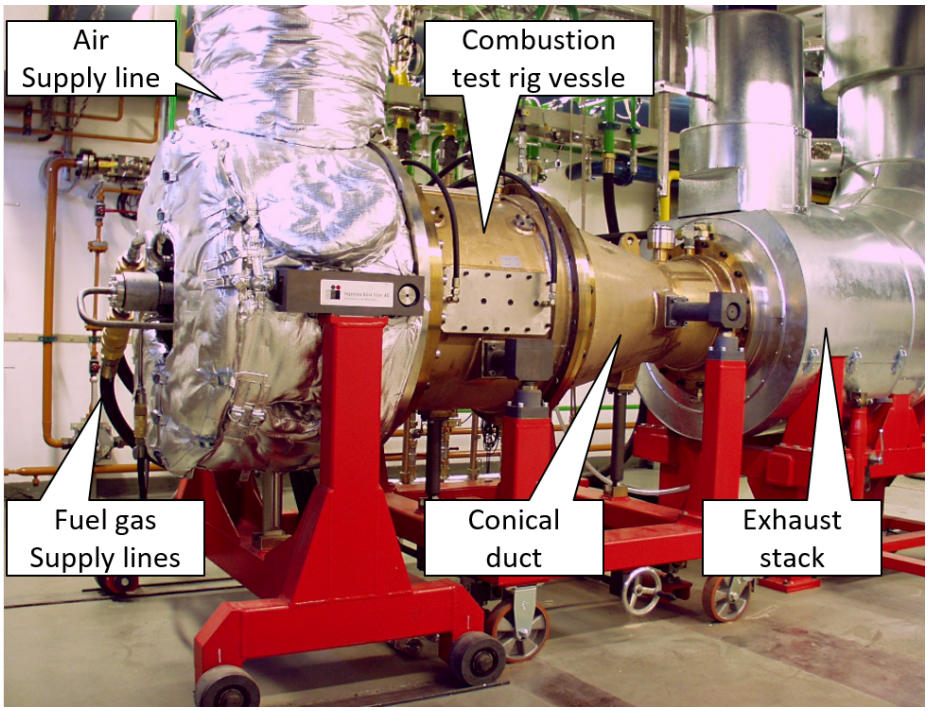

Figure 4.10: NDP-1 combustion test rig at the Siemens test facility in Mülheim a.d. Ruhr [100].

The rig was designed to hold one unscaled burner of the SGT5-4000F frames (see Figure 5.4 in section 5.2.2). An air inlet labyrinth mimics the engine compressor exit diffusor to replicate the incoming engine-like flow conditions, while the exhaust gases are guided into the exhaust stack by the conical duct, without a guide vane simulation section. To reduce the thermal load of the chimney, the exhaust gases are diluted with preheated air.

Optical access is available via two optical windows in the test rig, one in the side wall of the vessel and a second one in the exhaust stack. The first or side window is water-cooled and made out of fused silica, featuring a clear width of 286 mm and clear height of 114 mm, while the second one is made out of sapphire with a clear diameter of 140 mm. These two access points allow for a side and a perpendicular view of the flame. The location of both windows in relation to the burner position is visible in the cross-section of the NDP-1 in Figure 4.11.

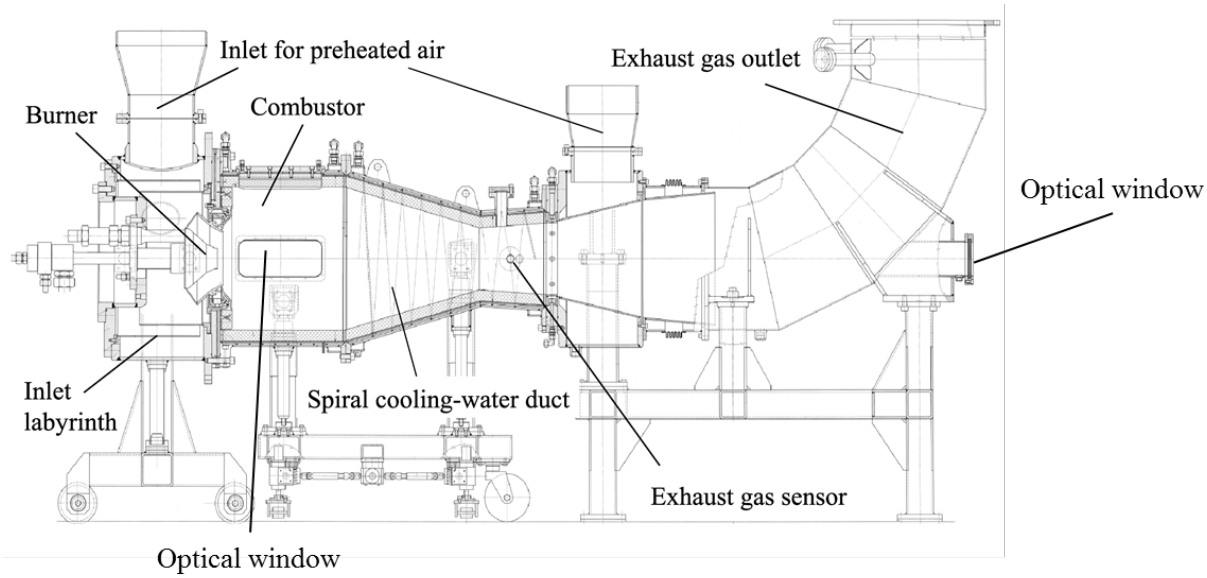

Figure 4.11: Side-view cross-section of the NDP-1 test rig [100].

Fiber-based optical access was realized by replacing the side window by a cooled inset (Figure 4.12), enabling flame observation with customized fiber-based optics and allowing for a validation of the probe head design. The two-part inset is water-cooled and directly integrated into the NDP-1 cooling circuit as a substitute of the side window. It consists of an outer chassis (5), which reproduces the outer geometry of the side window frame, and an inner plate (2). The latter has two inlet connection sockets (1) and two outlet connection sockets (4) for the integration of the inset into the cooling circuit of the test rig. The inset is installed in such a way that the side of the cooling water inlet is closer to the burner exit plane and the cooling water thus flows through the inset in the direction of the flow inside the test rig. To reduce flow-induced losses and to increase the heat exchange between the inset and the cooling water, the outer chassis features inner struts on its base surface, i.e., the surface facing the inner plate when the inset is assembled. Moreover, a protective layer of thermal barrier coating on the outer base surface of the chassis, i.e., the surface facing the flame, reduces the heat introduction of the flame into the inset.

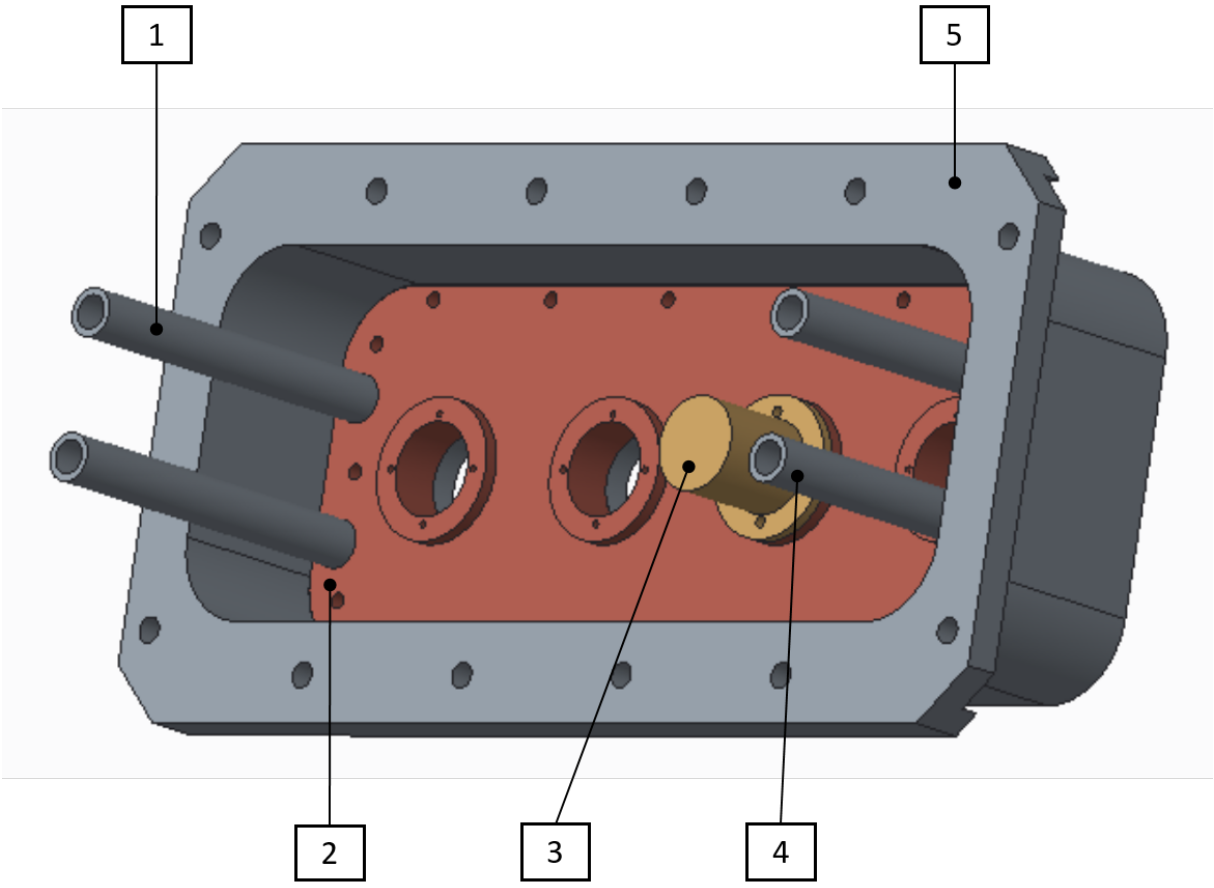

Figure 4.12: Fiber-port inset for the NDP-1 test rig.

The inset allows the use of up to four optical probes, each with a diameter of 37 mm, to accept the NPD-1 head design, at an axial distance (from centerline to centerline of each installed head) of 80 mm. The centerline of the fiber ports is aligned with the centerline of the combustor when installed. During testing, the probe head is mounted flush with the inner wall of the inset to avoid flame perturbance. Customized flat seals prevent the intrusion of ambient air into the combustion chamber. A dummy (3) is installed in the figure to represent one probe head.

4.4.2 HBK-4

The next modified rig was the HBK-4 high-pressure combustion test rig at the German Aerospace Center (DLR) in Cologne, Germany. The rig features an optical port for an existing rigid fiber probe, which was used in the first chemiluminescence experiments in 2013 (cf. section 5.3) and was later modified for a first feasibility study of the newly developed flexible probe in 2016. In contrary to the NDP-1, the HBK-4 allows for high-pressure testing up to the certified vessel pressure of 2.0 MPa with engine-like thermodynamic boundary conditions and an improved validity of the results with regards to real engine combustors.

The facility at the DLR possesses external compressors and air preheaters to provide pressures up to 4.0 MPa and inlet temperatures up to 980 K at an air mass flow of 45 kg/s. With the adjustable backpressure valve, the operation at different pressure levels is possible. Figure 4.13 shows an overview of the test facility with the HBK-4 rig installed.

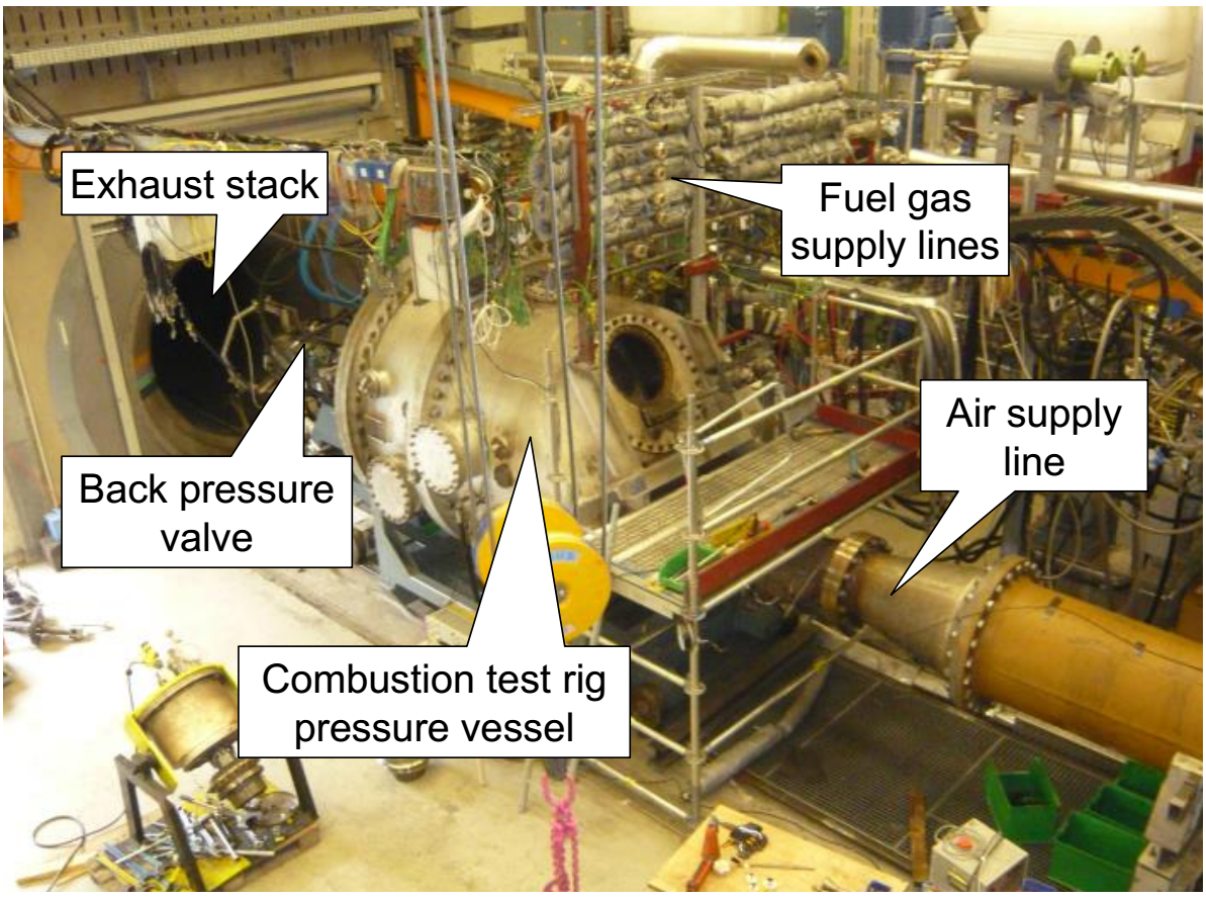

Figure 4.13: High-pressure combustion test facility at DLR.

The combustion test rig consists of a flow box installed in a pressure vessel. The flow box mimics relevant features of the gas turbine mid-frame, e.g., the compressor exit diffuser, the burner inflow, the combustion chamber (depending on the burner to investigate), the outlet as well as the guide vane of the turbine via a guide vane simulation section. The flow box is interchangeable to enable the representation of different gas turbine frames. A sketch of the test rig with the installed SGT6-8000H flow box and combustor is shown Figure 4.14, along with the position and resulting viewing angle of the rigid probe used. Furthermore, the figure presents the location of the pressure transducers.

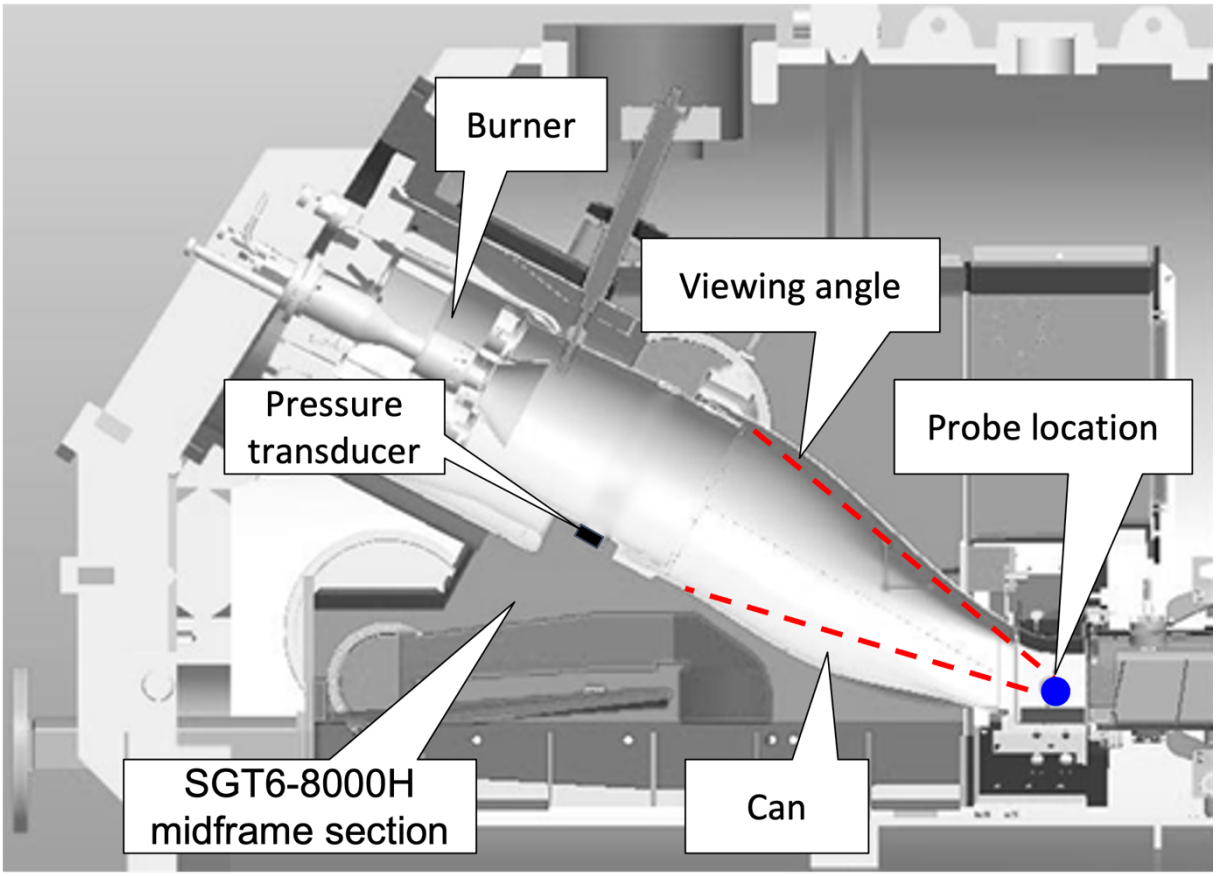

Figure 4.14: Location of the probe and resulting viewing angle for the setup including the rigid probe at the HBK-4 [16].

The use of the flexible probe required numerous modifications to the HBK-4 rig, yet on the premise of minimal intrusion and compliance with safety regulations. A total of four parts was modified: the combustor liner, the flow sleeve, a side lid of the flow box, and a manhole cover of the pressure vessel. Figure 4.15 shows a side view and a perspective top view (partially sectioned) of the rig with the probe installed as well as the viewing angle and the resulting field of view (yellow). The first two parts to be modified belong to the combustor hardware under investigation, which thus were irreversibly modified. In contrast, spare parts were manufactured for the latter two parts, which belong to the test rig itself, allowing easy replacement during test preparation.

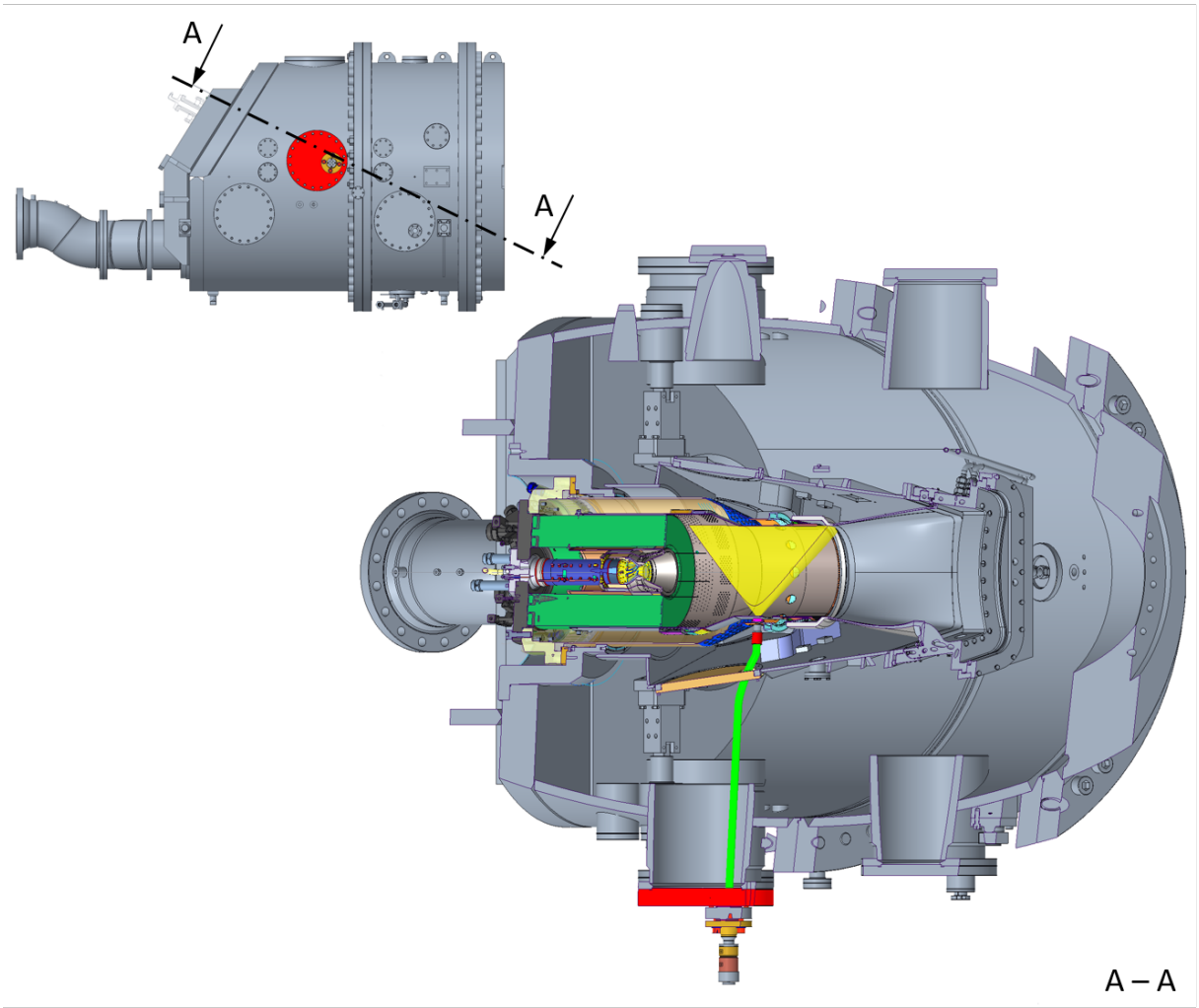

Figure 4.15: Side view and cross section of the HBK-4 rig with probe assembled. The resulting viewing angle is indicated in yellow. The probe is fed through the manhole cover (red) and the flow box lid (gold).

To enable optical access to the flame inside the combustor, a circular hole of 30 mm in diameter was laser cut into the liner. To mount the probe head to the liner, an adapter was fabricated and welded to the liner. The adapter has an inner diameter of 31 mm to accommodate the probe and two lugs provided with M4 internal threads to tighten the connection of probe head and adapter. To seal the combustion chamber against possible leakage air from the flow box through this connection, a pressurized metal O-ring for high-temperature applications (made of Inconel X-750) is used, accommodated in a groove provided in the top portion of the adapter. The necessary sealing force is provided by two bolts tightened into the aforementioned lugs when the probe is installed. The deterioration of the elastic modulus of the O-ring due to high temperatures is compensated as the internal pressure of the seal increases with temperature. Since the base surface of the adapter facing the liner has to reproduce the outer contour of the liner, the

adapter was also manufactured by selective laser beam melting. The necessary thermal stability was ensured by the use of Hastelloy X. The height of the adapter was chosen in a way that the distal surface of the probe, i.e., the foremost surface of the window mount, is flush with the inner surface of the liner when the probe is installed, accepting small tolerances to account for the fact that the surface of the window mount is flat while the inner surface of the liner is curved.

An ellipsoidal feed-through slot of 40×52 mm was cut into the flow sleeve, the dimensions of which allow the probe head to be mounted, in particular the retaining bolts to be tightened, and also accommodate a possible difference in thermal expansion of the liner and the flow sleeve. A close-up view of the cutouts and the adapter welded to the liner is shown in Figure 4.16.

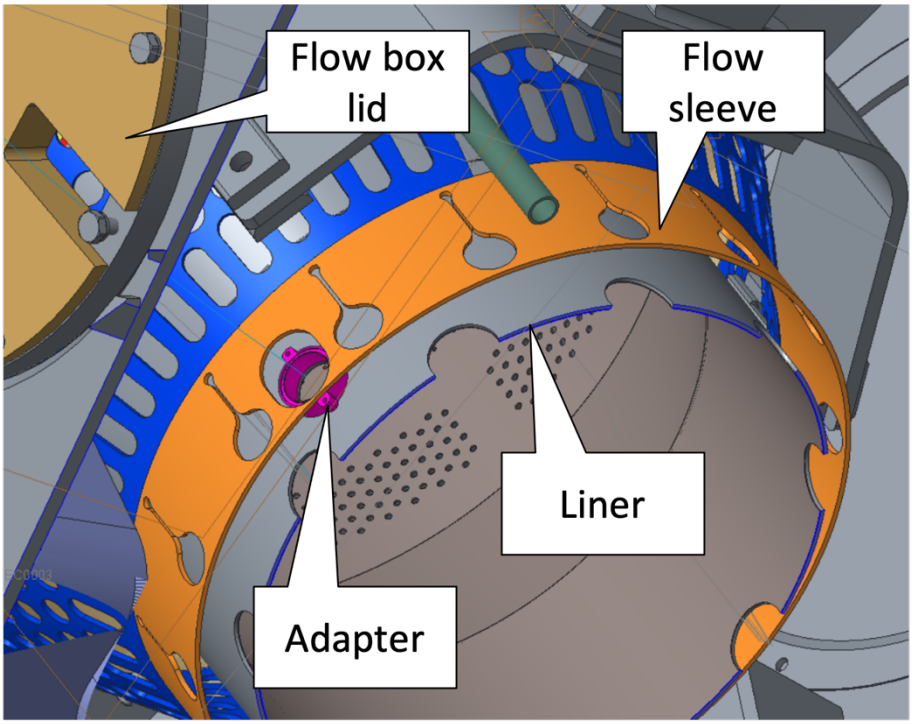

Figure 4.16: Close-up view of the probe head adapter welded to the combustor liner and the feed-trough slots in the flow sleeve and the flow box lid.

The feed-through slit in the flow box lid is also visible in Figure 4.16. The lid enables access to the combustor hardware and has an outer diameter of 448 mm. The pressure difference between the outer and inner side of the flow box is negligible and consequently, the sealing effort for the feed-through was kept low, thus reducing the port to a slit with a height of 40 mm and width of 100 mm. It starts from one edge of the lid, thus enabling the installation of the lid with the probe already mounted. The space of the slit not occupied by the probe was closed by means of a correspondingly shaped plug during the tests.

In contrast to the flow box lid, the pressure difference over the manhole cover regularly exceeds 1.0 MPa during testing, reaching a maximum of 2.0 MPa. Hence, this pressure difference had to be considered in the design of the probe feedthrough and the design of the replacement manhole cover. The redesigned cover has a diameter of 525 mm and a thickness of 70 mm. A hole with a diameter of 70 mm was provided as feed-through port for the fiber probe. The hole was located off-center with an offset of 127 mm from the middle axis, whereby allowing a variation of the axial position of the feed-through port by rotating the cover. The hole was surrounded by the four M20 threads for mounting the probe's cooling body to the rig (see chapter 4.3 for details on the HBK-4 probe design). The annular surface between these threads and the hole was prepared as sealing surface for the flat seal. As a consequence of these modifications, the thickness of the cover was increased by 28 mm to compensate the degradation of material strength.

4.4.3 CEC

The latest stage of the high-pressure rig design is the CEC rig located at the Siemens Clean Energy Center in Ludwigsfelde near Berlin, Germany. Like at the DLR, this test facility features external compressors and air preheaters to provide engine-like thermodynamic boundary conditions for the combustion test rig such as maximum rig pressures of 4.0 MPa, and a maximum air inlet temperature of 870 K at air mass flows of up to 50 kg/s. Figure 4.17 shows an overview of a test bed of the facility with the CEC rig installed. This rig also comprises a pressure vessel, an exchangeable flow box, which mimics all mid-frame engine features such as the compressor exit diffusor, and a turbine guide vane section. The pressure vessel can be used for different burner or engine designs by replacing the flow box. To account for the different engine pressure levels, the rig pressure is adjustable by a back-pressure valve.

The design of the optical access was based on the HBK-4 approach, yet significantly improved in consequence of the experiences gained at the DLR. In summary, the following improvements were made:

- Different feed-through positions for the probe
- Separable flow box lid with moveable bearing
- Increased head fixing onto the adapter
- Consideration of N_2 supply
- Stuffing box as pressure-resistant sealing with variable intrusion depth

One possible cause of the installation issues during the HBK-4 measurements was an insufficient tolerance of the inner diameter of the adapter in combination with the required tilting of the head due selected feed-through position. In order to avoid these issues, the location of the probe was moved downstream into the can (also referred to as transition) instead of the liner and thus into the rear-end of the pressure vessel through an inspection flange, as can be seen from Figure 4.18. Similar to the HBK-4 design, the combustor parts, i.e., the can, were subject to permanent modification while the inspection flange (red in the figure) and flow box lid (orange in the figure) were manufactured as spare parts.

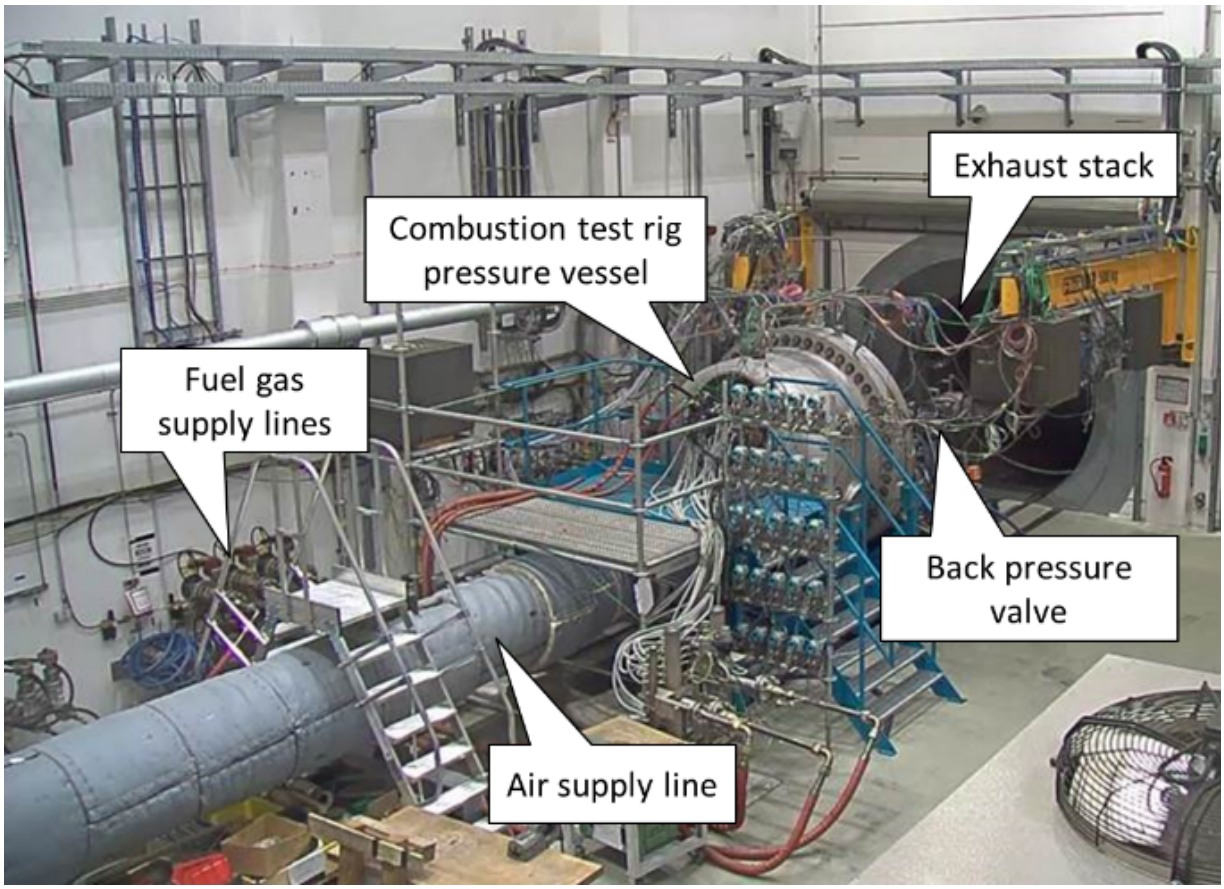

Figure 4.17: High-pressure test facility at the Siemens Clean Energy Center.

The chosen position in combination with the separable flow box lid enables a quasi-straight, mechanically stress-free assembling of the probe, without tilting the head. This allows for maintaining small fitting tolerances between the probe head and the adapter to reduce the impact on the combustor hardware and the experiments, in particular to prevent leakage air from the flow box from entering the combustion chamber through the adapter. In addition, the selected position limits the modification of the combustor hardware to the cutout for the optical access and the welding of the adapter onto the aforementioned. Moreover, the new feedthrough position

also prevents mechanical stresses acting on the probe, which were generated in the HBK-4 design by the different thermal expansion of the individual test rig components.

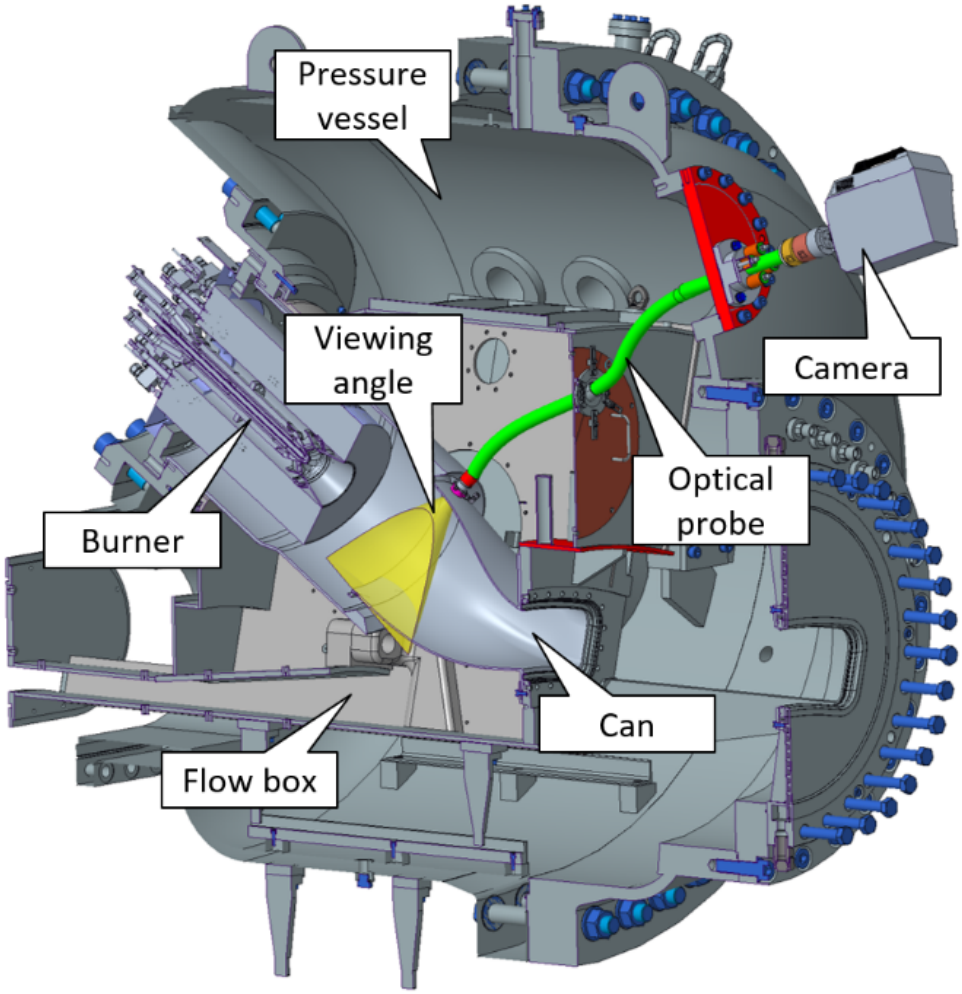

Figure 4.18: Perspective side view (cross section) of the CEC rig with probe assembled. The resulting viewing angle is indicated in yellow.

The parts involved in the insertion and mounting process of the head onto the can with the welded-on adapter are shown in the explosion view in Figure 4.19. The diameter of the cutout in the can was kept at 30 mm. The adapter has the same inner diameter and was again manufactured from Hastelloy X by selective laser beam melting. The contour of the bottom side of the adapter facing the can was again adapted to the corresponding contour of the can during printing of the adapter. As already mentioned in chapter 4.2, the adapter of the CEC probe design not only holds the probe head, but also provides the nitrogen supply. Accordingly, the adapter has a connection piece, internal cooling channels through which the nitrogen flows, and outlet slots whose position corresponds to the inlet slots of the probe head when it is installed in the adapter. For improved retention of the probe head in the adapter, as well as for providing

a more uniform force on the metal O-ring, which is again accommodated in a groove provided in the top section of the adapter, the adapter features four lugs with internal threads evenly distributed around its circumference.

The flow box lid was designed to consists of two parts. This has the advantage that the lid, which has a diameter of 500 mm when assembled, can be inserted into the pressure vessel more easily, and that the probe can be mounted first, followed by the installation of the individual lid halves and tightening to the respective opening in the flow box. Despite the two-part design, a comparatively large feed-through hole of 150 mm was provided in the lid, which is sealed with a movable bearing and is arranged off-center with an offset of 150 mm from the middle axis of the lid. Due to the resulting eccentricity, the feedthrough position, in particular the height in relation to the lower edge of the flow box, can again be adjusted by rotating the lid. The large hole allows for a free feed through of the probe and the nitrogen supply line, even if the head is assembled to the cooling body. A handle has been provided on each half of the lid to improve handling.

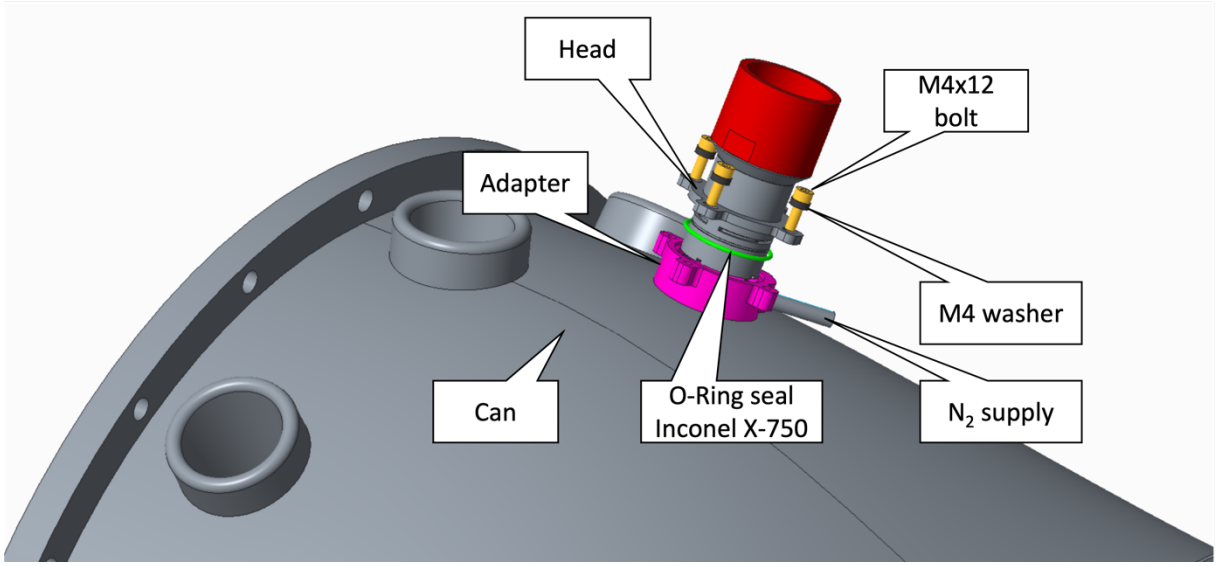

Figure 4.19: Head assembly

The moveable bearing holds the flexible probe and the nitrogen supply line by mimicking the angle of penetration and closes the hole in the flow box lid. While mounting and during operations the bearing is moveable as it is connected to the lid via moveable clamps, thus reducing the resulting stress due to thermal growth, however securely holding the probe and nitrogen supply line to prevent enforced vibrations introduced by the surrounding co-flow. Figure 4.20 presents the flow box lid, including the bearing as well as a section of the probe body and the

nitrogen supply line. As it can be seen from the figure, the bearing body (gray in the figure), which supports the probe and the nitrogen supply line, consists out of two parts as well, again for the sake of installing the bearing after mounting the probe to the can.

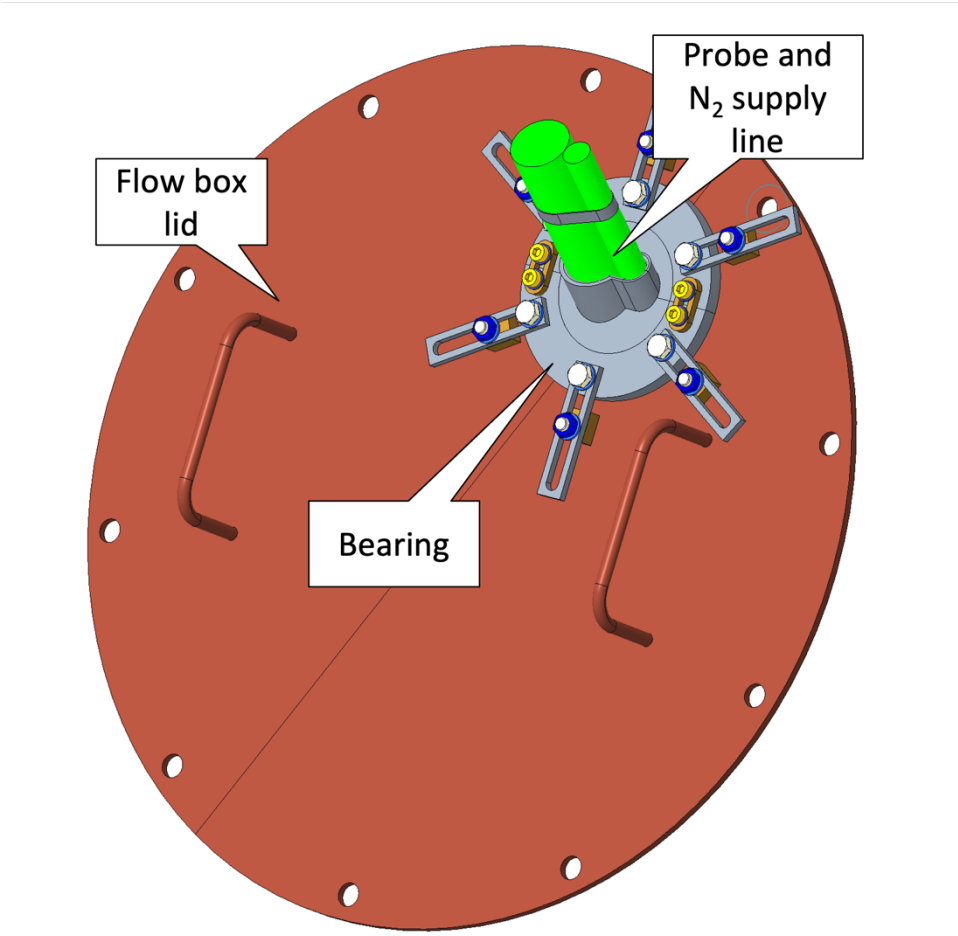

Figure 4.20: Flow box lid with movable bearing and installed probe and nitrogen supply line (both in green).

The inspection flange has an outer diameter of 500 mm and a maximum thickness of 60 mm. For the probe feed-through, an off-centered hole (127 mm off the flange's centerline) with a diameter of 40 mm was incorporated into the flange. Contrary to the flange-based sealing design of the HBK-4, the pressure vessel feed-through sealing approach for the CEC rig is based on a stuffing box, which can be directly mounted to the inspection flange. In combination with the rigid upper portion of the probe (see section 4.3), the box seals the port and allows for adjusting the intrusion depth of the probe. For mounting the stuffing box, the feed-through hole is surrounded by four M16 threads. To reduce leakage air, the stuffing box features a groove for a metal O-ring and the annular surface between the M16 threads and the feed-through hole

of the inspection flange was prepared as sealing surface, thus featuring the required surface finish.

4.5 Thermodynamic Performance

The CEC probe was deployed for two consecutive days of high-pressure combustion testing and showed a satisfying thermodynamic performance. During the test days, different test points were considered with rig pressures of up to 1.6 MPa and air inlet temperatures of 750 K at air mass flows of 32.5 kg/s. The probe was included into the cooling circuit of the test facility and the monitoring thermocouples in the cooling water in- and outlet together with a mass flow meter monitoring the cooling mass flow through the probe were integrated into the facility recording scheme and equipped with warning and emergency shutdown values, thus allowing for calculating the resulting cooling power and ensuring safety regulations.

A representative trace of the water in- and outlet temperatures and the corresponding water mass flow for a rig pressure of 1.6 MPa is shown in Figure 4.21.

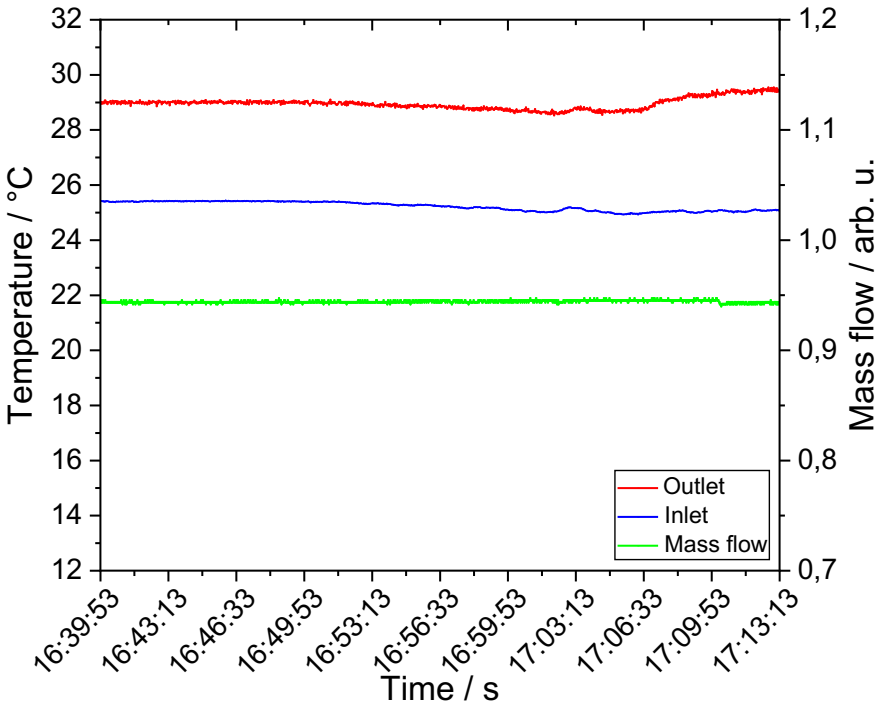

Figure 4.21: Example of cooling water mass flow, inlet, and outlet temperature during testing at 1.6 MPa.

It can be seen that the maximum temperature difference did not exceed 5 K at a quasi-constant water mass flow. In addition, the safety margin of the outlet temperature was found to be 45 K, indicating sufficient cooling for even higher compressor exit temperatures or an increased heat transfer due to higher air mass flows.

After the two days of continuous testing, the probe was inspected for signs of damage in order to determine its sustainability. In particular, the front window and the probe tip were of interest due to their close position to the flame, the resulting high thermal load and the experience from previous rigid probes. In these inspections, the sapphire front window showed no damage or opaqueness and the TBC at the tip was unaltered, as shown in Figure 4.22. Only the leading edge of the window mount showed a slight grey-bluish tarnish due to the high temperatures and temperature-induced oxidization by the remaining oxygen in the lean combustion.

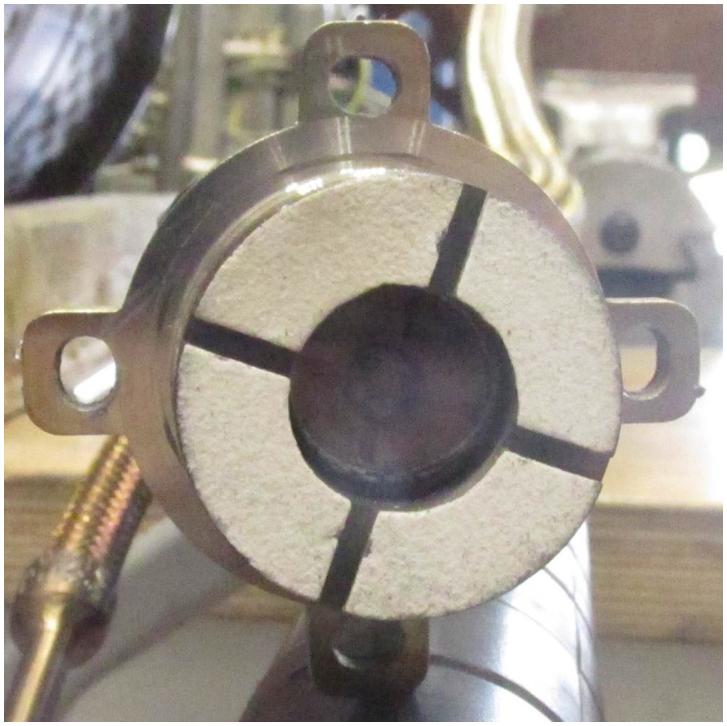

Figure 4.22: Probe tip after two days of continuous testing. The TBC and sapphire window remained unaltered.

Despite the overall good performance, it was found during the inspection, that the flat seal between the window mount and the sapphire window was displaced during the tests. The seal is visible at the bottom of the sapphire window in the figure above and might have caused a blocked area in the recorded chemiluminescence images (see Figure 5.17 in chapter 5.2.3).

4.6 Conclusions

In this chapter, the mechanical design process of a flexible, modular chemiluminescence imaging probe and the application to different industrial gas turbine combustor test rigs were presented.

It could be proven that fiber-based endoscopic imaging probes can be designed to withstand the harsh testing conditions during high-pressure combustion tests, enabling optical access at various feed-through positions while being flexible enough to compensate thermal expansion of the test rig. The final probe design incorporates the following key design features:

- Additive manufactured modular and exchangeable probe head to facilitate different optical setups and possessing inner cooling channels for water and nitrogen.
- Flexible tube-in-tube cooling concept based on an outside high-temperature, high-pressure flexible metal hose and a thin inner tube made of polytetrafluoroethylene.
- Flange-based feed-through approach with stuffing box, avoiding modifications of the pressure vessel and allowing for an adjustable intrusion depth.

The first version of the probe head was designed for the atmospheric NDP-1 test rig with a slightly larger head diameter. It was based on more rigid *Fujikura FIGR 30k* fiber bundles. With experiments at the NDP-1, the general design of a modular head could be tested. Active cooling of the probe was not necessary, due to the missing co-flow. Graphite flat sealing for the sapphire window were successfully used and kept as a design feature for the subsequently developed concepts.

The next evolution was designed for the HBK-4 test rig. Water cooling was introduced to the head's main body by additive manufacturing and the lenses were housed in holders made from AMPCOLOY 91. The design did not feature nitrogen cooling for the optics and the sapphire window. The rigid length of the probe head was 91 mm, thus leading, in combination with the geometry of the flow box lid and the chosen routing, to mounting difficulties. In conclusion, the finding was to reduce the rigid length and to aim for a rear end feed-through. Another drawback was the flange-based adaption of the probe to the test rig. This concept is easy to seal yet not flexible enough in mounting for the desired application.

Finally, the CEC design was derived, considering all former findings. The first change was the adjustment of the pressure vessel feed-through concept. It now uses a stuffing box with graphite

packing. Consequently, the insertion length is adjustable, and the assembling process is simplified. The next improvement was the rear end feed-through to reduce mechanical stress during the thermal expansion of the test rig. In combination with the newly designed flow box bearing, the probe was secured and protected from strong vibrations due to high co-flow velocities inside the flow box. To ensure the structural integrity of the sapphire window and the optics, nitrogen cooling was introduced. In order to achieve nitrogen cooling and to maintain the easy tube-in-tube design for the cooling body and water supply portion at the same time, the nitrogen feeding was incorporated into the head adapter, which was welded to the can. To further reduce the thermal load on the probe tip, it was coated with a protective layer of TBC.

All these features allowed the successful application of the probe during high-pressure testing up to 1.6 MPa rig pressure at a co-flow temperature of approximately 780 K and a maximum air mass flow of 32.5 kg/s.

The resulting cooling power was found to exceed 34 kW with a maximum water outlet temperature of approximately 305 K. Considering the maximum allowed outlet temperature of 350 K, the probe might have some cooling reserve. Higher co-flow temperatures or more challenging probe head locations seem feasible.

5 Chemiluminescence Sensing Applications for Industrial Combustor Tests

5.1 Introduction

Throughout this thesis, flame chemiluminescence measurements, both fiber-based and non-fiber-based, as well as fiber-based thermographic phosphor measurements were carried out at various unscaled industrial combustors under atmospheric and under high-pressure conditions, and at lab-scale burners, respectively.

The first high-pressure measurements were performed at the HBK-4 test rig at the DLR Cologne. An existing rigid probe, designed for a 50,000-pixel rigid fiber bundle, was used in combination with an intensified high-speed imaging system. The aim of this test campaign was the investigation of thermoacoustic instabilities in the SGTx-8000H combustion system. To enhance the prediction capabilities of the existing and the newly developed post-processing routines, additional chemiluminescence measurements of thermoacoustic instabilities of the SGT5-4000F combustion system were conducted at the NDP-1 in Mülheim a.d. Ruhr at atmospheric conditions.

The optics and flexible probe developed in the course of this thesis were used for the first time for chemiluminescence measurements to determine the flame position and flame length of the SGT5-4000F combustion system at the NDP-1 test rig. An intensified CCD-based detection system was used.

Lastly, the newly developed flexible probe was applied at the CEC rig at the CEC high-pressure test facility in Ludwigsfelde, near Berlin, during two separate test campaigns. The first campaign was directed at chemiluminescence flame sensing, using the flexible probe in combination with a flexible imaging fiber bundle and an intensified high-speed detection system. The second campaign aimed at wall temperature measurements with the thermographic phosphor technique, using a large core multimode fiber inside the flexible probe, an excitation laser for exiting the thermographic phosphor, and a photomultiplier tube as detection system. The campaigns investigated an experimental full-scale SGTx-8000H combustor (chemiluminescence flame sensing) and the designated combustor for the SGTx-9000HL engine (thermographic phosphor measurements).

In this chapter, details of the measurements are described. This includes a brief introduction to the testing procedure, the optical setup, and the different image post-processing routines. Afterwards, the exemplary results are presented and discussed.

In addition to the hindered optical access, endoscopic fiber-based chemiluminescence imaging often suffers from low SNR. In particular, hot parts and ceramic walls inside real gas turbine require narrow optical filters in order to discriminate the signal of the selected chemiluminescent species. Therefore, the aim of the first experiment at the NDP-1 was to test whether or not the selected optical system and post-processing routine allows for meaningful chemiluminescence recordings and results.

5.2 Flame Position and Length Measurements

Due to its comparative simplicity and robustness, chemiluminescence sensing and imaging allow the visualization of flames in a variety of industrial and especially in non-scaled high-pressure combustion test rigs. Its application offers additional possibilities, e.g., for the determination of flame ignition, flame propagation, flame length, flame position or for the investigation of flame-to-flame interaction in technical combustion systems. In addition to the pure investigation of the aforementioned parameters, knowledge of these also makes it possible, for example, to validate simulations of combustion in such combustion systems, more precisely to provide further data for validation [16, 31, 101–106]. In particular, the shape of the flames or the flame length are of interest and relevant for many technical applications. For example, the flame position and length determine the residence time and thus, the emission values [107–109] or the areas of the combustion chamber that require special cooling or ceramic shielding [3].

Despite the already widespread use of endoscopic chemiluminescence measurements in technical combustion systems, they still suffer from the problem of slow optics or low luminous intensity of the used optical systems [54, 65, 110], especially when using imaging fiber bundles [2, 54]. Therefore, in the context of this work, a new detection approach based on a threshold-based detection method was developed for the determination of the flame object from the acquired images, which also accounts for the image entropy for an improved determination of the flame object.

5.2.1 Post Processing

The applied fiber-based chemiluminescence detection allows for locating the flame position and determining its length if either targets or known geometrical structures inside the combustor are recorded before mapping the images. Beside the standard background correction, the images need to be corrected for the absolute magnification of the optical system and for the inner rotation of the fiber bundle.

For the background correction, a set of dark images was recorded prior to the respective image series. The set was averaged, and the average was subtracted from each recorded chemiluminescence image. The resulting magnification and inner rotation were corrected either by recorded targets or geometrical features inside the combustor.

For the NDP-1 measurements the burner exit lies within the field of view (FOV) and was used to detect the resulting magnification and inner rotation. No further image transformation was required.

A modified version of the Otsu thresholding method [111] was used to identify the flame object. The Otsu method allows for evaluating the "goodness" of the found threshold and showed good results in determining the flame area (e.g., [65]). The method splits the image into classes C_i, based on the gray-level histogram for an image containing pixels at L gray levels. For more details on the general method, the reader is referred to [111]. Otsu describes the "goodness" of a threshold k by one of the discriminant criteria [111, 112], defined as

$$\varepsilon = \frac{\sigma_{\mathrm{B}}^2}{\sigma_{\mathrm{T}}^2} \tag{5.1}$$

In equation 5.1 σ_B represents the between-class variance and σ_T the total variance of levels, respectively. With σ_B as a function of the threshold k, ε maximizes with the right threshold so that Otsu states the constraint for the optimal threshold k^+

$$\sigma_B^2(k^+) = \max_{1 \le k < L} \sigma_B^2(k) \tag{5.2}$$

For images with multiple thresholds, the upper statement can be extended to multiple classes C_i. The use of multiple thresholds is beneficial and necessary for images with structures of interest at different intensities, i.e., gray levels. For an example with two thresholds, resulting in three classes, the equation writes as

$$\sigma_B^2(k_1^+, k_2^+) = \max_{1 \le k_1 < k_2 < L} \sigma_B^2(k_1, k_2) \tag{5.3}$$

In such scenarios, as in the chemiluminescence images, the number of classes C_I strongly affects the goodness of a threshold, as shown in Figure 5.1.

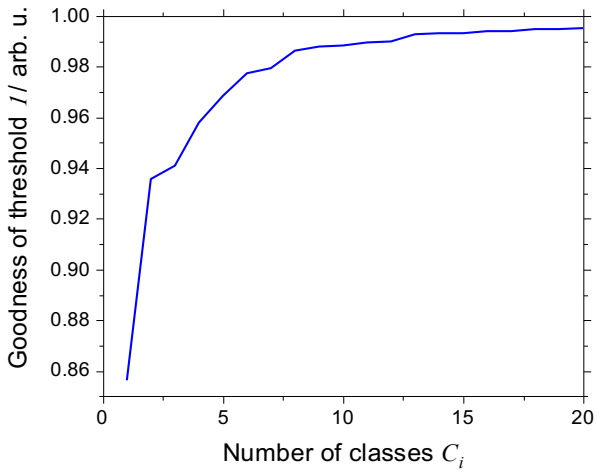

Figure 5.1: Goodness of the threshold as a function of the number of classes within the image shown in Figure 5.2.

As seen from the figure, ε rises with the number of classes C_i. Nonetheless, defining too many classes may deteriorate the determination of the flame length, as the physical meaning of the discriminant criterion $\sigma_{\mathrm{B,max}}$ decreases [111].

As the number of classes C_I increases, the goodness of the found threshold ε increases as well, yet no criterion is defined to evaluate the best threshold k_i^+ to represent the flame object within the recorded chemiluminescence images (see equation 5.2). This threshold is particularly crucial for an accurate determination of the flame length throughout an image series, as the overall intensity varies, for example, due to the architecture of the CMOS detector and its sensitivity variance as a function of ambient temperature or between readout cycles, or as the global or local intensity of technically premixed flames varies as a result of temporal or spatial equivalence ratio Φ fluctuations. Selecting the threshold manually would diminish the advantage of Otsu's method where no user input is required and would be tedious for large image series. Gradient-based approaches may suffer from the LoS nature of the images as well as from additional blurring effects such as misalignment, low signal intensities, and fiber crosstalk. Figure 5.2 presents the effect on the resulting flame object from selecting two neighboring thresholds for a total number of 12 classes. The flame object defined by the white boundary appears more compact than the flame object within the blue boundary, however, analyzing the gradient does not favor one of the two presented values.

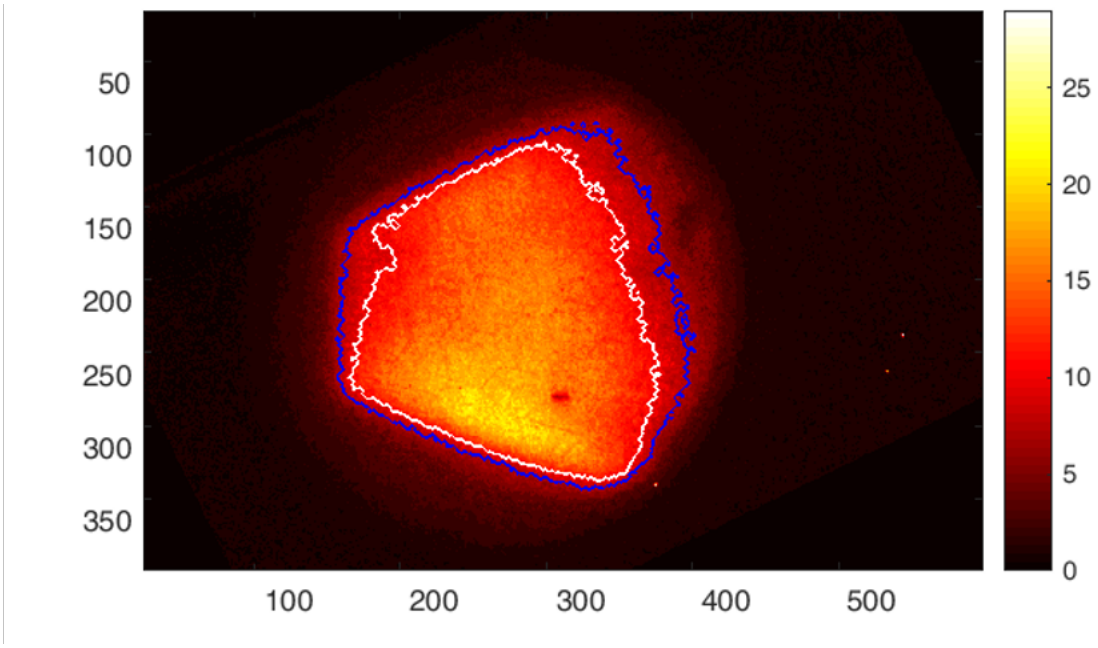

Figure 5.2: Effect of selecting neighboring thresholds k_i (blue) and $k_{\mathrm{i+1}}$ (white) for a given number of classes (here 12). The intensity scale of the chemiluminescence image is indicated by the colorbar.

In order to identify the flame as unambiguously as possible, an optimization method was developed. As a starting point, sets of thresholds were generated, using the Otsu method while increasing the number of classes C, starting from one and increasing to the maximum five. The result is a set of thresholds M_{k} for each $C_{\mathrm{i}} = \{1, 2 \dots, \mathrm{n}\}$, defined as

$$M_{\mathrm{k,n}}(C_{\mathrm{n}}) = \{k_1, k_2 \dots, k_{\mathrm{n}}\} \tag{5.4}$$

Now, each element in M_{k} represents a certain intensity threshold and the optimization routine regroups all sets, according to the representing intensity group i, into new sets containing all found thresholds of similar value

$$M_{\mathrm{i}}(i) = \left\{k_{\mathrm{C1,i}}, k_{\mathrm{C2,i}} \dots, k_{\mathrm{Cn,i}}\right\}. \tag{5.5}$$

Afterwards, a set of flame lengths was calculated for each M_{i}. Now, the standard deviation within each set $l_{\mathrm{f}}(M_{\mathrm{I}})$ was calculated, thus identifying the intensity group with the lowest error in the estimated lengths, i.e., the lowest standard deviation. In consequence, the possible values for the optimal threshold are narrowed down to a limited set of similar intensity values.

Despite the limited set, this reduction process did not lead to the most accurate identification of the flame object as no criterion for selecting the threshold which represents the outer flame contour is defined. In consequence, the determination process of the optimum threshold k_{i}^{+} was extended by an additional step, in which the image entropy was calculated for each resulting flame object.

Image segmentation based on or aided by image entropy is commonly used in applications with low contour clarity and low difference in intensity [113–116] and may improve the determination process of the optimum threshold k_{i}^{+}.

Entropy in information theory was first introduced by Shannon [117] and applied by Pun [118] for image post processing. The image entropy for a confined image region of $X \times Y$ pixels with $X = \{x_1, x_2 \dots, x_{\mathrm{I}}\}$ and $Y = \left\{y_1, y_2 \dots, y_{\mathrm{I}}\right\}$ is given by [119]

$$H = -\sum_{\mathrm{L}=0}^{\mathrm{L}=C-1} P_{\mathrm{L}} \log_2(P_{\mathrm{L}}) \tag{5.6}$$

with $P_{\mathrm{L}} = n_{\mathrm{L}}/X \times Y$ [120] as the probability of number of pixels at gray level L.

The boundary of the flame object, i.e., the presumable outer flame contour, is assumed as a transition region within the images. According to [121], such transition regions in images are characterized by high values of image entropy as given by 5.6. Subsequently, in order to determine the optimal threshold k_{i}^{+} to represent the flame object, the image entropy was calculated for each flame object within each set $l_{\mathrm{f}}(M_{\mathrm{i}})$. Finally, the threshold k selected as the optimal threshold k_{i}^{+} had to meet the constrains of representing the threshold with the lowest standard deviation and the maximum entropy at the transition region between the flame image and the background [112, 119, 122].

After finding the optimal threshold k_{i}^{+}, the images were binarized and the signal outside a continuous flame object was omitted. In the following step, line-wise scanning for the maximum spread of the flame object in horizontal direction was performed as the maximum spread in this direction was considered the flame length, i.e., the spread of the flame object in the direction perpendicular to the combustor exit plane. Therefore, the normalized flame length is given by

$$l_{\mathrm{f}} = \frac{x_{\max} - x_{\mathrm{B}}}{D_{\mathrm{B}}} \tag{5.7}$$

where $x_{\max}$ and x_{B} are the x-coordinates of the maximum object spread and the burner exit plane, respectively. D_{B} is the outer diameter of the burner. The process is shown in Figure 5.3

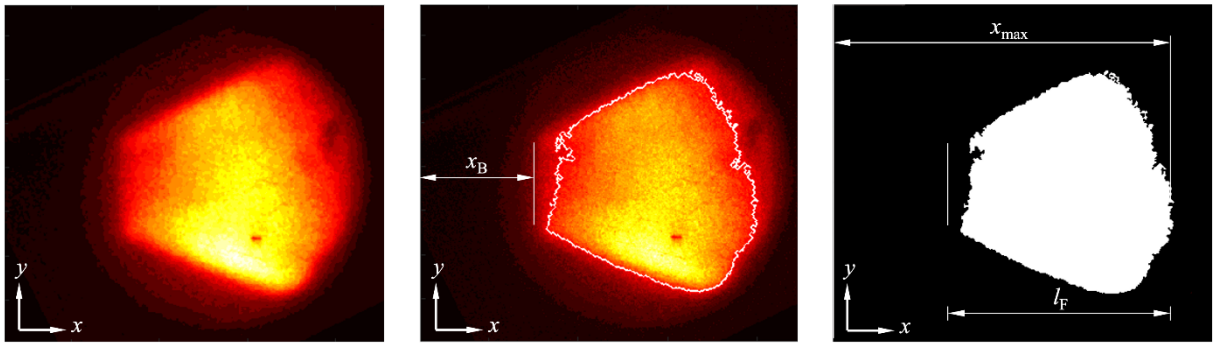

Figure 5.3: Overview of the determination process of the flame length: a series of chemiluminescence images of the flame object is used as input (left). The flame object is identified by the optimal threshold k_i^+ and the position of the burner is determined (middle). Afterwards, the images are binarized, the maximum spread of the flame object x_{max} is determined and the flame length is calculated (right).

For the CEC measurements, an additional image correction step prior to the evaluation of the flame length in post processing was required. For these measurements, geometrical structures inside the transition within the FOV of the input optics were used as targets. The target images $\boldsymbol{I}_{target}$ were recorded by a USB microscope with a spatial resolution of 640 × 480 pixels before the combustor was assembled and inserted into the test rig. In contrary, the chemiluminescence images were recorded with a scientific high-repetition rate camera with a resolution of 1024 × 1024 pixels (cf. section 5.2.3). In addition, the USB microscope was equipped with fixed imaging optics, so that the fiber bundle was used without the later output optics, hence the magnification of the target images differs from the magnification of the chemiluminescence images.

Thus, the images were resized, mapped, and rotated prior to the determination of the flame object to align the flame object inside the combustor. Since the end of the fiber bundle is contained in both the target image and the chemiluminescence images, this information was used to determine the required transformation matrices. First, the fiber bundle was detected in the respective images by searching for the circular structure of the fiber bundle using circular Hough transformation (CHT) [123–125]. The algorithm finds the radii and corresponding centers of the fiber bundle in the respective images. Afterwards, the transformation matrices for resizing the images were calculated and the images resized so that the imaged fiber bundle appears at the same size in both images, i.e., the calculated radii fulfill the constraint $r_{Fiber,CL} = r_{Fiber,target}$. Then, the centers of each detected fiber bundle were translated into the middle of the respective image. After detecting the outer contour of the flame object, as discussed

above, the contour was mapped onto the target image and rotated so as to match the orientation of the geometrical structures. The resulting angle of rotation was saved and afterwards applied to all chemiluminescence images prior to the determination of the resulting flame length.

5.2.2 NDP-1 Measurements

Subject of investigation was the main evolution stage of the well-established HR3 combustor. Its first version was developed in 1995 [5, 126], and the combustor, after continuous development, represents until today one of the most reliable combustion systems. It is, for example, used in the SGT5-4000H gas turbine. Originally it was designed as a so-called hybrid burner, featuring a lean premixed main stage for targeting the required NO_x-emission level as well as a diffusion pilot to maintain operational stability, i.e., in the sense of combustion instabilities, at part load conditions [126, 127].

Since its initial introduction, the combustor has been modified numerous times to address the increasing requirements for gas turbine combustors. The modifications may be summarized in three major evolution steps. In the first evolution step, the aerodynamic design of the burner was adapted to the changed outer recirculation zone inside the annular combustion chamber due to the decrease in cooling air after the introduction of the cooling-air reduced combustion chamber (CAR). The second evolution step addressed the pilot stage of the combustor as the diffusion stage was replaced by a premixed stage, thus further decreasing the NO_x emission of the combustor. In the third evolution step, the premixed stages were modified in order to further increase the turbine inlet temperature – thus increasing efficiency of the engine – and to increase the accepted Wobbe index range of the engine.

Nowadays, the power output of the SGT5-4000F engine is pushed to 329 MW with a pressure ratio of 20:1 and a gross efficiency of 41 % [128].

A cross section view of the combustor is shown in Figure 5.4. The combustor consists of two separate stages, which are arranged in a concentric manner, whereas the diagonal-oriented swirler of the main stage (Main swirler) surrounds the inner axial swirler of the pilot stage (Pilot swirler). As indicated, fuel and air are mixed within each stage as the air supplied by the compressor enters the corresponding stage and is mixed with the fuel, which is injected through nozzles located inside the swirler vanes (indicated as black arrows) in the main and pilot stage, respectively. Oil nozzles in the main and pilot stage allow for an operation with liquid fuels.

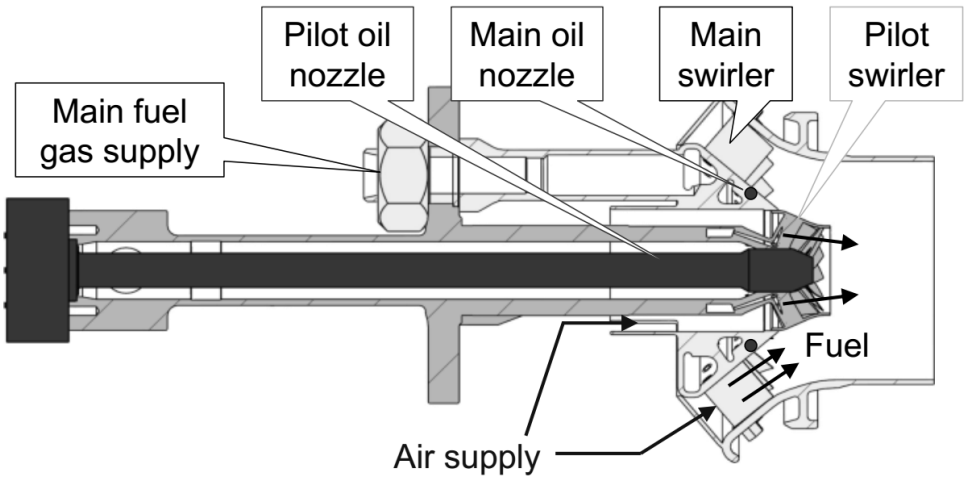

Figure 5.4: Cross-section of a HR3B burner for the SGT5-4000F engine [16].

The arrangement of the combustor stages and the swirl orientation results in a cone-like shaped flame anchored at or in the vicinity of the combustor exit plane [2, 5, 129, 130], featuring an outer and an inner reaction zone [15]. The total amount of fuel as well as the main and pilot split, the portion of fuel injected via the respective stage, is adjustable in order to address varying loads and flame stabilization.

Two test points were selected, derived from real engine conditions, and scaled to atmospheric pressure using natural gas as fuel. The first test point represented base load conditions, i.e., 100 % GT load with a normalized pilot split of 8 % and the second test point part load conditions, i.e. 50 % GT load, with a pilot split of 10 %.

Experimental Setup

For the measurements, the NDP head design was used and inserted into the fiber port closest to the burner (center of port 137 mm downstream of the burner exit plane) inside the cooled NDP-1 inset, which replaced the side window of the test rig (see section 4.4). Since the inset itself was cooled and the thermal load of the experiments comparably low, the probe was installed without additional cooling, i.e., without the cooling body.

A schematic overview of the detection setup is shown in Figure 5.5. The *Fujikura FIGR 30k* bundle (FB) was used in combination with the 40° FOV (L1–L4) input optics to detect the complete flame, as well as the burner exit. As output optics, the 10° FOV (L5) single lens was selected. In order to detect the OH^* chemiluminescence exclusively, a *Semrock* dielectric band-

pass filter (BP) with a center wavelength at 312 nm and a bandwidth of 35 nm in combination with a UG-11 filter glass was mounted in front of the recording system. The resulting transmission characteristics are shown in Figure 5.6.

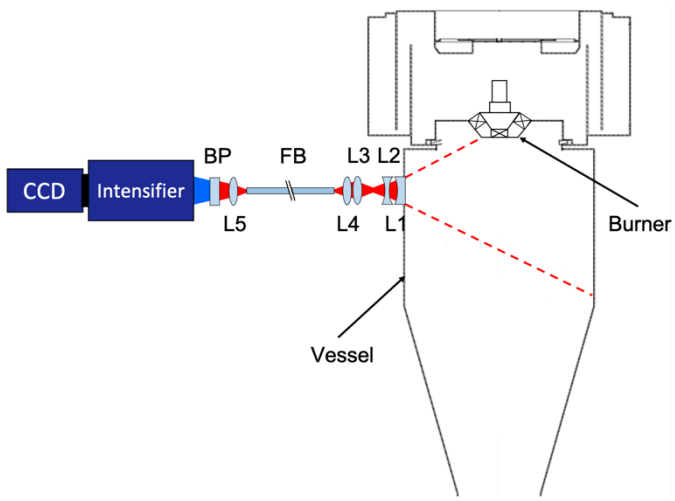

Figure 5.5: Experimental setup at the NDP-1.

The recording system consisted of a *PCO Sensicam QE* equipped with a *LaVision IRO* image intensifier. The flames were recorded at a repetition rate of 10 Hz with exposure times of 150 and 450 µs, respectively.

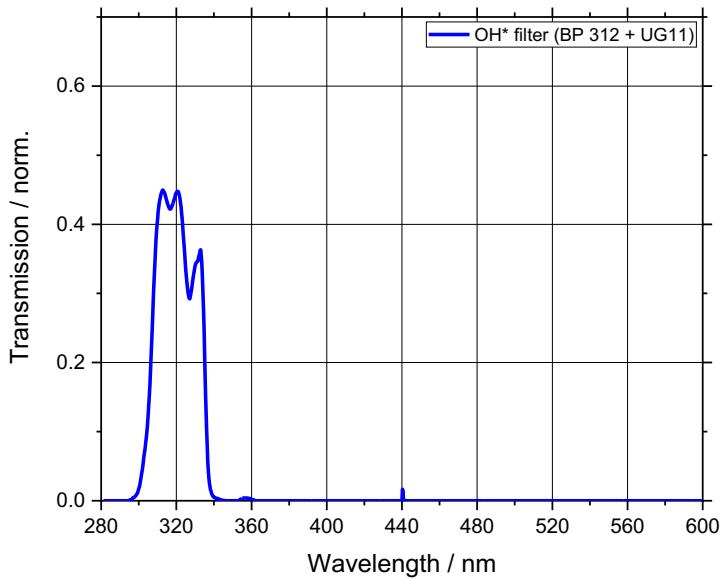

Figure 5.6: Transmission characteristics of the selected OH^* filter (BP 312) in combination with 3 mm UG-11 filter glass.

Results

For the base load test points, two image series out of 200 single shot images were recorded. The first series was recorded with an exposure time of 450 µs (series A) and the second series with a shorter exposure time of 150 µs (series B). The averaged chemiluminescence image for each series is shown in the top row of Figure 5.7.

For series A, the chemiluminescence emission is well-discriminated against the background emission and a continuous flame object was observed and completely located within the resulting FOV, as indicated by the white contour line in the top left corner in Figure 5.7. The flame object is anchored in the vicinity of the burner exit and shows the characteristic cone-like shape and a curved flame tip.

The averaged chemiluminescence image as well as the flame object for series B is shown in the top right corner in Figure 5.7. Although the lower exposure time of 150 µs in combination with a higher intensifier gain led to a decrease in SNR the flame object was reliably determined by the post processing routine.

Both the averaged chemiluminescence signal and the determined flame object of series B showed similar structures as in series A like the cone-like shape and the curved flame tip. Nonetheless, the determined flame object appears coarser, in particular at the flame tip, with small independent flame objects being detected.

Especially in the upper region of the flame tip, some agglomerated pixels seem to be excluded from the main flame object due to the set limitation of connectivity, i.e., the minimum number of connected pixels at a certain threshold, thus resulting in apparently independent flame objects. In addition, the average chemiluminescence image suffers from background noise due to the high intensifier gain as some portion of the intensity signal appears outside the illuminated region of the sensor, i.e., outside the imaged fiber bundle.

The calculated axial flame length distribution is shown in the bottom row of Figure 5.7 for series A on the left and for series B on the right, respectively. The flame length was calculated for each single shot image and the resulting classes of found length are shown as blue bars together with the resulting normal distribution indicated as the red curve within each graph.

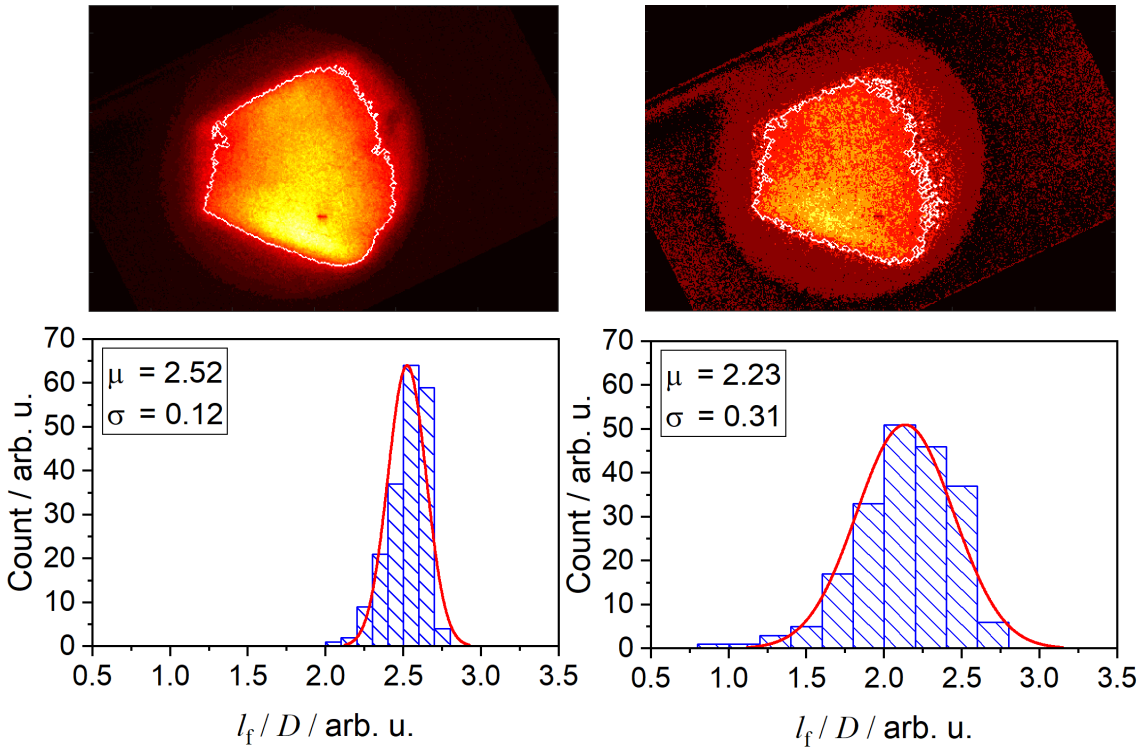

Figure 5.7: Top row: averaged chemiluminescence images for base load conditions recorded with exposure time of 450 µs (left) and 150 µs (right). Bottom row: corresponding distribution of the axial flame lengths.

In general, the distribution of series A appears narrower with a mean normalized length of $l_f/D = 2.52$ and a standard deviation of $\sigma^2 = 0.12$, whereas the axial flame length of series B was found to be shorter with a normalized length of $l_f/D = 2.23$ and a less uniform distribution with a higher deviation of $\sigma^2 = 0.31$.

The increase in standard deviation as well as the reduced length most probably originates from the lower exposure time. Firstly, the lower exposure time reduces the temporal averaging of the flame in each single shot. Hence, weaker flame areas, in particular at the tip of the flame, might be less well determined due to the low intensity. In addition, the lower exposure time generally lowers the SNR and thus complicates the discrimination of the flame object within the images. This is evident at the flame tip where the object appears coarse, and some objects are separated from the main flame object. Due to the aforementioned connectivity criterion, these areas are excluded from the flame length calculation after eroding the image to separate the outer contour of the flame object. Nonetheless, the reduced temporal averaging allows for capturing the variance of the flame length within the image series, resulting in a broader distribution, as seen in the above-presented graph.

For the second test point, i.e., the part load conditions, again 200 single shot images were recorded with an exposure time of 450 µs (series C). The results are shown on the right-hand side of Figure 5.8 together with the results for series A.

Again, the averaged chemiluminescence image is presented in the top row while the axial flame length is shown in the bottom row. As expected, the part load flame appears significantly shorter with a normalized length of $l_f/D = 1.06$. However, at the tip some flames areas might have been neglected due to the selected connectivity. The flame still stabilized in the vicinity of the burner exit and featured the characteristic cone-like shape. The increased standard deviation of $\sigma^2 = 0.23$ might indicate a less stable flame, which might originate from the comparable low pilot split of 10 %, yet during the experiments, no significant combustion instabilities (cf. section 5.3) were detected.

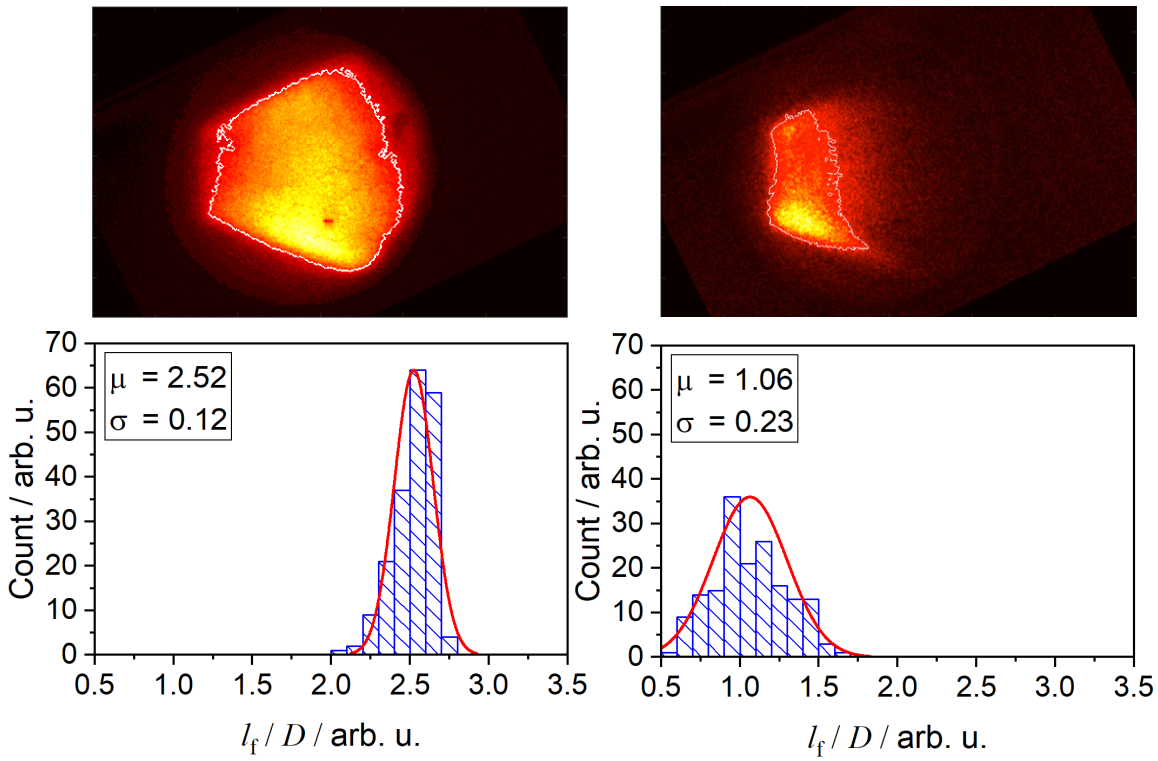

Figure 5.8: Top row: averaged chemiluminescence images for base load (left) and part load (right) operation. Bottom row: Corresponding axial flame length.

In summary, the optics used allowed for reasonable chemiluminescence imaging of a complete gas turbine combustor flame at the geometrically unscaled NDP-1 test rig. Viable images were recorded with exposure times down to 150 µs, serving as input for a reliable post processing routine for the determination of the axial flame length. The routine ran stable for all image

series without user interaction, although underestimating the length by an average of 12 %, compared to user-driven determination.

5.2.3 CEC-Rig Measurements

The second investigated hardware was an experimental design of the ULN (ultra-low NO_X) combustion system. The non-experimental ULN combustor represents the combustion system for the SGTx-8000H engine which features a gross efficiency of over 41 % with a pressure ratio of 21:1 and an electrical power output of 450 MW (50 Hz engine) in single cycle [131]. The combustor was first brought into service in a SGTx-8000H frame in 2007 and is continuously updated today [10, 11].

The system comprises eight main stage swirlers fixed at a support housing, a central pilot nozzle, a flow sleeve, and a basket. A sectional view of a respective combustor assembly is shown in Figure 5.9. The standard design of the combustor features five fuel stages whose supplied gas quantity can be adjusted independently from each other. The main stage is split into two stages A and B, respectively, with each stage encompassing four swirlers, arranged crosswise as indicated in the bottom right corner of Figure 5.9. The fuel is injected via internal fuel nozzles inside the swirler's guide vanes while instantly being mixed with air in the swirler.

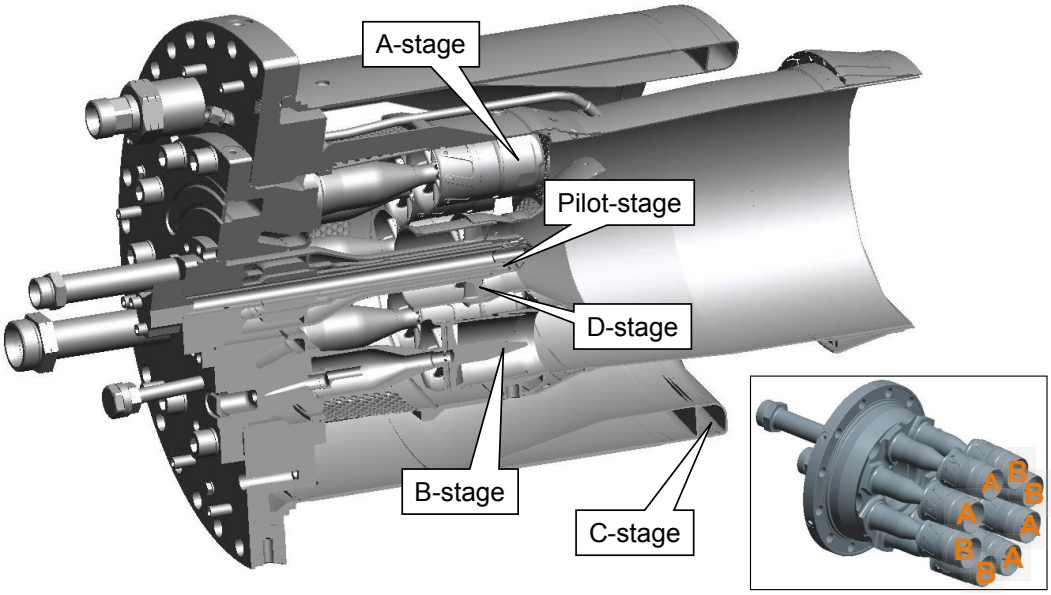

Figure 5.9: Sectional view of the ULN combustor of the SGTx-8000H engine [2].

Two more fuel stages are located in the central pilot nozzle with the diffusion pilot-stage at the tip as well as the premixed D-stage, whose swirl vanes, including the internal fuel nozzles, are encircling the pilot's central portion. In addition, the C-stage is located inside the flow sleeve and injects fuel into compressed air which is then guided through the main and pilot stages. The experimental design additionally features a fuel stage (hereinafter referred to as cross-stage) which injects fuel as jet-in-crossflow downstream of the main flame. This stage is not shown in Figure 5.9.

Experimental Setup

In this campaign, the latest design of the flexible fiber-based probe as well as latest design of the probe head, i.e., the CEC head, were used for the first time under high-pressure conditions. As presented in section 4.4.3, the optical access was located – 12° (counterclockwise in flow direction) off to the top dead center (TDC) and 32 mm downstream of the rear edge of the cross-stage injector holes in the transition, i.e., 70 mm downstream of the centerline of the stage, resulting in a sideview of the flame. The probe was incorporated into the cooling water circuit of the test rig and was supplied with a constant water mass flow of approximately 1.3 kg/s. To ensure the nitrogen cooling of the probe head and in particular the window optics and window portion, the N_2 line of the probe was connected to a separate N_2 supply line of the test facility, and the feeding pressure was kept at 0.5 MPa above combustion pressure, i.e., the pressure inside the test rig.

In order to fulfill the flexibility requirements of the selected feed-through approach (cf. section 4.4.3), the optical setup was based on the *Nanjing 20k* imaging fiber bundle, which offers a higher flexibility than the *Fujikura 30k* bundle. A principal sketch of the recording setup is shown in Figure 5.10. The 25° FOV design was used as input optics. At the proximal end of the bundle, i.e., at the fiber bundle end surface outside the combustor, the 10° output optics were used to project the image from the fiber bundle onto the detector of the image intensifier.

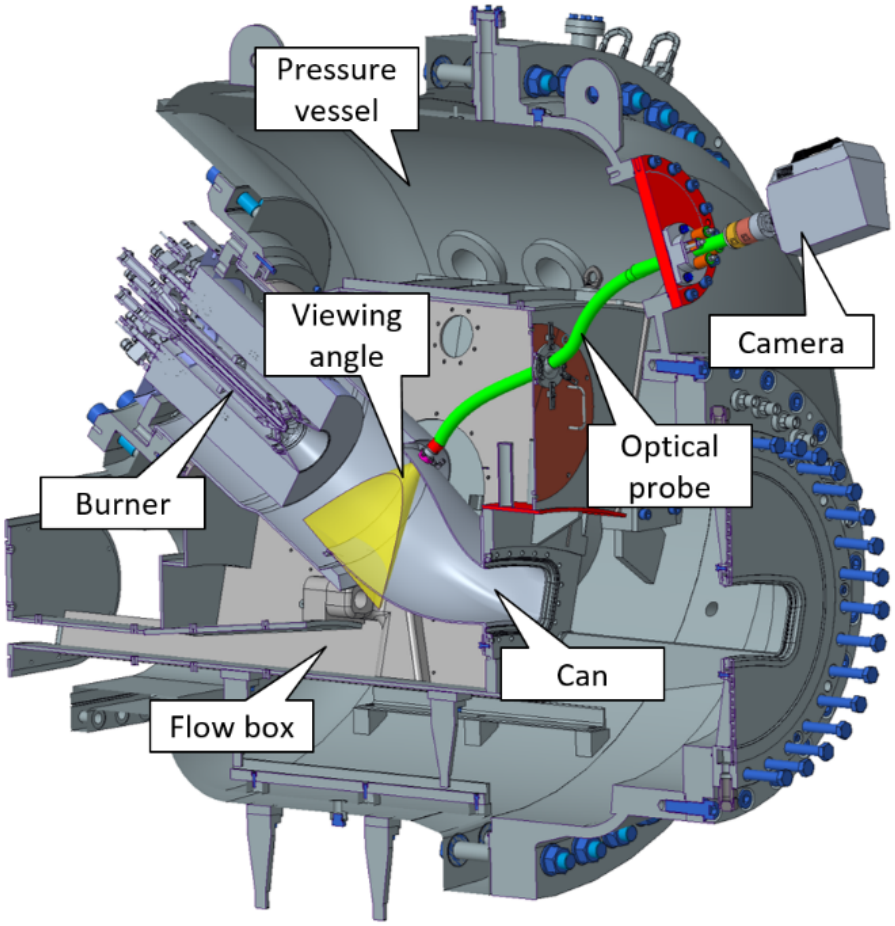

Figure 5.10:Scheme of optical setup for chemiluminescence imaging.

A narrow interference band-pass (BP) filter for CH^* ($\lambda = 434 \pm 8$ nm) was chosen to record the chemiluminescence signal originating from CH^* emission exclusively and placed in front of the detection systems. The transmission characteristics as well as the optical density of the selected filter are shown in Figure 5.11. The filter selection was based on the experiences from former measurements [15, 16] and in consideration of the limited testing time as only one testing day was available. Although OH^* might show higher emission and the dominant band heads are even further away from the black-body radiation from hot combustor parts, this filter avoids possible reabsorption of OH^* signal by ground-state OH in the exhaust gases [60, 54] at high pressure.

As detection system, the *Photron Fastcam SA-Z* high-speed camera was combined with the *LaVision high-speed IRO* image intensifier. The camera features a maximum resolution of 1024 × 1024 pixels at a maximum repetition rate of 20 kHz. Nonetheless, in order to record time series of sufficient duration as required for ignition testing of the cross stage due to limitation of the internal storage of the camera, the resolution was set to 896 × 1024 pixels at a

repetition rate of 2 kHz in order to record continuous single shot image series of 10,000 and 25,000 images. The exposure time was set to 500 µs as a tradeoff between an unintended averaging of the images and a sufficient SNR.

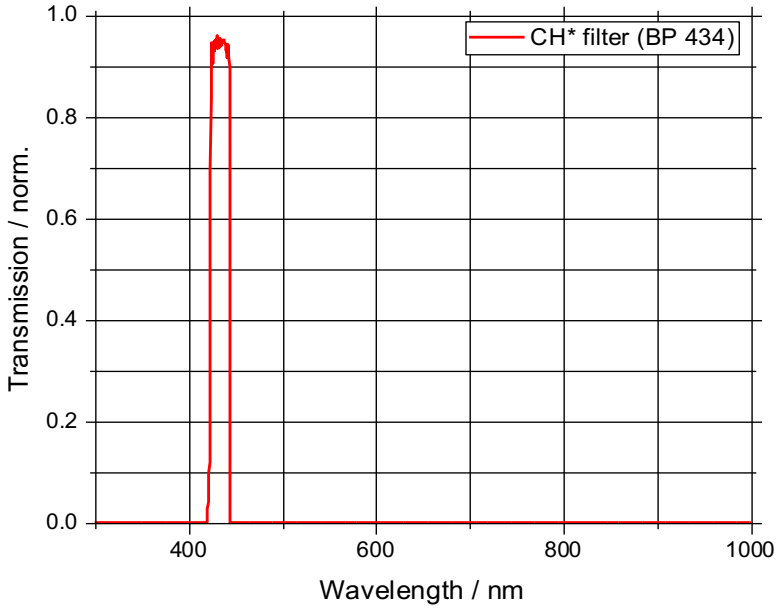

Figure 5.11: Transmission characteristics and optical density of the CH^* filter (BP 434).

An additional challenge for the chemiluminescence measurements at the CEC rig arose from the ambient conditions inside the test cell, more precisely from high noise emission (sound pressure), high vibrations and high room temperatures. At the CEC, the backpressure valve of the rig in combination with a large acoustic volume, i.e., the volume of the test cell, causes a high sound pressure. Measurements showed that the sound pressure levels inside the test cell may exceed 140 dB during operation. Such high levels have already led to failures of electronics, even of quite robust AC adapters. Moreover, the ambient temperature inside the test cell may exceed 330 K during testing.

Although the flexibility of the fiber bundle allows for placing the detection system, comprising the camera, the image intensifier and the respective controllers, next to the test rig without any mechanical connection, the length of the imaging fiber bundle is of only 3 m length, and thus, the detection system had to be placed close to the feed-through port (cf. section 4.4.3) of the rig and thus inside the test cell. Moreover, the feed-through port was located inside the inspection flange, and thus directly above the exhaust portion of the test rig.

To position the detection system close enough to the flange, the detection system was mounted onto a breadboard, which was placed on a bridge-like frame that extended over the exhaust portion of the rig. The frame was based on optical guide rails with adjustable feet. To avoid or at least to reduce the feeding of vibration from the test cell into the frame and subsequently into the sensitive detection system, the frame was placed on sand filled buckets. Additionally, the breadboard was connected to the frame by rubber shock absorbers.

In order to protect the detection system from the noise emissions, the setup, i.e., the equipment mounted onto the breadboard, was encapsulated by a soundproofing box. The box comprises five wooden elements made of oriented strand board (OSB), each element was equipped with acoustic foam elements with thicknesses of 50 and 80 mm. The acoustic elements were arranged in such a manner that the outer surface of a wooden element, i.e., the surface of the box, was equipped with the thicker elements while the inner surfaces were equipped with the thinner elements. The setup is shown in Figure 5.12. In this way, the damping characteristics of the foam elements superimposes, leading to an effective soundproofing.

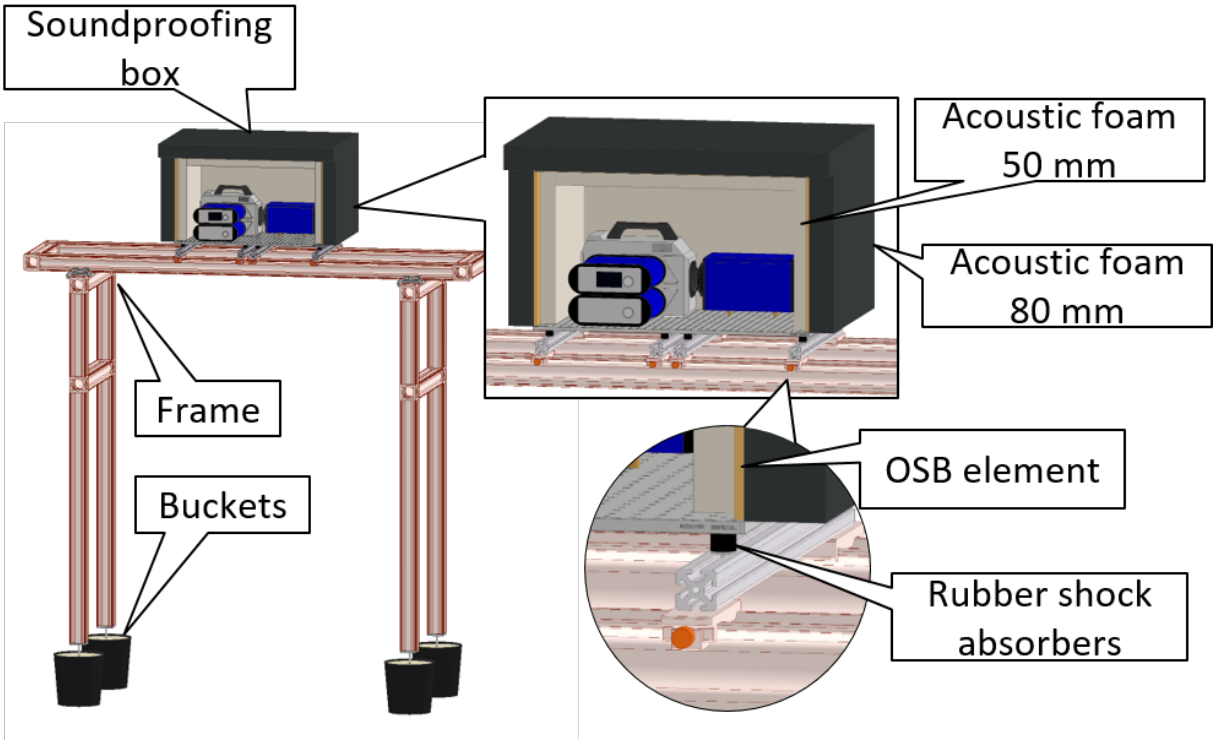

Figure 5.12: Setup at the CEC rig. The detection system is placed on a breadboard and encapsulated by the soundproofing box (top right), while the breadboard is connected to the frame via rubber shock absorbers (bottom left).

During operations, the soundproofing box was flushed with a constant flow of nitrogen, which was supplied through the breadboard so as to keep the temperature inside the box within the operation temperature of the detection system.

Results

For the CEC measurements, the aim was to investigate the interaction of the flame between the cross-stage (hereinafter referred to as cross flame) and main flame, i.e., the flame of the main and pilot stage only, and in particular to detect the resulting location of the cross-flame portion. Consequently, an image series containing operations of the main flame only, the ignition of the cross flame, and the combined flame was recorded. A stable base load operation point at a pressure of 0.8 MPa was selected as test point and 25 000 single shot images at a repetition rate of 2 kHz with an exposure time of 500 µs were recorded. The resulting trace of the averaged chemiluminescence intensity is presented in Figure 5.13.

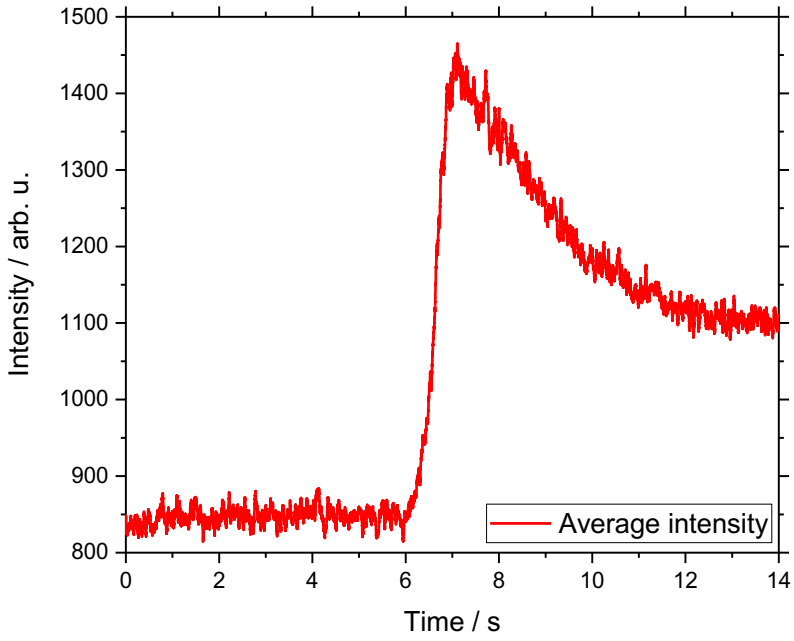

Figure 5.13: Averaged integrated intensity during the ignition of the cross stage.

As it can be seen from the figure, in the beginning of the recording, the main flame was burning separately. After approximately 6 s, the cross flame ignited. It has to be mentioned that the ignition of the cross flame was delayed due to the time lag caused by the length of the gas

supply line from the valve to the cross-stage injectors. As expected, the averaged chemiluminescence intensity increased significantly during the ignition process and reached its maximum value, which was about 1.7 times higher than the initial intensity shortly after ignition. As the resulting flame, i.e., the main flame and the cross flame combined, stabilized, the averaged chemiluminescence intensity declined to a stable value of approximately 1.25 times of its initial value.

In order to identify the contribution of the cross flame and its position in the resulting flame, two averaged chemiluminescence images were calculated. The first image only contained single shots recorded prior to the ignition of the cross flame, i.e., single shots of the main flame, while the second averaged chemiluminescence image contained single shots recorded after the stabilization of the resulting flame. In consequence, the ignition process of the cross flame was excluded from the image. Afterwards, the first image was subtracted from the second image to achieve an averaged chemiluminescence image of the isolated cross flame. The images are presented in Figure 5.14.

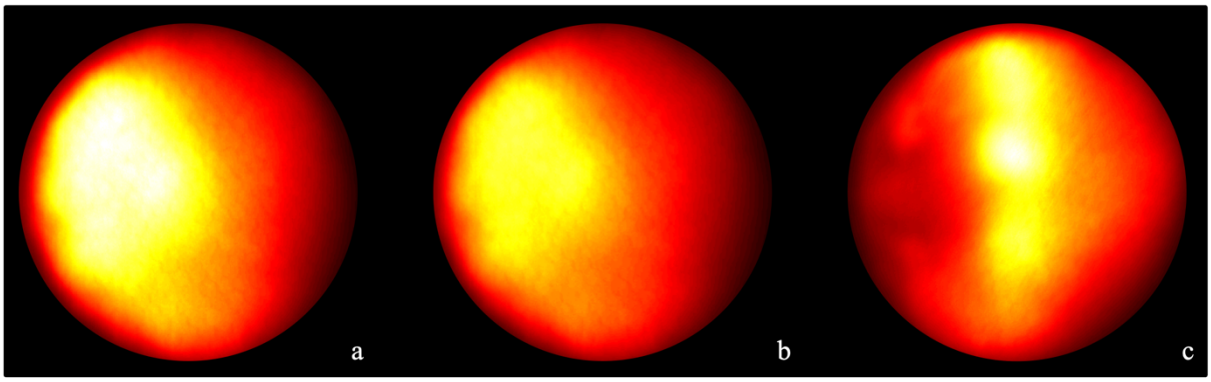

Figure 5.14: Average image of the flame after ignition of the cross flame (a), average image of the main flame prior to ignition of the cross flame (b), and the resulting average image of the cross flame (c). The color scale is adjusted to the respective maximum intensity of each image.

In the figure above, the color scale of image a and b are identical while the scale for image c is adjusted to its respective maximum (approximately 40 % of the maximum of a and b). The resulting image is presented in Figure 5.15. Although affected by the LoS integration, three – to some extent separated – regions of high intensity (outer contour marked in black) were observable. This number is consistent with the number of injectors visible in the pre-recorded target image.

To determine the effect of the main flow on the cross flame, the images were first transformed as described in section 5.2.1. Then the axial position of the cross flame was determined by

comparing the location of the center of the high intensity areas in the resulting image to the location of the center line of the injectors of the cross-stage in the pre-recorded target image. The result of the comparison is shown in Figure 5.15. After superimposing the contour of the averaged chemiluminescence image onto the target image, it was found that the axial positions were identical as the axial position of the regions of high intensity, i.e., 80 % of the maximum intensity (indicated by black contour), does not vary from the axial position of the center of the injectors (indicated by crosses). This may lead to the conclusion that the cross flame is not significantly affected by the main flow as it is not bended in downstream direction, and hence, stabilizes in the vicinity of the cross-stage injectors. It must be mentioned that the localization accuracy is constrained by the LoS integration in the chemiluminescence image.

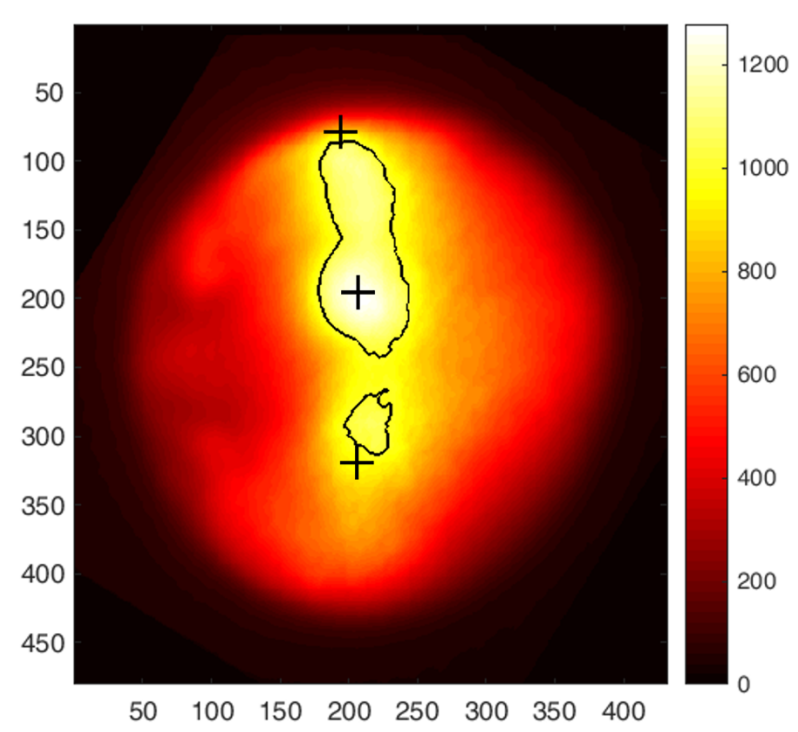

Figure 5.15: Averaged chemiluminescence image of the isolated cross flame at 0.8 MPa. The center of each injector located within the FOV is indicated by a cross. The intensity scale of the chemiluminescence image is indicated by the colorbar.

For the purpose of using chemiluminescence images as validation data for CFD simulations, CFD simulations were performed for the measured test point by Siemens AG. The spatial distribution of heat release was integrated along the LoS of the endoscope using a ray tracing approach in post processing of the CFD simulations. As the emission of CH^* was recorded, the chemiluminescence intensity qualitatively reflects the heat release rate. As can be seen in Figure

5.16, the position and structure correspond well between measurement and simulation, indicating a good quality of the CFD simulation for predicting the flame position. Nonetheless, improved simulations of the optical setup and effects are necessary to further improve the matching of the images.

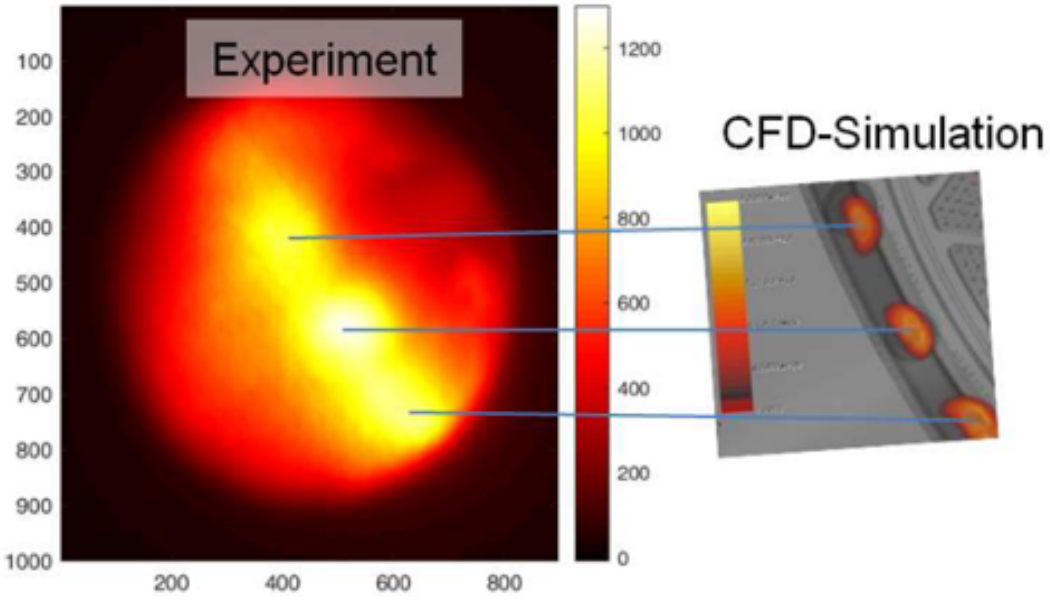

Figure 5.16: Comparison of the averaged chemiluminescence image obtained in the experiment (left) and the integrated heat-release rate from CFD simulations. The intensity scale of the chemiluminescence image is indicated by the colorbar.

The next set of test points represents different operation conditions, for which the axial fuel split, resulting in a change in the turbine inlet temperature (TIT), and the combustion pressure were varied. The scope of the experiments was to investigate the impact of these two parameters on the flame length. It has to be mentioned, that some of the images were affected by an unexpected phenomenon as they showed an arc-shaped dark structure in the images. An example is shown for a test point at 1.2 MPa in Figure 5.17.

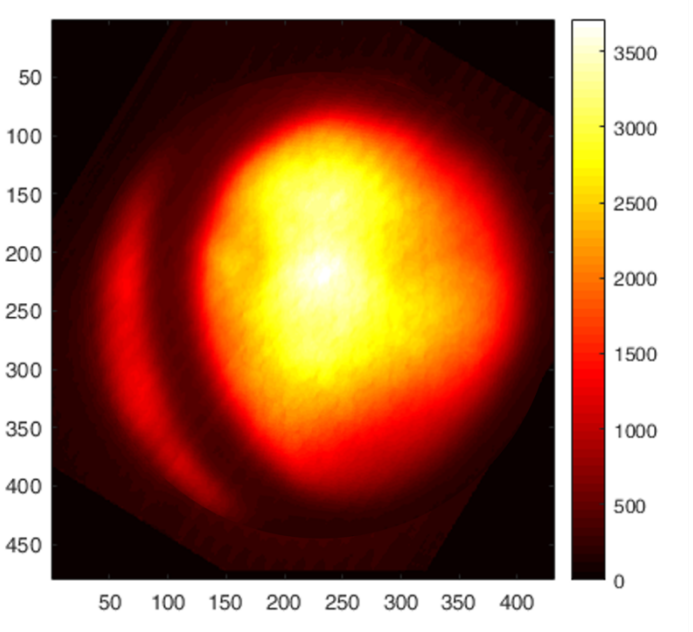

Figure 5.17: Test point at 1.2 MPa with arc-shaped blocking. The intensity scale of the chemiluminescence image is indicated by the colorbar.

This structure or blocking might be caused by either the front seal being displaced during the experiment or by cooling water entering the space between the input optics and the fiber bundle. For the later explanation speaks that behind the structure, in the picture on the left side, a lower intensity was measured and so a bubble formed by the entered cooling water was effective as optical element. However, no humidity was found in this area during the inspection of the probe carried out after the measurements. Consequently, the following results might be corrupted by an additional optical distortion. As the routine calculates the flame length using the maximum object spread $x_{\max}$ (see Equation 5.7), the arc-shaped blocking within the flame object is neglected.

Figure 5.18 depicts a set of variations for a normalized TIT of 0.96 and 1 and pressures of 0.8 and 1.2 MPa. In blue, the distributions of the detected flame lengths are shown, together with a Gaussian-fitted normal distribution. The length is normalized to the outer diameter of the pilot cone in the pilot cone exit plane.

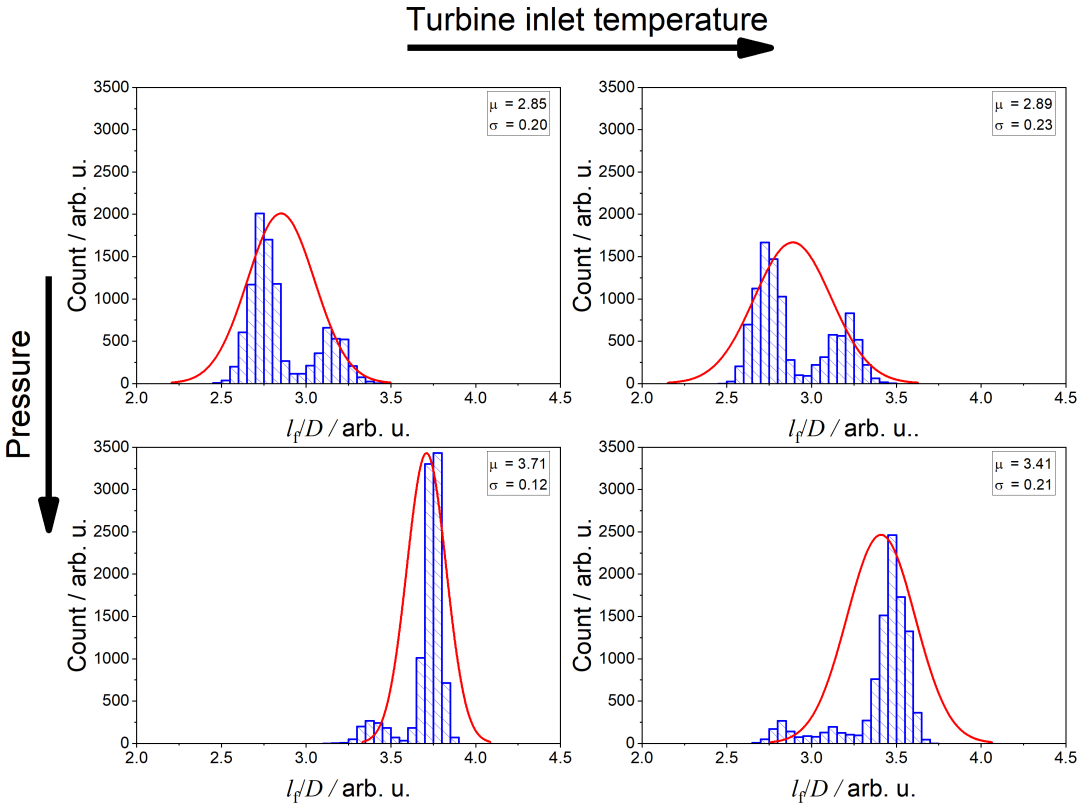

Figure 5.18: Flame length distribution for varying turbine inlet temperature and combustion pressure.

The 0.8 MPa flames in the top row appeared to be shorter with a wider spread and a tendency towards a bimodal distribution was observable, while the flames at 1.2 MPa, shown in the lower row, were found to be longer with narrower skewed left distributions. The impact of pressure variation was found to be more significant as an increase in pressure led to an increase in flame length of 30 and 17 %, respectively. On the other hand, the increase in TIT resulted in a non-consistent change in flame length as the flame grew by 1.4 % for the 0.8 MPa test point and shortened for the 1.2 MPa points. The overall behavior is most likely caused by aerodynamic effects rather than chemical effects during the combustion, as the flow velocity and turbulence increase with pressure.

It should be noted that the burner exit plane is not included in the images due to the limited FOV of the input optics in combination with the position of the probe head inside the transition. Consequently, any change in the overall position of the flame object, e.g., due to a possible change in the lift of position of the flame, are not accounted for in the calculation of the flame length.

In addition, the recorded chemiluminescence signal may comprise, besides the radiation of the selected CH^*, a non-negligible portion of background emission from molecules such as CO_2^* and CH_2O^* [50, 57, 132, 133].

After calculating the flame length, the results were investigated for possible correlations of flame length or its standard variation to other measurement data such as CO or NO_x emissions (measured by suction probes in the exhaust path) and to the general stability of the combustion in terms of thermoacoustic behavior (expressed as the amplitude of the pressure oscillation recorded by pressure transducers). Neither the flame length nor the standard variation showed an unambiguous correlation to any of the aforementioned data, as shown in Figure 5.19.

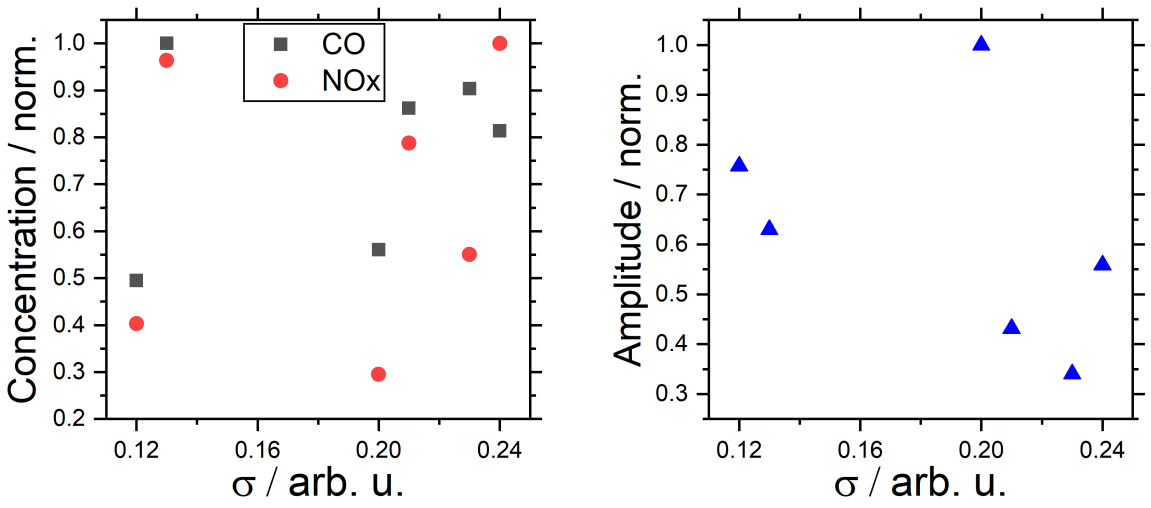

Figure 5.19: Correlation of the temporal standard deviation of the flame length to the normalized concentration of CO or NO_x in the exhaust gas (left) and pressure oscillation (right).

In summary, the presented measurements revealed a good determination of the flame within the recorded images. In particular, the experiments showed for the first time the location of the axial stage flame. It was found that this flame, in contrary to the expected behavior, seems to be centered close to the injectors without being displaced and pushed downstream. Furthermore, a significant impact of pressure on the flame length was recognizable. Correlating the flame length or its standard deviation to emissions or thermo-acoustic oscillations did not led to any satisfying results. Nonetheless, the ability to visualize the flame in such challenging environments may beneficially contribute to the overall development process.

5.2.4 Conclusions

In the above section, flame length and position measurements for real scale GT combustors were presented at atmospheric and at elevated pressures. An intensity thresholding-based calculation routine was established and applied to recorded chemiluminescence images of unscaled GT combustors. The method was found to be reliable. Even for poor SNR, the method was capable of reliably detecting the flame object and to calculate the flame length, although with higher uncertainties.

For the CEC measurements, the flame of the cross-stage was visualized for the first time by subtracting averaged chemiluminescence images of the main flame from images containing both the main flame and the cross flame. It was found that the cross flame appeared to be negligible affected by the main flame or main flow as the flames appeared in the vicinity of the injector nozzles in axial direction. In addition, three more or less separate flames were visible, which also corresponds to the number of injector nozzles located in the FOV, agreeing well with the results from CFD simulations. For testing the detection scheme of the flame object, the flame length for different combustion pressures and different axial fuel split (resulting in varying TIT) was determined. It was found that the size of the flame object and thus the flame length increases with pressure. However, no unambiguous trend was found for the TIT. In addition, no clear correlation was found between flame length or its standard deviation and CO or NO_x emissions or combustion stability.

5.3 Combustion-Induced Oscillations

The need to increase efficiency and reduce pollutant emissions led to highly premixed and lean combustion systems in gas turbine combustors with high power densities of 500 MW/m³ [2, 5]. Although these combustion systems are characterized by their high efficiency as well as low pollutant emissions, they are prone to combustion instabilities known as thermoacoustics or combustion-induced oscillations that affect the operation of the engine, such as flame blow-off, increased wear, structural damage or engine trips and feature reduced damping capacities due to their compactness [3]. Hence, the stability of the combustion process of a particular combustor design has to be considered during the development process of combustors [3, 5–9] and during operations of the engine [10, 11].

As discussed in section 2.3, a fundamental driving mechanism for these thermoacoustic oscillations is the coupling between the heat release rate fluctuation and the pressure fluctuation inside the combustion system. Under certain conditions, the heat release rate can be described by the emission intensity of specific chemiluminescence species [134–137], which allows for a comparatively robust and simple optical detection of the heat release rate or its fluctuation. The information obtained can be related to the pressure oscillations recorded by pressure transducers regularly used in or on the test rig [70, 71, 73, 138, 139] to further investigate the cause of these oscillations or to derive the flame transfer function [72, 140, 141].

As the general validity of chemiluminescence emission as a marker for heat release rate is often challenged in technical premixed flames [51, 63, 137, 142–146], care must be taken while evaluating the data. In some studies, the use of the ratio of chemiluminescence species was suggested to reduce the effects of the aforementioned flame properties while using chemiluminescence emission as a marker [132, 134], while other studies rely on a combined approach of measuring and modelling chemiluminescence species [58, 147] or on adapting the correlation of chemiluminescence emission and heat release rate to the case studied [148–150]. During the high-pressure testing in the development process of GT combustors, tedious adaption or multi-species measurements are not feasible or at least not reasonable. In consequence, a simpler approach is required to avoid misinterpretation of the collected chemiluminescence data.

In this work, a post-processing routine was developed to evaluate the potential use of the developed fiber-based probe for imaging chemiluminescence measurements to investigate the spatial origin of combustion-induced oscillations in a particular burner design in non-scaled GT burners, considering the limitations of its application in the challenging test-bed environments

in terms of accessibility, supporting measurements of other combustion variables, and repeatability. Three different burner settings were used for this purpose. The first was an SGTx-8000H combustor in the HBK-4 with limited optical access and realistic boundary conditions, while the second and third combustors, representing different SGT5-4000F combustors, were studied in the atmospheric NDP-1 vessel.

5.3.1 Post Processing

Recorded images of chemiluminescence emission might be used to indicate areas of heat release fluctuations or flame oscillations, which then could be investigated further to identify their origin. The developed routine is based on the assumption that the emission intensity of one of the prominent chemiluminescence species may serve as a suitable marker for the heat release rate or may at least represent flame oscillations during thermoacoustic events if the emission, more precisely its fluctuation, is related to the resulting pressure fluctuations. The latter is crucial as the detected fluctuations of the chemiluminescence emission might originate from other properties such as local equivalence ratio, local turbulence intensity, strain rate, flame stretch, etc. [31, 63, 151]. In particular, variations in the local equivalence ratio are critical as the temporal perturbations within the equivalence ratio are an important mechanism for thermoacoustic oscillations [28] and strongly affect the correlation between the chemiluminescence intensity and the heat release rate [31]. To prevent misinterpretation of the recorded chemiluminescence signal, it must be assigned as clearly as possible to the combustion instabilities. For this purpose, a signal-analytical approach in form of the so-called coherence analysis was chosen, which allows a prediction as to whether the recorded optical signal, i.e., the chemiluminescence emissions, is related to the combustion instabilities represented by the recorded pressure fluctuations. Assuming that the coherence between the chemiluminescence signal and the pressure signal represents the causality between these signals [152, 153], the level of coherence (possible values lie in the interval of 0 to 1) indicates whether the recorded intensity fluctuations are caused by the combustion instabilities and allow for the indication of areas within the combustor that exhibit significant intensity variations due to the combustion instabilities and could be the subject of further investigation during the combustor development process.

Starting point for the routine is a simultaneous recording of the pressure, the chemiluminescence intensity (as a series of single shot images) and the trigger signal during a combustion instability as shown in Figure 5.20.

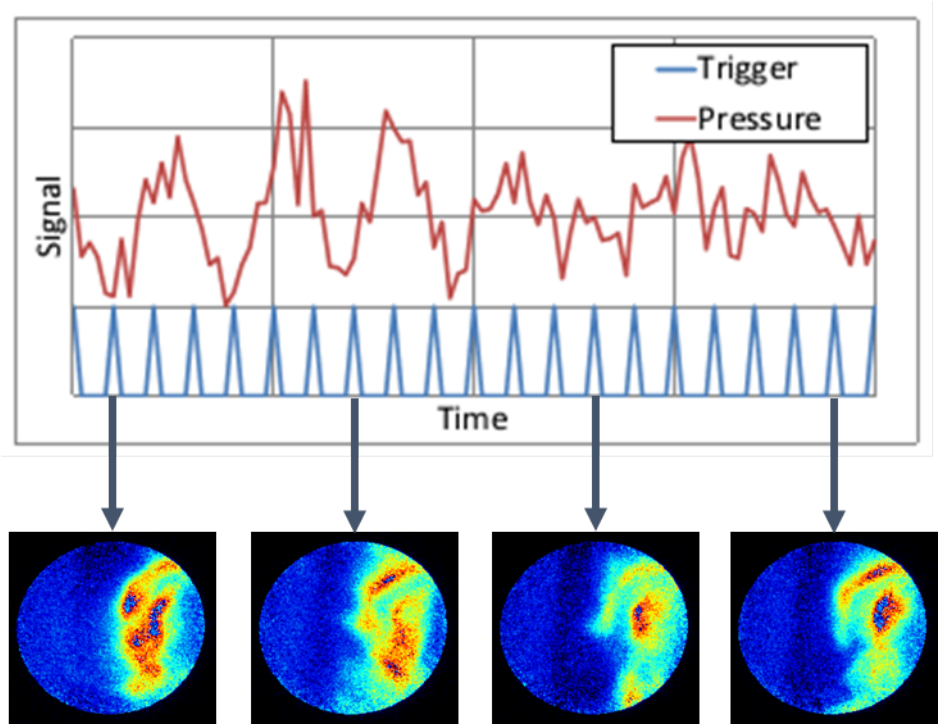

Figure 5.20: Simultaneous recording of pressure (red) and trigger signal (blue) with examples of chemiluminescence single-shot images recorded at the indicated trigger [16].

In consequence, the time of recording for each single shot image $\boldsymbol{Im}(r)$ with $1 \leq r \leq s$ of an image series of s images with regard to the pressure signal is known and thus the progression of the chemiluminescence intensity $I_{Cl}(t)$ and of the pressure $p(t)$ over the recorded period of time.

After background correction, a mask is automatically defined and applied to the images to suppress signal components outside the illuminated area of the detector, such as noise and artifacts caused by the detector. Afterwards, the chemiluminescence and pressure signal are Fourier-transformed from the time domain into the frequency domain by

$$I_{Cl}(f) = \mathcal{F}\{I_{Cl}(t)\} = \int_{-\infty}^{\infty} I_{Cl}(t) e^{-2\pi i f t} dt \qquad 5.8$$

and

$$P(f) = \mathcal{F}\{p(t)\} = \int_{-\infty}^{\infty} p(t)\mathrm{e}^{-2\pi \mathrm{i} f t}\,dt \tag{5.9}$$

to identify the frequencies of interest, defined as the frequency corresponding to the maximum amplitude of the respective signal, $f_{0,\mathrm{Cl}}$ and $f_{0,\mathrm{p}}$ and to evaluate the difference in frequency $\Delta f_0 = \left|f_{0,\mathrm{Cl}} - f_{0,\mathrm{p}}\right|$.

If the difference in frequency does not exceed a predefined threshold, the $m \times n$-pixel image matrix

$$\boldsymbol{Im}(r) = \begin{bmatrix} i_{11}(r) & \cdots & i_{1\mathrm{n}}(r) \\ \vdots & \ddots & \vdots \\ i_{\mathrm{m1}}(r) & \cdots & i_{\mathrm{mn}}(r) \end{bmatrix}$$

is split into b squared-shaped submatrices of adjustable size w × w

$$\boldsymbol{A}_{\mathrm{k,l}}(r) = \begin{bmatrix} i_{\mathrm{ij}}(r) & \cdots & i_{\mathrm{ij+w}}(r) \\ \vdots & \ddots & \vdots \\ i_{\mathrm{i+wj}}(r) & \cdots & i_{\mathrm{i+wj+w}}(r) \end{bmatrix}$$

with the number of submatrices

$$b = \left\lfloor \frac{m}{w} \right\rfloor \times \left\lfloor \frac{n}{w} \right\rfloor,$$

the indices of each submatrix

$$k = 1, 2, \ldots, \left\lfloor \frac{m}{w} \right\rfloor \text{ and } l = 1, 2, \ldots, \left\lfloor \frac{n}{w} \right\rfloor,$$

the number of rows $i_{\mathrm{k}} \leq i \leq i_{\mathrm{k}} + w$, and the number of columns $j_{\mathrm{l}} \leq j \leq j_{\mathrm{l}} + w$, whereas the first or starting index for each row and each column is defined as

$$i_{\mathrm{k}} = \frac{w}{4}, w + \frac{w}{4}, \ldots, \left(\left\lfloor \frac{m}{w} \right\rfloor - 1\right) w + \frac{w}{4},$$

and

$$j_\mathrm{l} = \frac{w}{4}, w + \frac{w}{4}, \dots, \left(\left\lfloor\frac{n}{w}\right\rfloor - 1\right) w + \frac{w}{4},$$

respectively. Then, the spatial-averaged intensity, given by equation 5.10

$$\bar{I}_{\mathrm{A_{k,l}}}(r) = \frac{1}{w^2} \sum_{\mathrm{i=i_k}}^{\mathrm{w}} \sum_{\mathrm{j=j_l}}^{\mathrm{w}} \mathrm{i_{ij}}(r) \tag{5.10}$$

is calculated for each submatrix for each image of the image series, thus giving the progression of the local chemiluminescence intensity $I_{\mathrm{Cl,A}}(t)$ for each submatrix. In order to allow for later spatial reconstruction, each submatrix is assigned a row index

$$x_\mathrm{local} = i_\mathrm{k} + w$$

and a column index

$$y_\mathrm{local} = j_\mathrm{l} + w$$

respectively.

In the next step, the routine determines the correlation between the pressure signal and the spatial chemiluminescence intensity by calculating the squared-magnitude coherence $\gamma^2_{I_{Cl},p}$ as defined in equation 5.11, as a measure of the correlation between the two signals [152, 153]

$$\gamma^2_{I_{Cl},p}(f) = \frac{\left|S_{I_{Cl},p}(f)\right|^2}{S_{I_{Cl}I_{Cl}}(f) S_{pp}(f)}. \tag{5.11}$$

In equation 5.11 the numerator is the cross-spectral density of the chemiluminescence intensity and the pressure signal, given by the Fourier-transformed

$$S_{I_{Cl},p} = \int_{-\infty}^{\infty} R_{I_{Cl},p}(t)\mathrm{e}^{-2\pi \mathrm{i} f t}dt \tag{5.12}$$

of the cross-correlation $R_{I_{Cl},p}(t)$ of both signals [153]. The denominator of equation 5.11 is given by the product of the autospectral density of the chemiluminescence intensity

$$S_{I_{Cl},I_{Cl}} = \int_{-\infty}^{\infty} R_{I_{Cl},I_{Cl}}(t)\mathrm{e}^{-2\pi \mathrm{i} f t}dt \tag{5.13}$$

and the autospectral density of the pressure

$$S_{p,p} = \int_{-\infty}^{\infty} R_{p,p}(t)\mathrm{e}^{-2\pi \mathrm{i} f t}dt \tag{5.14}$$

as the Fourier-transformed of the autocorrelation function of the chemiluminescence intensity $R_{I_{Cl},I_{Cl}}$ and of the pressure $R_{p,p}$ respectively [153]. The above specified properties are estimated using Welch's method [154, 155]. Under the premise, that a coherence value of $\gamma^2_{I_{Cl},p} > \gamma^2_{I_{Cl},p,\min}$ represents a good correlation of the detected pressure fluctuation and the chemiluminescence intensity fluctuation, the areas fulfilling this criterion are indicated by a white rectangle of size $w \times w$, centered at $P = (x_{\mathrm{local}}, y_{\mathrm{local}})$ to mark the possible spatial origin of the oscillations. The described post processing routine is visualized in Figure 5.21.

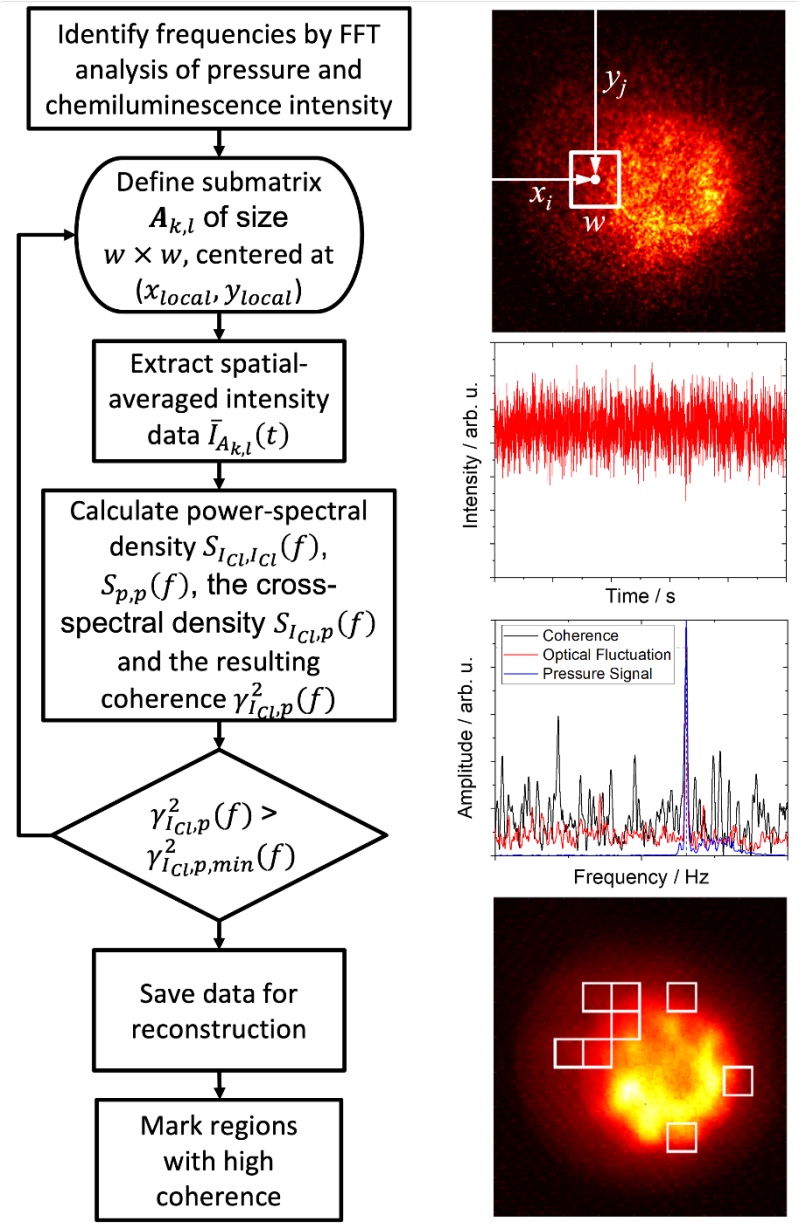

Figure 5.21: Post-processing routine for flame oscillation sensing

5.3.2 HBK-4 Measurements

The investigated hardware was a close-to-field engine design of the ULN combustor for the SGTx-8000H engine, featuring the two main stages A and B, diffusion pilot-stage, the premixed D-stage as well as the C-stage as described in section 5.2.3. For this design, high-frequency dynamics (HFD) which are characterized by frequencies above 1000 Hz [16, 156] were expected.

Experimental Setup

The imaging chemiluminescence measurements of the SGT5-8000H combustor were conducted with an existing rigid endoscopic probe. The probe was designed to withstand the harsh conditions inside the combustor and comprises an outer cooling body, an exchangeable probe tip and an inner fiberscope with the respective optics. The outer diameter of the cooling body is approximately 35 mm. Water and nitrogen cooling together with thermal barrier coating (TBC) at the probe tip allow for intruding the probe into the hot exhaust gas path of the combustor. The exchangeable probe tip is provided with a sapphire window featuring a nitrogen cooling stream to flush the sapphire window, which prevents contamination with combustion residuals. An imaging fiberscope with an outer diameter of approximately 8 mm and a length of 1600 mm was inserted into the cooling body. The rigid UV fiber bundle contains 50,000 singles fibers and was equipped with a custom-made input and output optics designed by *Micro-Epsilon Messtechnik GmbH & Co. KG*. The selected input optics consisted out of a front mirror and an air-spaced doublet, allowing for a viewing direction upstream towards the burner exit. An adjustable air-spaced doublet served as output optics. The probe was located in front of the guide-vane simulation section approximately 1350 mm away from the burner exit plane (see Figure 5.22) with an intrusion depth of the probe tip of about 110 mm.

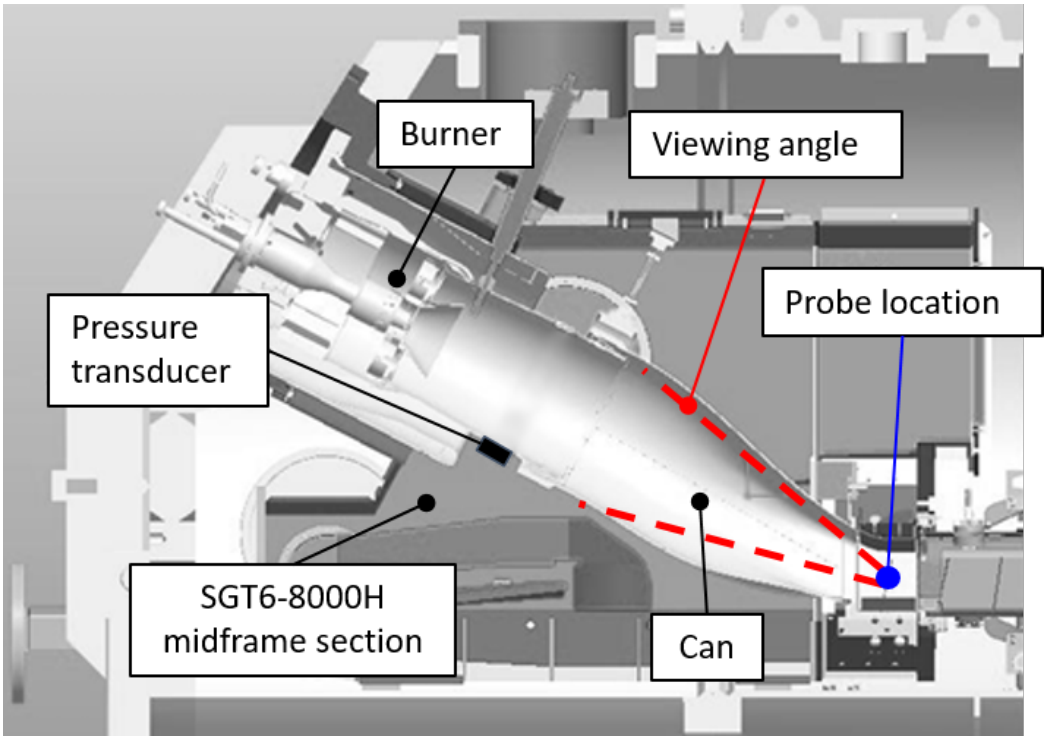

Figure 5.22: Experimental setup at the HBK-4 with the SGT6-8000H frame.

To discriminate the OH^* chemiluminescence emission from the overall emission inside the combustor, a *Semrock* band-pass filter (312 ± 17.5 nm) was combined with a 3 mm thick UG 11 colored glass (*Schott*), which was set up in front of the detection system. This combination was found to block the background radiation, e.g. from thermally excited water and hot combustor walls, effectively while remaining reasonable transmission in the desired spectral range. It is the same combination that was used during the flame length measurements at the NDP-1 (see section 5.2.2). The resulting transmission of the combination is shown in Figure 5.23.

As detection system, a *Phantom V7.3 CMOS* high-repetition-rate camera combined with a *LaVision high-speed IRO* image intensifier was used. The arrangement allows for image recordings at repetition rates up to 10 kHz at a resolution of 456 × 416 pixels. The exposure time was set to 75 µs at an intensifier gain of 75 as a compromise amongst a reasonable SNR, a short exposure time, and the usage of the dynamic range of the camera. The repetition rate fulfilled the Nyquist-Shannon theorem of proper signal sampling of the expected HFD frequency, and the short exposure time avoids unintentional averaging of the chemiluminescence signal. The signals from pressure transducers, located at various positions at the combustor, and the camera trigger were recorded with a *National Instrument* data acquisition card at a sampling rate of 50 kHz.

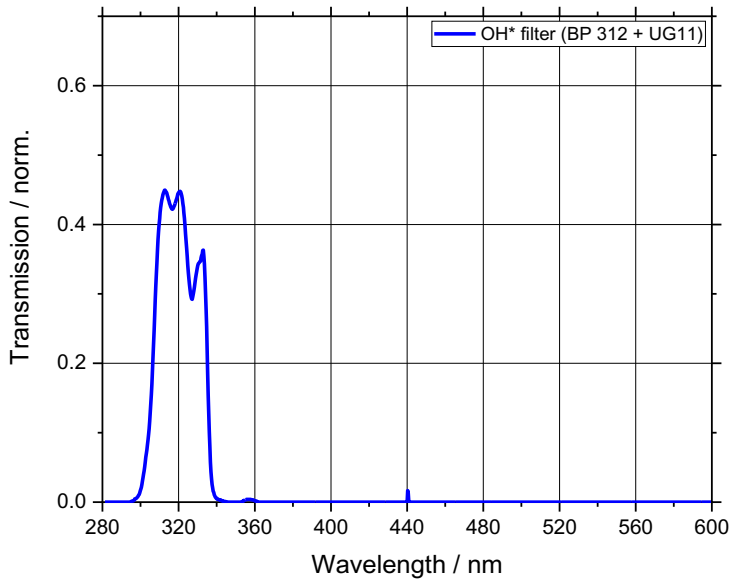

Figure 5.23: Transmission of the chosen filter combination for selective detection of OH^* chemiluminescence at the HBK-4.

A set of six test points was selected at three different pressure levels (0.8, 1.2, and 1.4 MPa) and varying fuel splits, in particular different pilot fuel portions, known to be prone to thermo-acoustic instabilities from earlier investigations.

Results

For each test point, an image series of 10,000 single-shot images was recorded. The resulting average chemiluminescence images for each test point are shown in Figure 5.24, sorted by the respective pressure (increasing from left to right). Each individual test point is named TP followed by a number as indicated in the upper left corner of each image.

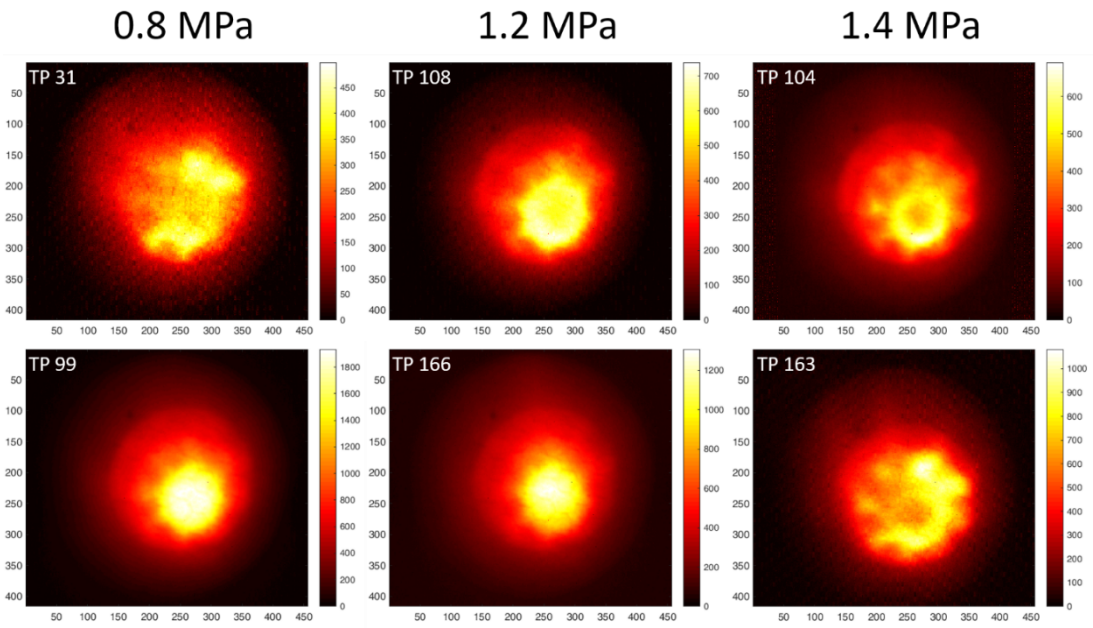

Figure 5.24: Averaged OH^* chemiluminescence intensity images for the investigated test points. The intensity scale of each chemiluminescence image is indicated by the respective colorbar.

The averaged chemiluminescence intensity images of more pilot-stage driven flames such as TP 99, TP 108, and TP 166 indicated a more confined flame with areas of high chemiluminescence intensities in the center of the burner, i.e., the approximated position of the pilot- and D-stage, independent from the pressure level whereas the main-stage driven flames, i.e., TP 31, TP 104, and TP 163, showed a wider spread, although TP 104 was found to tend to a smaller and more centered flame as well.

Although all test points showed significant pressure oscillations around the expected frequency, related oscillations in the chemiluminescence signal could only be observed for TP 163. This is possibly attributable to either the reabsorption of the chemiluminescence signal by ground

state OH at high pressures and a large optical path length, which can be exhibited depending on the selected measurement position and flame geometry [16, 54, 60] or to flame properties such as local equivalence ratio, local turbulence intensity, strain rate or flame stretch, resulting in a diminished chemiluminescence signal [31, 63, 157].

For the analysis of the coherence between chemiluminescence intensity fluctuations and the pressure oscillation, a matrix size w of 40 pixels was selected. The analysis of TP 163 showed very good agreement of chemiluminescence intensity and pressure signal at a maximum coherence level of $\gamma^2_{I_{Cl},p,\max} = 0.89$ at an oscillation frequency of $f = 1.15 f_0$ with f_0 as the normalized critical frequency of the burner, as shown in the graph on the left-hand side in Figure 5.25. The threshold was set to $\gamma^2_{I_{Cl},p} \geq 0.85$. The right side of the figure shows the averaged chemiluminescence image in which the possible spatial origins of the flame oscillations are indicated by squares of size $w \times w$, representing the regions of high coherence and high frequency coincidence. Such indications are referred to as localizations in the following.

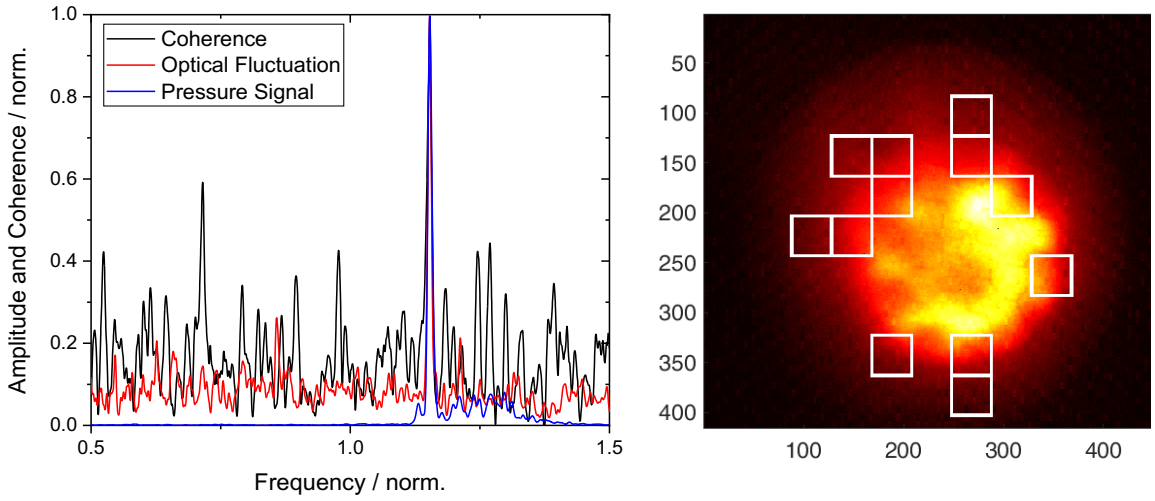

Figure 5.25: Temporally averaged chemiluminescence intensity image (OH^*) of TP163 with marked areas of high coherence.

As can be seen from the figure, the localized areas of high coherence are found in the outer region of the flame, where a strong interaction of the main stage with the pilot stage can be presumed. A more accurate determination is complicated by the slight offset of the viewing axis from the burner axis, as well as the line-of-sight nature of the chemiluminescence imaging measurement. However, a temporally varying fuel concentration occurs in this region for the burner type considered [2], which is a significant driving mechanism for instabilities.

5.3.3 NDP-1 Measurements

As for the measurements at the NDP-1, two different designs of HR3 burner of the SGT5-4000F were subject of the investigations. The general description of the combustor is given in section 5.2.2. In order to avoid repetition, reference is made to the details provided there.

Experimental Setup

As mentioned above, the measurements of the SGT5-4000F combustors were conducted at the atmospheric NDP-1 test rig. No endoscopic probe was required as the rig features multiple points of optical access through windows inside the vessel (see 4.4.1). The exhaust window was selected in order to achieve a top view onto the combustor and thus the flame. The general setup is shown in Figure 5.26.

Again, the *Phantom V7.3 CMOS* high-repetition-rate camera was used and combined with the *LaVision high-speed IRO* image intensifier. An *EADS UV 1.8f* objective was mounted onto the intensifier and different band pass filters were placed in front of the objective in order to discriminate OH^* (series A) and CH^* (series B), respectively. The leading surface of the detection system, i.e., the surface closest to the burner, was located approximately 3300 mm away from the burner exit plane. The detection system was mounted onto optical rails and placed as close as possible to the quartz window to minimize the optical restriction by the window diameter, thus increasing the resulting FOV. The resolution of the camera was set to 800 × 600 pixels at a recording rate of 2 kHz and an exposure time of 500 µs. The signal from the pressure transducers and the camera trigger signal were recorded simultaneously with a *Teledyne LeCroy WaveSurfer MXs-B* at a sampling rate of 50 kHz.

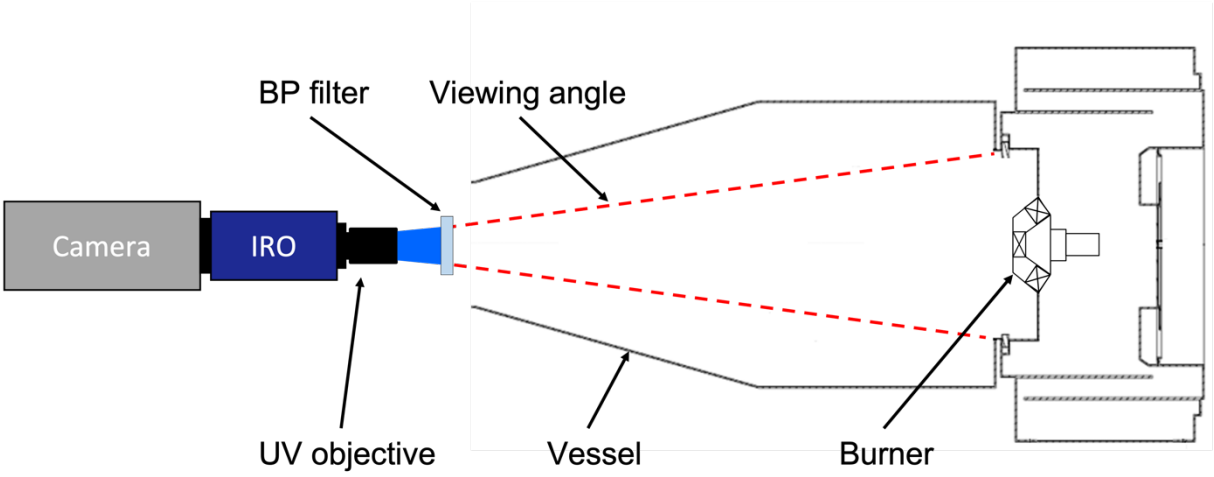

Figure 5.26: Setup at the NDP-1 test rig.

As mentioned above, the emission of two different chemiluminescence species was recorded. Therefore, two different optical band pass filters were used. For the OH^* emission, the combination of the *Semrock* BP 312 with UG 11 was used, while the CH^* emission was discriminated with a Chroma band-pass filter (BP 434). The transmission properties of each filter setup are shown in Figure 5.27.

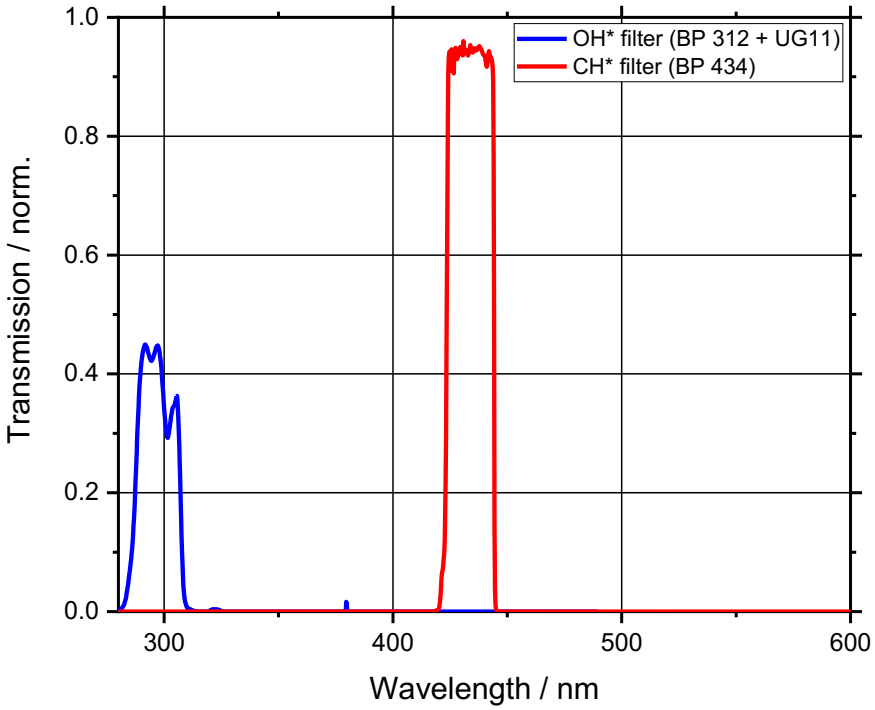

Figure 5.27: Transmission properties of the selected optical filters at the NDP.

Results NDP-1

The experimental setup at the NDP-1 allowed for a perpendicular and straight view onto the burner hardware and flame, respectively. In addition, the atmospheric nature of the NDP-1 permitted longer unstable test points since the lower absolute pressure fluctuation does not risk major damage to the test rig or burner hardware. For the first campaign, a dated burner design with a cylindrical burner outlet (CBO) (hereinafter referred to as series A) was used and test points were selected. In contrary, the second burner version was a state-of-the-art version (series B) and therefore test points with combustion instabilities during high-pressure testing were se-

lected and scaled to the atmosphere conditions within the NDP-1. Figure 5.28 shows the averaged images of each test point of the series A with increasing pilot split from left to right and rising global equivalence ratio from top to bottom. The central blocking in the center line was caused by the emission probe. These images were recorded with a mounted OH* interference filter. The circular shape of the images is caused by the duct following the optical window (in viewing direction), thus limiting the aperture. Reflections of the flame from the ceramic inlay of the combustion chamber were suppressed sufficiently, yet still visible to a certain extent.

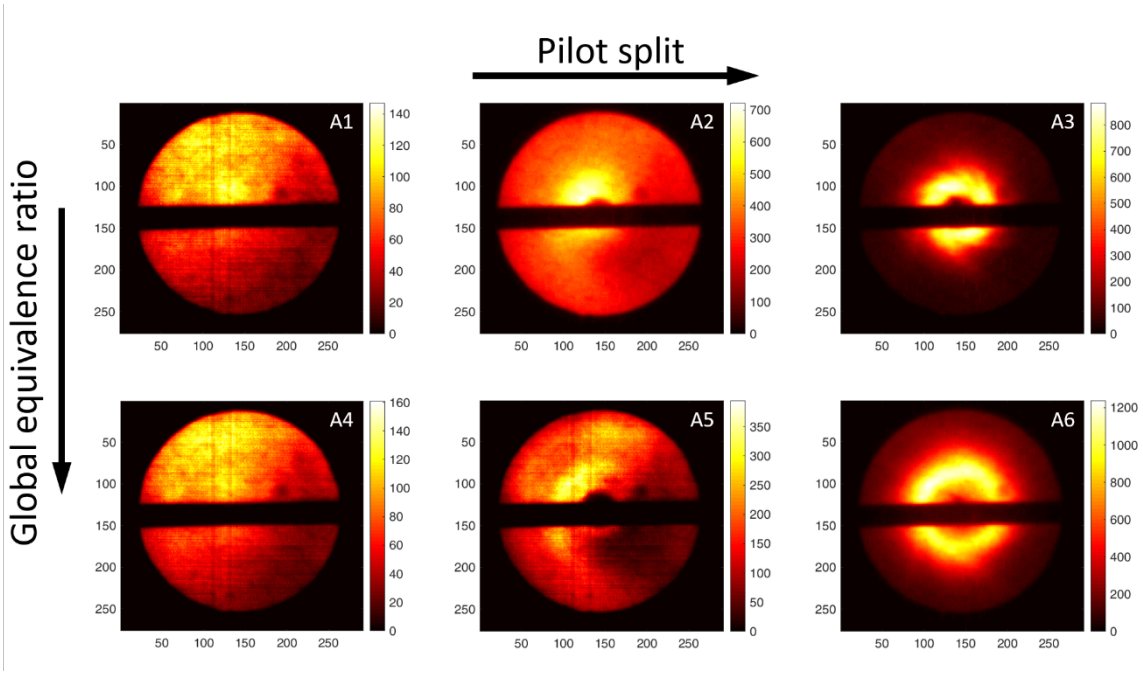

Figure 5.28: Averaged images of the OH* chemiluminescence emission of series A. The intensity scale of each chemiluminescence image is indicated by the respective colorbar.

As seen from the figure, the main stage-driven flames (A1, A2, A4 and A5), represented by the averaged OH* chemiluminescence, seem to favor the upper left corner inside the combustion chamber while the flame collapses with an increasing pilot split towards the center of the burner forming a confined torus (A3 and A6). The orientation of the flame to one side has been observed before in high-pressure measurements by Witzel et al. [15]. In particular, the averaged image in the middle of the bottom row (A5) resembles former high-pressure test with a similar 4000F burner [15]. An average of each flame is presented in Figure 5.29. Although recorded at different pressures, both images showed a distinct separation of the main and pilot stage, and the averaged chemiluminescence image of the flame featured an arc-like shape instead of a full circle as it would be expected. In the high-pressure image, the FOV did not cover the complete flame, thus an optical origin of the shape was presumed. This explanation can be excluded for

the atmospheric measurements at the NDP-1, since the angle of view was perpendicular to the burner and the FOV, except for the area of the emission probe and the duct, was not affected or blocked. In consequence, the observed effect might originate from local signal quenching due to high turbulence intensity or to air entrainment into the flame, such as cooling air [31, 63]. Although the high-pressure rig features cooling air entrainment, this explanation is unlikely for the NDP-1 vessel since it does not feature air entrainment in the vicinity of the flame. The only possibility would be leakage air entering through one of the ports in the vessel. In consequence, the observed quenching is likely to result from high turbulence intensity in this area of the flame.

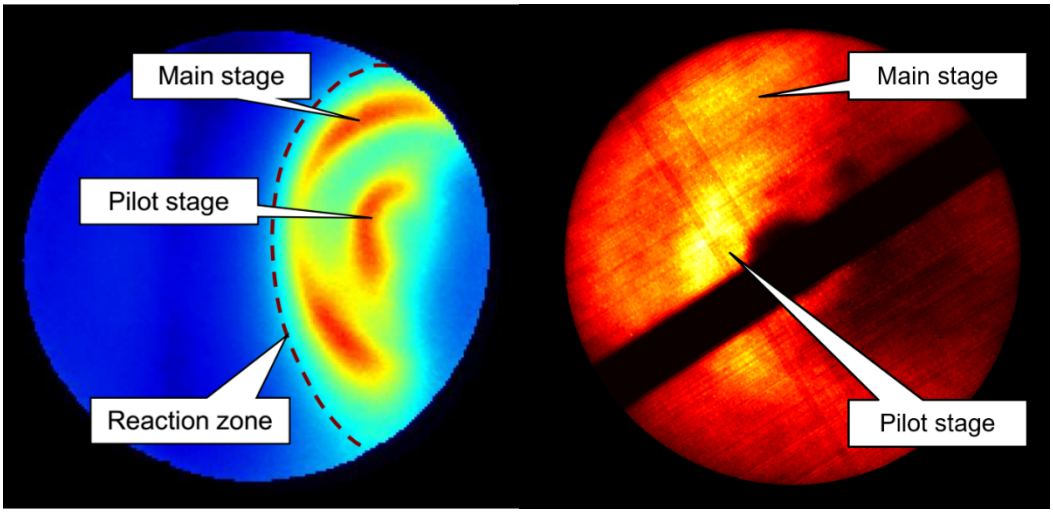

Figure 5.29: Comparison of averaged chemiluminescence images (OH^*) of the 4000F burner at 0.9 MPa at the HBK-4 (left) and at 0.1 MPa at the NDP-1 (right).

The coherence analysis was performed for four test points (A1, A4, A5, A6) as shown in Figure 5.30 and Figure 5.31. The results are inconclusive since the analysis showed very good agreement between the frequencies of the pressure and the optical fluctuations, resulting in a high coherence level of $\gamma^2_{I_{Cl},p,\max} = 0.99$ for the test points A1, A4, while for the test points A5, A6 a significant shift in frequency between these signals was detected, resulting in low coherence levels of only $\gamma^2_{I_{Cl},p,\max} = 0.30$ and $\gamma^2_{I_{Cl},p,\max} = 0.43$, respectively. In consequence, no significant relations between the pressure and the optical fluctuations were observable for these test points. This indicates that the fluctuations of the chemiluminescence intensity result from mechanisms such as local flame stretch, local change of temperature, or local high turbulence rather than from the combustion instabilities [31, 63]. The thermal excitation mechanism of OH^* can be neglected as the contribution of this mechanism to the overall OH^* generation is comparably low for the expected flame temperatures [62, 77, 158, 159]. Although reabsorption of the OH^*

emission by ground state OH [60] is unlikely at atmospheric conditions for lab-scale flames it might affect the image of full-scale flames. In addition, general transmission losses might be significant due to the long optical path from the recording system to the flame inside the vessel. To provide a more robust analysis, simultaneous spectral measurements should be performed in future experiments.

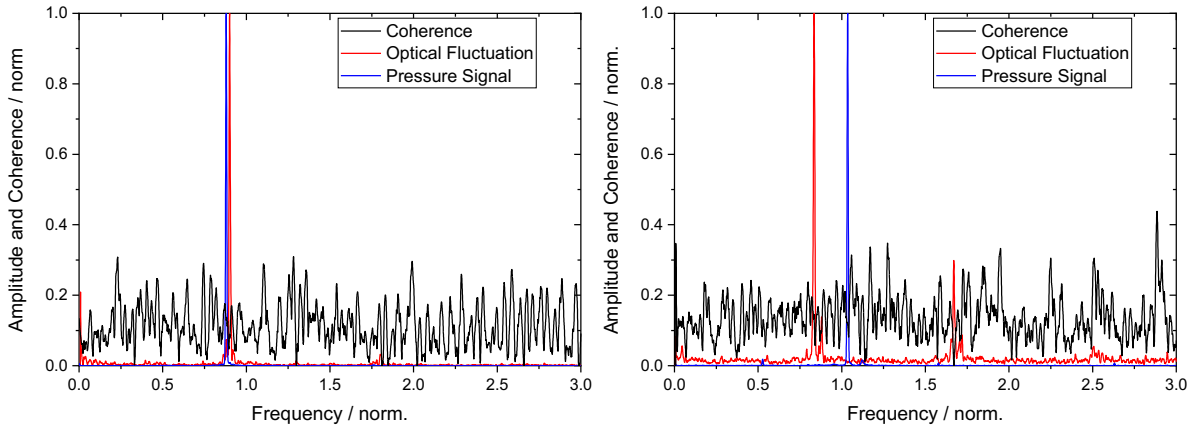

Figure 5.30: Frequencies and resulting coherence for test points A5 (left) and A6 (right) of image series A.

In the pressure and chemiluminescence oscillation for test points A1 and A4, numerous peaks were observed, with the most dominant one approximately at the normalized frequency f_0, which represents the critical frequency of the engine [6] and thus is set to one in the graphs. The reconstruction of the spatial origin of the detected oscillations leads to similar results for both images as indicated by the white rectangles in the averaged chemiluminescence images on the right-hand side of Figure 5.31. The threshold was set to $\gamma^2_{I_{Cl},p} \geq 0.95$. For both test points, the reconstruction indicates the lower right in the flames as the origin of the oscillations. As described above, these areas could be characterized by high turbulence intensity, with potentially significant fluctuations in the equivalence ratio ϕ' and could be investigated further, e.g., in DNS simulations with a defined mesh.

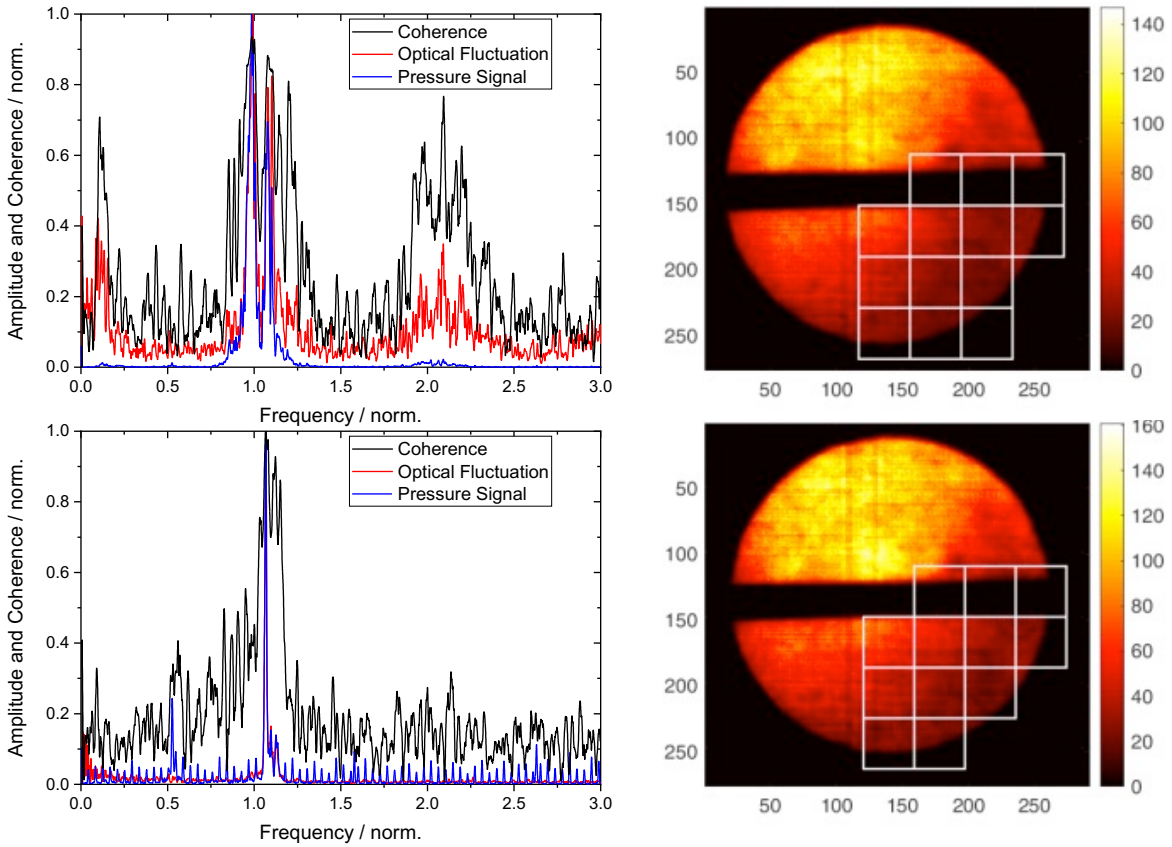

Figure 5.31: Frequencies and coherence analysis for test points A1 (top row) and A4 (bottom row) of image series A with a matrix size of 40 pixels. The intensity scale of each chemiluminescence image is indicated by the respective colorbar.

The series B images were recorded with the CH* interference filter mounted in front of the intensifier. The test points were selected based on real engine load points where thermoacoustic oscillations occurred during high-pressure testing, supposedly in different spatial locations. The temporal averaged chemiluminescence images are shown in Figure 5.32. Apparently, the background reflection was less efficiently blocked by the filter, as even the images of the more confined flames (B3 to B5) show significant signal in non-flame areas. The images in the top row (B1 and B2) are assigned to flames anchored closer to the turbine inlet (represented by the exhaust duct of the vessel), while the lower ones (B3 and B5) are assigned to flames anchored closer to the burner exit, thus further away from the turbine inlet. The image in the middle (test point B4) represents a flame supposedly located halfway between the burner exit plane and the exhaust duct of the vessel. Also, these flames tend slightly to the left, but less pronounced in comparison to the series A images. The test points B4 and B5 featured wide-spread flames where the maximum field of view was occupied, and the outer area of the flames were blocked

by the limited optical access caused by the duct following the window in the head end of the NDP-1 (see Figure 4.11).

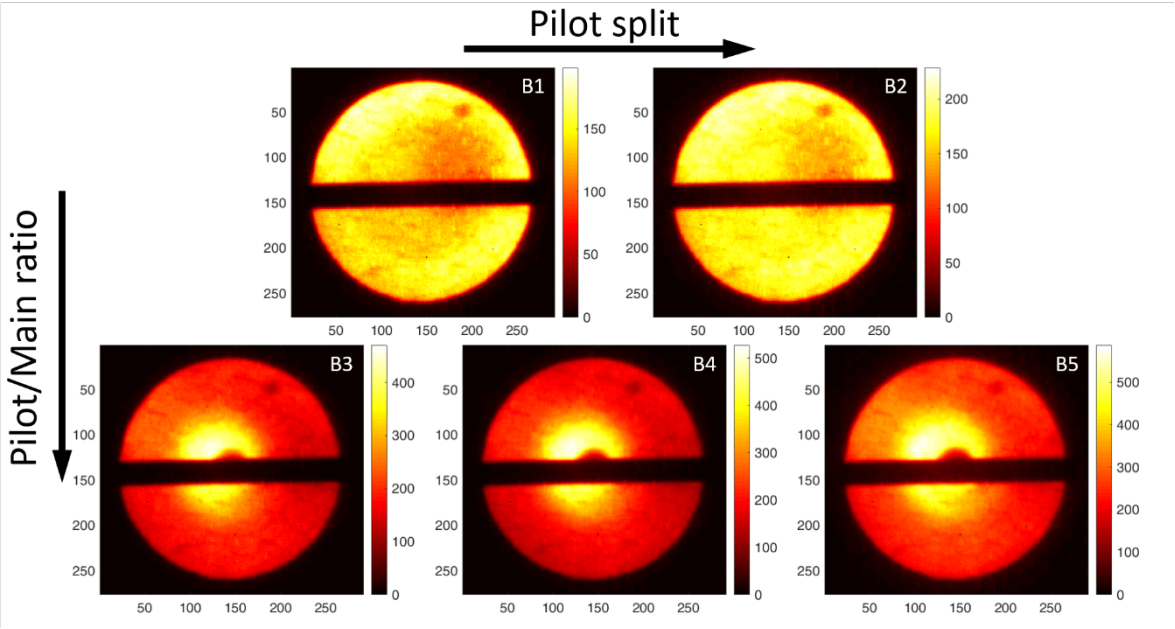

Figure 5.32: Averaged images of the CH* chemiluminescence emission of the NDP-1 image series B. The intensity scale of each chemiluminescence image is indicated by the respective colorbar.

In contrary to series A, the series B results of the coherence analysis showed a good agreement between the pressure and the chemiluminescence oscillation, i.e., the optical fluctuation for all test points, as can be seen on the left-hand side in Figure 5.33 and Figure 5.34. The strongest oscillations, both optical- and pressure-wise, were recorded for the test points with lower Pilot/Main ratios, i.e., with a higher gas portions of the main stage of the burner. In the following, these points are described as main-stage driven. These test points (B1 and B2) are shown in Figure 5.33. All points show a clearly visible dominant frequency at approximately $f = 0.82 f_0$ and two of its multiples f_{01} and f_{02}, hence, the dominant frequency for this design of the burner was found to be lower compared to the the design of series A. A high coherence of $\gamma^2_{I_{Cl},p,\max} = 0.99$ was calculated for all test points at these dominant frequencies. Albeit this may lead one to the conlcusion, that the CH* is a more suitable marker, it has to be mentioned that the significant shift in phase between the pressure fluctuations and the intensity of CH* reported in the literature [150] is not mimicked properly as the coherence does not account for a difference in phase [152, 153].

Althought significantly correlated, the coherence decreases for the first f_1 and second f_2 multiple for all test points. For example for test point B2, the coherence was calculated to

$\gamma^2_{Cl,p,01} = 0.97$, and $\gamma^2_{Cl,p,02} = 0.75$ for the first and second multiple, respectively. This might be caused by non-correlated input signal portions or by a more pronounced non-linear system response at higher frequencies. Nonetheless, the coherence levels were high enough to prove a correelation between the pressure and the optical signal even at higher frequencies.

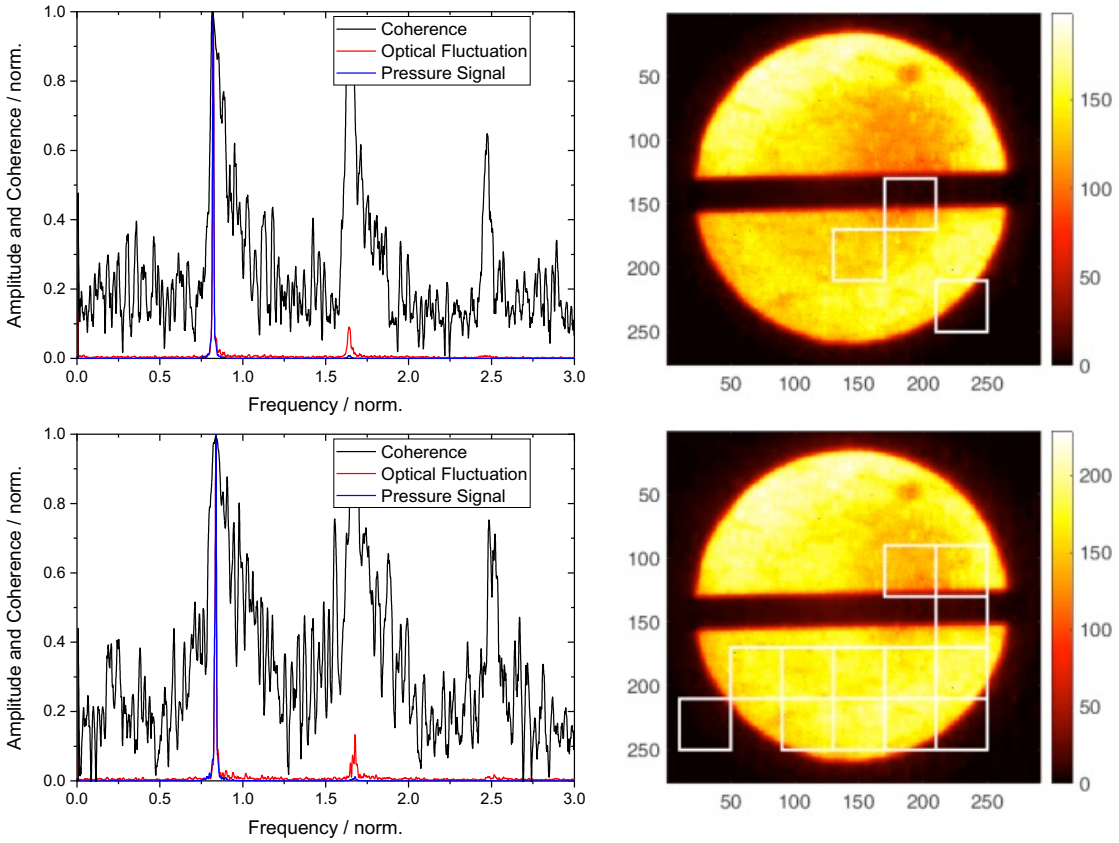

Figure 5.33: Frequencies and coherence analysis for test points B1 (top row) and B2 (bottom row) of image series B with a matrix size of 40 pixles. The intensity scale of each chemiluminescence image is indicated by the respective colorbar.

The reconstruction of the areas of high coherence for test points B1 and B2 within the averaged chemiluminescence image are shown on the right in Figure 5.33. For test point B1, three sub-matrices were reconstructed with two of them located near the center of the image and one at the bottom right. The two areas close to the center might point towards the mixing region of pilot and main stage. The other region might be a result of oscillation of the flame in its outer region. However, a statement on this effect is burdened with the uncertainty that parts of the flame were not visible due to the optical blocking caused by the test rig design. For test point B2, the complete region below the emission probe (the central blocking within the images) as well as two areas above are reconstructed. The reconstructed area in the lower left of the image indicates a possible inadequacy of the chosen geometry of the submatrices, as well as the fact

that the reconstruction of the submatrix at point $P = (x_{local}, y_{local})$ may lead to a spatial inaccuracy of the reconstruction, since this matrix is only connected to the flame in its upper right corner. The coherence analysis and reconstruction for test points B3 to B5, which are characterized by a higher pilot/main ratio and thus referred to as pilot-driven flames, are shown in Figure 5.34.

Again, all test points showed a good agreement between chemiluminescence emission and pressure, resulting in the high coherence levels as mentioned earlier, as seen from the graphs on the left. As for the reconstruction, no clear trend was observed for the pilot-driven test points. For test point B3 (top row), two areas in the lower right of the flame were reconstructed, while for test point B4 (middle row) additional areas below the probe and closer to the center as well as one area above the probe were reconstructed. Lastly, for test point B5 (bottom row), almost the complete area in the proximity of the emission probe was reconstructed alongside areas in the lower right corner. As all averaged chemiluminescence images appear similar, no unambiguous explanation for the reconstructed areas could be derived from the analysis.

Comparing the number of reconstructed areas within the main-stage and the pilot-stage driven flames, it appears that the number of reconstructed areas increases with the pilot split, i.e., a higher amount of gas fed through the pilot stage. Although in general, a higher pilot split stabilizes the flame, it might cause a change of the shear layer location. Another explanation might be given by the position of the flame inside the test vessel. As mentioned above, the supposed location of the flame differs for the test points. Fluctuations within flames closer to the burner exit would appear in a smaller region on the detector, while fluctuation closer to the exhaust would appear larger. In consequence, for lager objects, the number of reconstructed areas increases and vice versa. This explanation does not hold for test points B1 and B5. Nonetheless, a more detailed study should be carried out in order to investigate this tendency in more detail.

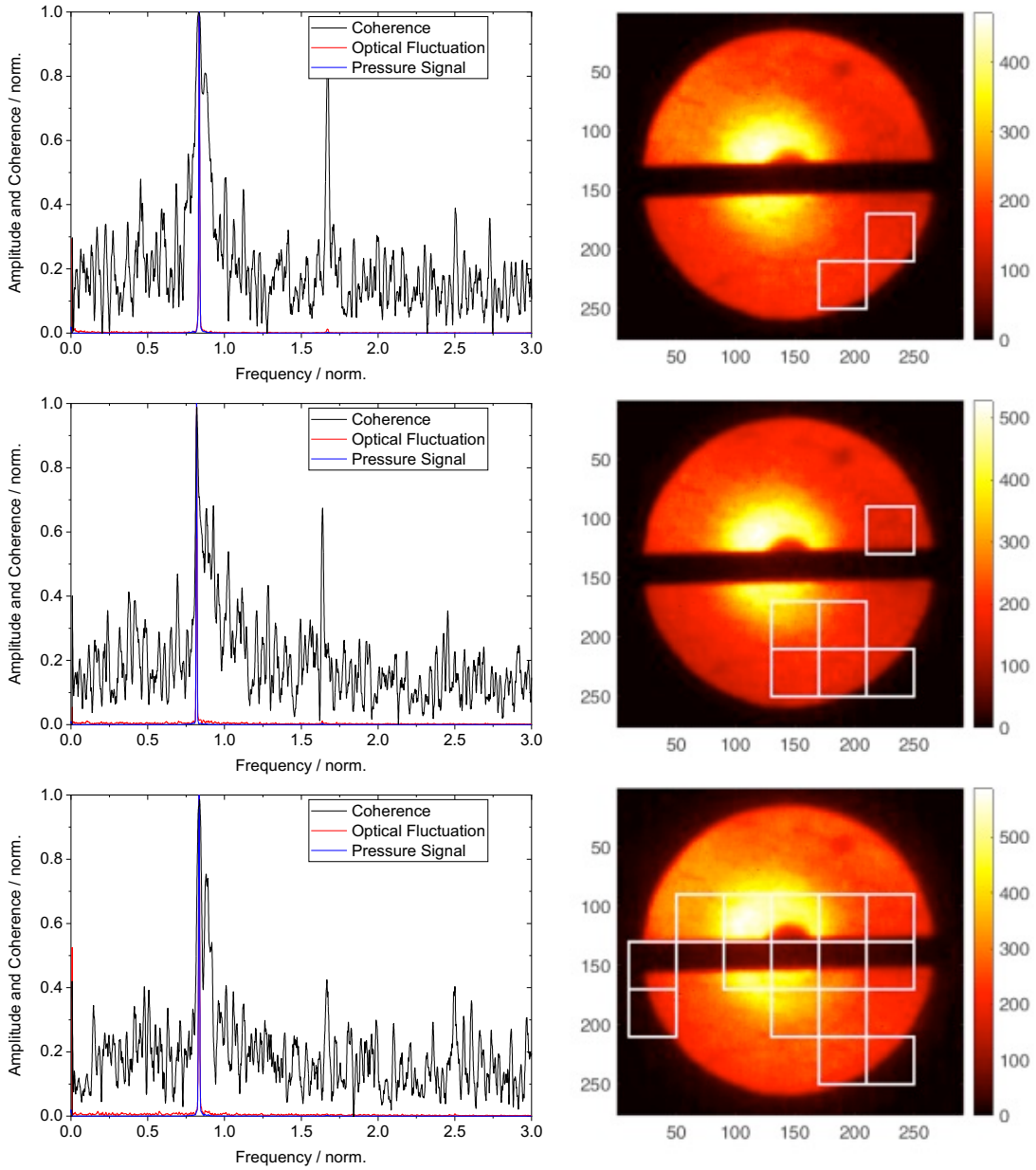

Figure 5.34: Frequencies and coherence analysis for test points B3 (top row), B4 (middle row), and B5 (bottom row) of image series B with a matrix size of 40 pixles. The intensity scale of each chemiluminescence image is indicated by the respective colorbar.

In general, all test points for image series A and B tend to favor the lower part of the image as most reconstructed areas were found there. One possible explanation might be a slight asymmetry of the flame caused by the redirection of the compressor exit air, which enters the compressor simulation section at the NDP-1 from above. Nonetheless, such an asymmetry is not supported by the averaged chemiluminescence images.

5.3.4 Conclusions

In the above section, flame chemiluminescence intensity images and pressure fluctuation measurements for real scale GT combustors at elevated and at atmospheric were presented. A post-processing routine for correlating the fluctuations within the chemiluminescence signal and the pressure fluctuations was established to avoid a misleading interpretation of the recorded chemiluminescence signal as the origin of these fluctuations might differ from combustion instabilities. In addition, the routine allowed for a spatial localization of areas featuring a strong correlation, i.e., high coherence levels, between these two signals. In general, the routine was developed as an attempt to utilize the comparably robust application of imaging chemiluminescence measurements as diagnostic tool for identifying regions of combustion instabilities during high-pressure rig testing, which could be investigated further during the development process of new combustor designs.

For the high-pressure measurements, a solid level of coherence, hence, a good correlation was found for the recorded image series which showed significant fluctuations within the chemiluminescence signal. As a result, only one test point at high pressure was available for testing the routine, showing again the general issue of using chemiluminescence emission as heat release marker in turbulent premixed flames as the chemiluminescence signal is subject to quenching and reabsorption. Nonetheless, in cases of well correlated signals chemiluminescence imaging might indicate locations inside a particular combustor, which could be of interest for deeper investigations to analyze the thermoacoustic behavior of the combustor.

At the NDP-1, a total of eleven test points was recorded for two different HR3 burner designs. For images series A, the emission of OH^* was recorded, while the image series B was directed towards the emission of CH^*. In general, the coherence analysis indicates that CH^* is a more suitable marker as for all test points where high levels of coherence were calculated compared to only two test points of series A. The former conclusion might be challenged by the effect of the neglected possible shift in phase for CH^* emission and pressure fluctuations and by the fact that two different burner designs were used in the study. Nonetheless, the results for OH^* indicate the general suitability of the developed routine as a robust tool to separate unrelated fluctuation in the chemiluminescence emission during the investigation of combustion instabilities. Consequently, the use of the routine avoids misinterpretations of recorded chemiluminescence images.

Although the localization indicates certain areas, the measurements are limited by the general issue of the line-of-sight integration of the optical signal which cannot reliably predict the location of the fluctuations along the flame and thus, does not account for effects such as the consumption of equivalence ratio perturbations along spatially extended reaction zones of a technically premixed flame.

5.4 Wall Temperature Measurements

This section, including all figures, was previously published by Nau et al. in Ref. [46]. My contribution within the scope of this work was the realization of the optical access using the flexible probe assembly and the adaptation of the modular probe head for the input optics and single fiber used. The figures and references were renumbered according to this thesis.

5.4.1 Introduction

The cooling design of gas turbines plays an important role in the efficiency and overall performance of gas turbines. On the one hand, a high turbine inlet temperature is desired to achieve high efficiencies. On the other hand, cooling air is needed to protect the walls from excessive temperatures. However, cooling air has a direct impact on the efficiency and emissions of a gas turbine. Therefore, the exact knowledge of the wall temperature is important to determine an optimal cooling air flow. However, combustion tests of gas turbines are usually performed in test rigs, where only limited information from inside the gas turbine is available. While inlet and outlet conditions, and cold-side temperatures are monitored, the surface temperatures inside the combustor are often unknown.

Various online and offline wall temperature measurement techniques exist. Thermocouples are widely used and can provide temperatures with good precision. The main drawback of this technique is, that it is intrusive and wiring can be difficult. Another online technique is pyrometry. It requires optical access to the combustor. However, due to interferences from flame emissions and reflected radiation in the combustor the accuracy is limited [160]. Thermal indicating paint is a widely applied offline technique. The paint is applied to the wall before the combustion test and the color change interpreted after testing to obtain isotherms at the color change temperature. The precision is however limited and only the maximum temperature during the test cycle is obtained. Phosphor thermometry is a technique utilizing phosphorescent particles. These particles consist of a ceramic host doped with transition or rare earth metals.

Temperature can be measured online with high precision [161–164], although also an offline variant exists [165]. Phosphor thermometry is based on the temperature dependence of the emission characteristics of phosphorescent materials. After excitation with light (preferably a laser pulse), these materials emit light, after several internal energy transfer processes. Non-radiative quenching reduces the lifetime of the phosphorescence at high temperatures. The temperature dependence of the lifetime is therefore a precise indicator of the temperature.

One of the challenges at large combustion test rigs is the limited optical access. Due to the arrangement of the combustor inside the pressure housing, a fiber coupled setup is often the only solution. Fiber coupled remote phosphor thermometry has been performed before on a stator vane doublet at atmospheric pressure [166]. A fiber bundle with different fibers for laser delivery and phosphorescence collection was used. The distance between fiber probe and phosphor coated wall was only 26 mm. A single fiber setup has the advantage of simpler and cheaper design and higher collection efficiencies. However, fluorescence and Raman scattering generated as the excitation laser pulse is transmitted through the fiber can interfere with the phosphorescence. To overcome this issue excitation of the anti-Stokes shifted phosphorescence has been proposed. This way, the emission wave- length of the thermographic phosphor is shifted to a region with less influence from interference generated in the fiber [167].

In this work, we present the first successful wall temperature measurements with fiber coupled online phosphor thermometry at the Siemens CEC test facility. Online wall temperatures could be obtained during high-pressure combustion tests up to 8 bar. During the campaign temperatures up to almost 1600 K were measured using the phosphor YAG:Dy. Here we demonstrate single fiber phosphor thermometry with gated signal detection, to overcome problems associated with fast, laser induced interference signals. Details of the setup and the measurement procedures will be presented. Strong influences on the signal from flame emissions could be observed. We present strategies for correcting for background emission to increase measurement precision and will discuss data evaluation procedures.

5.4.2 Experimental and Data Evaluation

In this section, the optical access to the combustor wall will be explained first. Then the optical setup, the data evaluation procedures, and the calibration process will be explained.

Test Facility and Optical Access

The probe was applied to a Siemens high-pressure combustion test rig, operated at the Siemens Clean Energy Center (CEC) test facility in Ludwigsfelde near Berlin. The facility holds three testbeds with exchangeable combustion rigs. External compressors and air preheaters provide engine-like thermodynamic boundary conditions such as maximum rig pressures of 4.0 MPa, and maximum air inlet temperature of 870 K at air mass flows up to 50 kg/s. The left side of Figure 5.35 gives a schematic drawing of the test facility.

The combustion test rig consists of a pressure vessel containing an exchangeable flow box, which mimics all mid-frame engine features like the compressor exit diffusor and the first turbine vane section. One pressure vessel can hold different burners by simply replacing the flow box. To account for the different engine pressure levels, the rig pressure is adjustable by a back-pressure valve.

To achieve optical access to the combustor, the fiber probe is guided through the pressure vessel and the flow box to the combustor wall. The feedthrough port in the pressure vessel serves as a pressure barrier and needs to meet all safety regulations of the pressure equipment directive. To minimize the required modifications on the pressure vessel, the feed-through approach is based on a non-centric port in a flange lid of the vessel, thus enabling different feedthrough positions by either turning the lid or by changing its position. A stuffing seal is attached to the lid to hold and seal the fiber probe while offering the opportunity to adjust the penetration depth to account for different length requirements for each targeted measuring position.

The flow box is located inside the pressure vessel, and thus, the pressure difference over its walls is negligible. Subsequently, the port definition was easier, and no seals were necessary. Despite this, the feedthrough in the flow box holds an important task, i.e., to stabilize the probe to avoid vibrational fatigue due to the high flow velocities inside the flow box. The basis of the port is a two-piece lid featuring a large round non-centric cutout for easy probe installation.

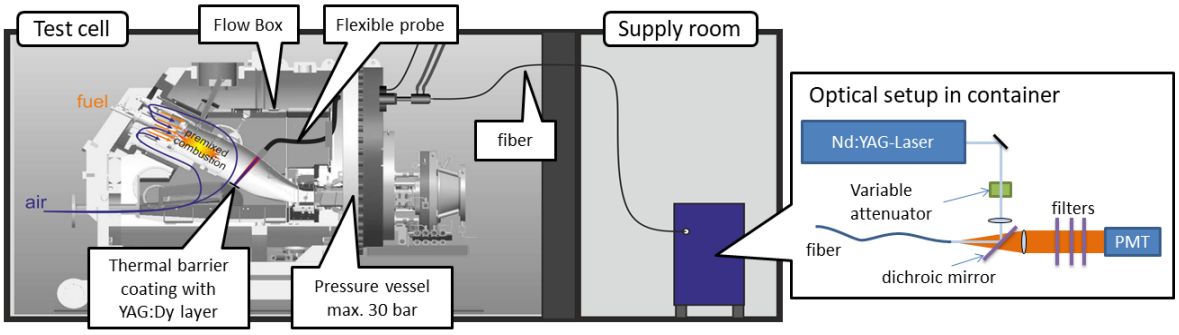

Figure 5.35: Schematic of the high-pressure test rig with modular optical probe and optical setup [46].

To secure the probe tip position at the combustor wall, a custom-made adapter was welded onto the can (Figure 5.36). It was manufactured using additive manufacturing (AM), which was an important key factor in realizing advanced functions of internal cooling and purge air distribution. In addition, AM enables to meet the free-form surface of the can, and to select the measurement position by fixing the probe slightly tilted. The head is tightened with screws and a high-temperature, pressurized metallic toric joint prevents leakage air entering the combustion chamber at the probe feed through. In addition to holding the head, the adapter also serves to inject nitrogen into the probe to purge the sapphire window of the probe and cool the probe tip.

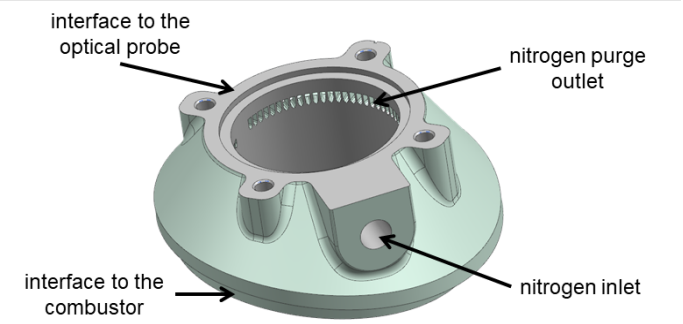

Figure 5.36: Schematic of the adapter for holding the probe head and nitrogen purging [46].

Modular Optical Probe

Given the special experimental conditions, the probe had to meet several requirements. Besides the protection of sensitive optics, the probe had to be flexible and modular. Flexibility to allow different routing inside the rig and compensate thermal expansions and modularity for using the probe for different optical diagnostics by changing the optics and fiber in the probe. The probe consists of three main assembly groups. First, the modular probe head. Second, the flexible cooling body, and third a rigid section at the end with the water supply. The probe assembly is shown in Figure 5.37.

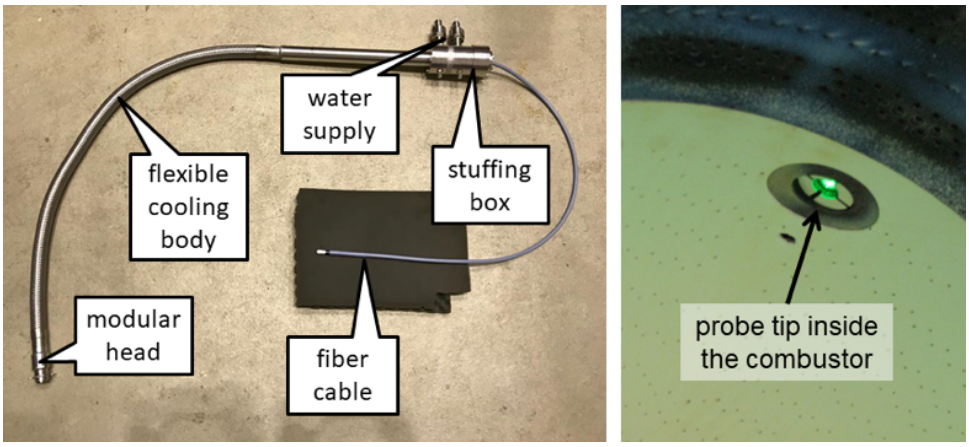

Figure 5.37: Photograph of the assembled modular probe (left) and the probe tip inside the combustor (right) with a green alignment laser coupled into the fiber [46].

The underlying concept is a tube-in-tube heat exchanger, thus providing efficient cooling in a closed system. The inner tube served as the inlet section. This way the coldest water surrounded the sensitive fiber. The outer tube was the outlet section, cooling the metal portion of the probe. The head was mounted onto the customized can adapter and was produced by additive manufacturing. Consequently, fine inner cooling channels could be integrated into the head and the high-temperature alloy Hastelloy X could be used as material. The integrated cooling channels realized the reversal of the cooling water deep in the front of the probe head. The modular optics holder was made of Ampcoloy to take advantage of the higher thermal conductivity and thus improve the cooling performance of the optics. The modular head (see Figure 5.38) contained the optics for laser delivery and signal collection. The front window holder at the tip of the head holds the front sapphire window (diameter 20 mm) hat was sealed by two mica foil rings. The front of the probe head was coated with a protective layer of ceramic thermal barrier coating. Nitrogen was used for front optics purging and cooling. It reached all the way to the probe tip, where the nitrogen exited into the combustor, forming a purging curtain to cool and clean the front sapphire window.

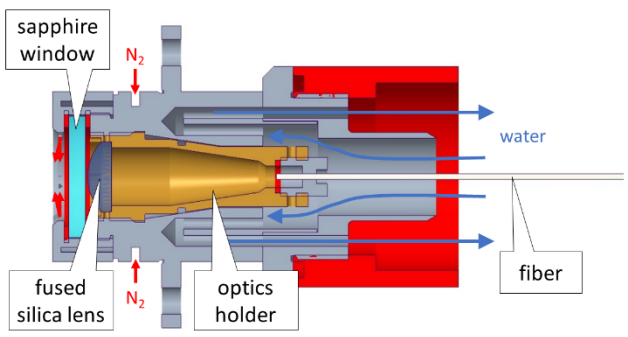

Figure 5.38: Schematic of the modular optical head of the probe [46].

A large core multimode fiber (*FVA1000*, *LaserComponents*, high-OH, 1 mm core, silica/silica) was used for delivery of excitation pulses and detection of the laser-induced emission of the thermographic phosphor. The fiber was glued into the fiber holder, which was threaded into the optic holder and sealed from the cooling water by an FKM O-ring. The optic holder was threaded into the main probe head and sealed by a second FKM O-ring in the conical surface. A single fused silica lens (diameter 12.7 mm, f = +20 mm, UV-AR coated) was used to collimate the laser light and collect the phosphorescence.

Optical Measurement Setup

A mobile measurement container was used for the phosphorescence measurements. Using an 18 m long glass fiber allowed the container to be placed in a quieter auxiliary room near the test rig. This container protects all optics and electronics from vibrations and other environmental influences and simplifies setting up the experiment. A schematic of the optical setup is shown in Figure 5.35 on the right. A Nd:YAG laser (*Spitlight 600*, *Innolas GmbH*, 15 Hz repetition rate, 6 ns pulse length at 355 nm) was used for excitation of the phosphor coating. The laser beam passed a continuously variable attenuator to control the laser energy. Then the beam was focused with a lens (f=+75 mm) with the focal point a few millimeters in front of the tip of a large core fiber. The laser radiation was guided with this fiber to the optical probe at the test rig. The collimation optics (f = +20 mm) in the probe formed a 30 mm laser spot on the TBC wall coated with thermographic phosphor at the opposing side of the combustor (distance about 40 cm). The efficiency of laser coupling and transmission was about 70 %. Using laser energies of 2.2 mJ the energy density on the TBC was about 0.2 mJ/cm^2.

Phosphorescence light was collected with the same optics and fiber and guided back to the measurement container. In the container the phosphorescence light passed a dichroic mirror to separate it from the laser light. An additional long pass filter (*FELH0400*, *Thorlabs*) was used to further suppress laser radiation and a cold glass filter (*KG3*, *Schott*) reduces thermal radiation. A band pass filter centered at a Dy emission line (center wavelength 458 nm, bandwidth 10 nm) reduced remaining interfering emissions. The transmitted light was collected with a photomultiplier tube (PMT) with gate function (*H11526-20-NF*, *Hamamatsu*). The gate function of the PMT was necessary to avoid saturation of the PMT due to thermal radiation in periods between the laser pulses and even more important to suppress a short intense spike at the

beginning of the decay trace. The gate was switched on for 1 ms before the laser pulse to capture the offset level from background radiation. Then the PMT gate was switched off for 1 µs and switched on again to capture the phosphorescence decay trace. Sample decay traces with the gating scheme are shown in Figure 5.40 a). PMT signals were captured with an oscilloscope (*DSO7034B*, *Agilent Technologies*, 350 MHz, input impedance 500 Ω) and transferred to a computer running a *LabVIEW* program for online signal processing and data storage. The main parameters of the optical setup (laser energy, filter selection and gating of the PMT) could be controlled remotely from the rig control room.

Data Evaluation

The phosphorescence signal can be described as an exponentially decaying curve

$$I(t) = o + A\mathrm{e}^{-t/\tau} \tag{1}$$

with intensity I at time t, amplitude A, offset o and decay rate τ. The decay rate is typically determined with a nonlinear fitting process. However, in reality the decay curve shows multi-exponential behavior. As a result, the obtained decay rate depends on the section of the decay curve used for the data evaluation, when a mono-exponential fit is used. Therefore, the mono-exponential model is combined with a carefully controlled fitting window. One approach proposed by Brübach et al. [168] defines the start and end time of the fitting window ($c_1 \times \tau$ and $c_2 \times \tau$) based on the decay rate. Therefore, an iterative fitting process is needed to determine τ. In this investigation $c_1 = 0.2$ and $c_2 = 2$ were used. The selection of c_1 and c_2 is a trade-off between signal quality and usually interfering signals at the beginning of the curve. A late fitting window shows more noise because the signal is weaker, but the beginning of the curve is sometimes affected by interfering signals like fluorescence.

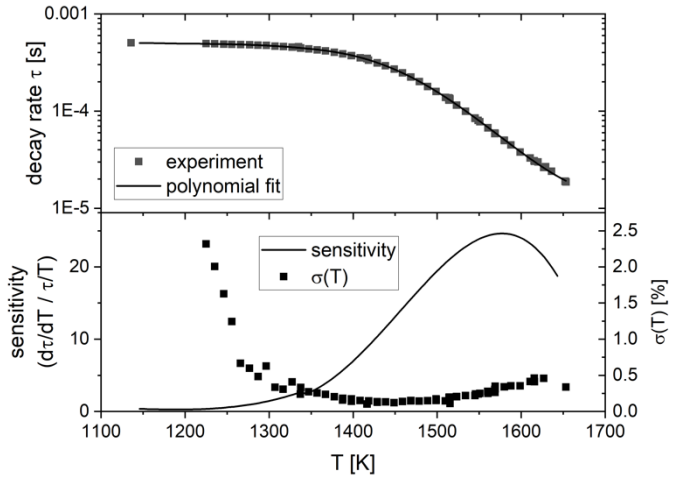

Figure 5.39: Calibration measurements for YAD:Dy on coated TMC sample (top) and temperature sensitivity and standard deviation $\sigma(T)$ of the phosphor (bottom) [46].

Phosphor Coating and Calibration Procedures

Phosphor coatings were applied with a mixture of a commercial binder (LRC, ZYP coatings) with the phosphor powder (YAG:Dy, Phosphor Technology). A mixing ratio of 0.2 g phosphor powder to 1 ml binder was used. The mixture was spray painted onto the surface with an air brush (Badger 100). To increase homogeneity of the coating, several layers were painted and dried with a heat gun after each layer. At the combustor a surface area on the TBC surface of about 5 × 5 cm^2 was coated.

For calibration measurements a small sample of TBC was used. A small piece of TBC coated steel substrate (about 4 × 4 cm^2) was treated with aqua regia (hydrochloric and nitric acid, ratio 1:3) for several hours until the coating dissolved from the steel substrate. This TBC piece was coated with the same phosphor and binder mixture as the surface at the CEC. The layer thickness on the sample was controlled with a coating thickness gauge (*TE 1250-0.1FN*, *Sauter*) on a separate steel sample to achieve a thickness of about 20 µm. Calibration measurements were performed in an optically accessible furnace *(LAC*, *VP 10/16*, *Boldt Wärmetechnik GmbH*). The sample was placed inside the furnace with a reference thermocouple (type B) close to the sample. The decay rate of the phosphorescence is then measured step-wise at different temperatures. Laser setup, detection setup and electronics were identical between calibration and combustor measurements. The laser energy density on the surface was 0.2 mJ/cm^2 for both cases to avoid systematic errors due to different laser energies.

The measured decay rate for temperatures between 1150–1650 K is shown in Figure 5.39. In addition the sensitivity obtained from the polynomial fit to the decay rates in shown. The sensitivity is the normalized derivative of the fitted trace. The temperature sensitive range of this phosphor starts at about 1350 K. In this temperature range the precision is between 0.1–0.5 %, determined from the standard deviation σ of 150 individual laser shots. Additional errors from the calibration procedure (mainly the reference temperature measurement inside the furnace) contribute by 0.5–0.7 % to the total error.

5.4.3 Results and Discussion

Sample decay traces measured at the CEC test rig are shown in Figure 5.40 a). The used gate scheme for the PMT is indicated with the shaded area. The data was taken from a 1200 shots (80 s) long data set during the first day of the measurement campaign. Gating of the PMT was mainly necessary to remove an intense spike at the beginning of the decay trace. This initial spike could not be suppressed with filters and is therefore not just scattering at the laser wavelength. It has been reported before that Raman scattering and fluorescence from the fiber itself is observed especially in configurations were a single fiber is used for laser and signal delivery [166]. An excitation wavelength of 355 nm was used like in this work. At 365 nm detection wavelength no useful measurements were possible, while at 456 nm (almost identical to the detection wavelength of 458 nm used here), the initial spike was still present, but much smaller due to the larger wavelength shift to the excitation wavelength. The initial spike observed in this work was stronger than the phosphorescence signal and would have caused severe distortion of the decay trace due to saturation of the PMT. The gated PMT is an elegant and simple solution for this problem. An alternative solution could be the use of fiber bundles and spectral filtering inside the probe head, as proposed by Eldridge et al. [166]. This is more costly than a single fiber setup and reduces collection efficiency. Also the utilization of blue-shifted phosphorescence by excitation of anti-Stokes luminescence has been demonstrated [167]. This is, however, not applicable for every phosphor material.

The single-shot decay traces show very strong interferences from flame emissions, probably from CO_2^*, which shows broad-band emission [16, 54]. These emissions made it impossible to evaluate single shot decay rates reliably. After ten averaged laser shots the situation has already significantly improved, and decay traces can be evaluated. As can be seen in Figure 5.40b, a slight systematic shift for less than 100 averaged laser shots is observed. At 100 averaged laser

shots the standard deviation is around 1 % (15 K) and does not reduce much with further averaging. This is probably due to actual temperature variations on the wall and not due to errors from the data evaluation. Therefore, for further analysis 100 laser shots were averaged. This is a compromise between precision and measurement time (100 laser shots correspond to 6.7 s measurement time).

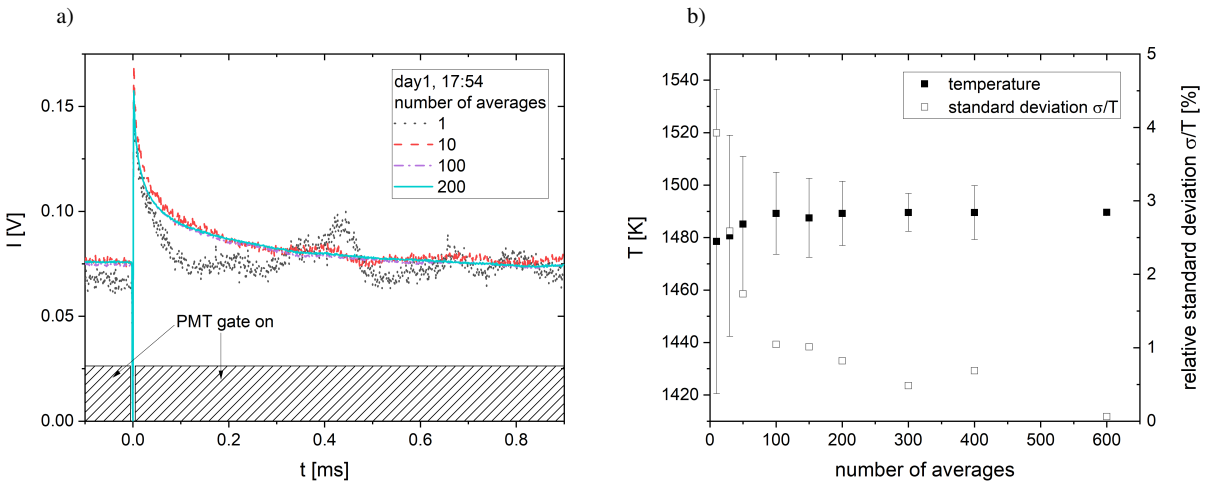

Figure 5.40: a) Sample decay curves after averaging of 1–200 single pulses. The PMT gate is shown as shaded regions at the bottom. b) Obtained temperature and standard deviation for different amounts of averaged single pulses using the same data set [46].

Online wall temperatures for the two measurement days are shown in Figure 5.41. At both days, measurements were performed at up to 8 bar. Measurements were performed during test rig heating up, ignition, load variation and finally burner shut down. Typically, a series of 900 laser shots was captured for each measurement point shown. Temperatures below 1400 K during test rig heating up are less reliable due to the reduced sensitivity of the phosphor in this temperature region. However, at final test conditions the temperatures rise to about 1500 K where the selected phosphor shows very good sensitivity as can be seen in Figure 5.39. At the second measurement day the signal level was lower than on the first day, probably due to degradation of the phosphor coating.

During both measurement days several conditions of the burner were tested. These conditions will be discussed together with the measured cold side temperatures from thermocouples and calculated adiabatic flame temperatures in the following section. In Figure 5.42a, temperatures are shown for different test conditions at both measurement days. It can be seen, that all three temperatures follow a similar trend. Especially the lowest temperature for condition 9 is well captured. However, there are some notable differences, for example between condition 4–7 the

adiabatic flame temperature and inside wall temperature decrease, while the thermocouple temperature shows an opposite trend.

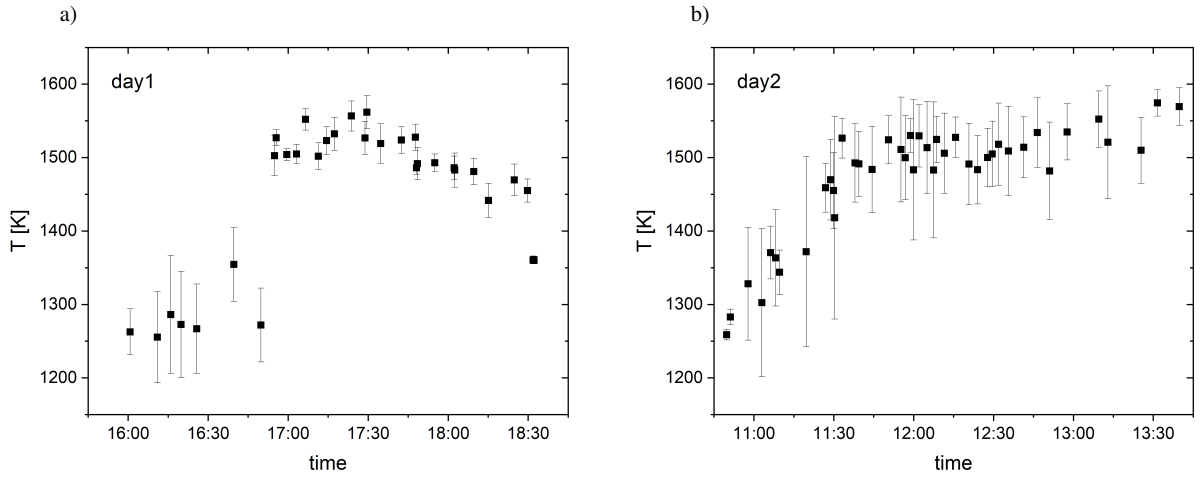

Figure 5.41: Measured wall temperatures at the CEC at the two measurement days [46].

This might be explained by the fact, that the thermocouple temperature measurement on the outer wall of the combustor also depends on additional factors such as the flow conditions in the flow box. Condition 12 and 16 are almost identical test conditions (marked with circles in Figure 5.42a). These conditions were measured at the same day with a time difference of 1.5 h. It can be seen that wall temperatures measured with thermographic phosphors are also almost identical (1511 and 1510 K). This shows the good reproducibility of the technique.

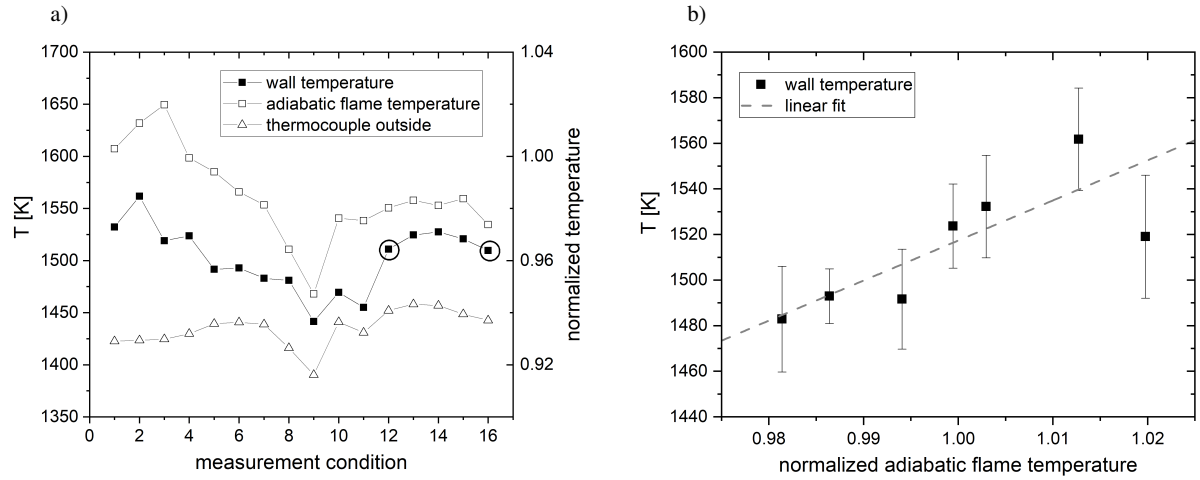

Figure 5.42: a) Wall temperatures (closed symbols) and normalized temperatures (open symbols) for selected measurement conditions from both measurement days. Lines are drawn for clarity. b) Wall temperature plotted against the normalized adiabatic flame temperature [46].

For a selected series of test conditions, the wall temperatures are plotted against the calculated relative adiabatic flame temperatures at the measurement location in Figure 5.42b). A linear relationship between both temperatures can be observed, as expected. However, the measured temperatures at a normalized adiabatic flame temperature of 0.994 and 1.02 seem to be too low. To ensure this is not an artifact from the data evaluation procedure we tested different fit settings (e.g., early and late fitting windows and bi-exponential instead of a mono-exponential fit). This did however not change the obtained temperatures significantly. In future measurement campaigns this could be investigated further.

To improve signal quality and precision some strategies are planned. The limiting factor was the interference from flame emissions, as discussed above. A second PMT could be used to capture only the broadband flame emissions without the phosphorescence. At 410 nm YAG:Dy shows almost no phosphorescence [45], while CO_2^* shows still pronounced emissions [16, 54]. At 410 nm the flame emission spectrum is free from CH^* emissions, like also the phosphorescence spectrum at 458 nm. The measured background signal could be subtracted from the decay trace to remove the unwanted fluctuations. Another approach could involve a high-speed laser to improve the averaging at a given measurement time. At the observed temperatures around 1500 K the decay rates are about 0.1 ms. Therefore, a repetition rate of about 1 kHz could be used without significant overlap between consecutive phosphorescence traces.

5.4.4 Conclusions

Fiber coupled phosphor thermometry has been successfully applied at a full-scale high-pressure gas turbine test rig to measure wall temperatures inside the combustor in real-time. To obtain optical access a modular optical probe was developed. The probe features a modular optical head that allows different front optics to be installed. For laser delivery and signal transmission a single 18 m long large-core optical fiber was used. A mobile measurement system was developed, that contains all necessary optics and electronics. The system allows online evaluation of the measured phosphorescence signals. A gated PMT was necessary to shut the PMT off between the laser pulses and to remove a strong spike (probably luminescence generated inside the long fiber) at the beginning of the phosphorescence decay trace. A combination of commercial binder and YAG:Dy phosphor was used to coat the TBC wall inside the combustor. The durability of the coating was appropriate for the measurement campaign but could be improved for example by embedding the phosphor into the TBC layer.

During the measurement campaign the capability of the technique could be demonstrated, and online wall temperatures were measured. The reproducibility of the technique could be shown, and temperatures were compared with calculated flame temperatures and thermocouple temperatures on the combustor outside wall. Further campaigns could focus on test conditions where exact knowledge of the inside wall temperature is crucial.

Due to the strong interferences from flame emissions, 100 laser shots had to be averaged to achieve reliable phosphorescence signals. Signal collection could be improved in further investigations to allow single-shot temperature measurements. A strategy could involve a second PMT with a bandpass filter at a different wavelength (e.g. around 410 nm) to capture the flame emissions without the phosphorescence and subtract this signal from the decay trace. This way the measurement precision could be improved.

6 Summary and Outlook

6.1 Summary

The increasing requirements imposed on the combustion system of stationary gas turbines due to the constant changes in the energy market led to systems that enable the most efficient energy conversion possible but have become significantly more complex due to the characteristic high-turbulence and lean combustion. As a result, the development effort has increased continuously. In general, such systems are intensely investigated in elaborate high-pressure tests prior to their use in gas turbines. The effort involved in these tests and their high costs provide the incentive to achieve the highest possible information density during such tests. The application of optical measurement techniques may support an increased information density and allow for more detailed studies of complex combustion phenomena. In order to enable regular or more frequent use of optical measurements, this work aimed to develop a fiber-based flexible probe together with the associated test rig access, which allows optical access for various optical measurement methods.

In the work reported in this thesis, multiple designs of a flexible fiber-based probe were engineered and tested, all based on the construction concept of a tube-in-tube heat exchanger. Each design comprised a probe head, a cooling body, and a water supply portion. The exchangeable head of the final design (CEC head) featured inner cooling channels for water and nitrogen and accommodated optics holders for the input optics. The holders were customized for each set of input optics and the last holder was equipped with an O-ring seal to seal the input optics from the cooling water. The front surface of the window holder was coated with TBC to decrease the thermal input from the flame into the probe. A corrugated metal hose and a polytetrafluoroethylene tube were used as outer and inner tube of the cooling body, respectively, and provided, in combination with the *Nanjing 20k* fiber bundle, the required flexibility. A rigid end portion at the proximal end of the cooling body allowed different penetration depths. Nitrogen was supplied to the probe head via the adapter on the combustor can by a separate supply line. The

water supply section accommodated cooling water inlet and outlet as well as thermocouple ports. The probe was successfully deployed during two consecutive days of high-pressure testing and was operated at boundary conditions of up to 1.6 MPa rig pressure and 780 K co-flow temperature. The probe exhibited a good thermodynamic performance with a cooling power of approximately 34 kW and maintained a flowback temperature well below the maximum operating temperature of the fiber bundle.

Chemiluminescence imaging were carried out at three different test rigs, namely the NDP-1, the HBK-4, and the CEC under atmospheric (NDP-1) and high-pressure conditions. At the NDP-1, fiber-based measurements with an intensified CCD camera and high-speed measurements utilizing optical windows with an intensified high-speed CMOS camera were carried out. For each measurement, the signal was filtered for OH^* or CH^*, respectively, via the corresponding bandpass filters. For the optical access to the high-pressure rigs, an existing rigid fiber-based probe (HBK-4) and the newly developed probe (CEC) were used.

The fiber-based measurement at the NDP-1 as well as the measurements at the CEC aimed for a determination of the flame length and flame position in the respective combustor. For the purpose of flame length measurements, a post-processing routine was developed for identifying the flame object within the recorded chemiluminescence images. With the routine, the flame position and flame length were investigated for the HR3B burner of the SGT5-4000F engine and for an experimental design of the ULN burner of the SGTx-8000H. The routine combines the thresholding method developed by Otsu with calculations of the image entropy to identify the optimal threshold that most accurately characterizes the flame object. The optimal threshold met the constraints of the lowest standard deviation of the calculated flame length and highest image entropy at the transition region between flame and background. Afterward, the images were binarized, the background signal was omitted, and the final flame length was calculated. The routine was found to reliably detect the flame object within the images even for poor SNR. Statistical evaluations of flame length or its standard deviation and of the CO or NO_x emission did not show a clear correlation. The investigated experimental ULN burner featured an additional fuel stage downstream of the main burner referred to as cross stage, and was visualized for the first time in a high-pressure single combustor test. The number of distinguishable flame objects matched the number of injection nozzles within the field of view of the selected input optics. The results revealed a relatively low impact of the main flow on the flame of the cross stage, as the flame objects were detected close to the area of the injection positions in axial direction.

High-speed chemiluminescence imaging measurements during single combustor tests of SGT5-4000H burners at the HBK-4 under high-pressure conditions (0.9–1.2 MPa) and at the NDP-1 (non-fiber-based) at atmospheric conditions were directed at determining the feasibility of using high-speed imaging chemiluminescence measurements to investigate the spatial origin of combustion-induced oscillations. The aim was to localize areas of high chemiluminescence intensity fluctuation, which correlate with the pressure fluctuations caused by combustion-induced oscillations. Hence, the signal from the pressure transducers and the trigger signal of high-speed camera were recorded simultaneously. The developed post-processing routine used the signal-analytical approach of the so-called coherence analysis to determine the correlation between the chemiluminescence intensity fluctuations and the pressure fluctuations. The routine divided each single-shot image of an image series into a set of submatrices to determine the intensity fluctuation within each submatrix and to calculate the coherence between these fluctuations and the pressure fluctuations. When a strong correlation, i.e., high coherence, was determined, the corresponding submatrices were white-framed in the averaged chemiluminescence to indicate the spatial origin of the flame-induced oscillations in the burner under study. For the measurements at the HBK-4, an OH^* filter was used. Although all test points showed significant intensity variations, only one test point showed a significant correlation between these and the pressure variations, again confirming the difficulties of using OH^* as a heat release marker. For the remaining test point, however, the developed evaluation routine identified the presumed interaction zone between the main and pilot stage of the ULN burner as a possible origin for the registered combustion-induced fluctuations, which could thus be investigated in more detail in further studies or by means of simulations. The studies at the NPD-1 were performed either with an OH^* or CH^* filter and a total of eleven test points was recorded. Under the present conditions, as well as neglecting any phase shifts between intensity and pressure signals due to the principle, CH^* was indicated to be a more suitable marker for the heat release rate, since higher coherence levels were identified.

The modularity of the developed probe design was demonstrated by using the probe during the wall temperature measurements of the flame tube performed by Nau et al. [46] using thermographic phosphors. During these measurements, the cooling body, the water supply portion, and the developed test rig feedthrough design were used at the CEC test rig. Only the probe head was adapted to the optics and the single fiber used. Thus, the probe could be successfully used for two different optical measurement techniques at high-pressure combustion chamber test rigs.

6.2 Outlook

The fiber-based flexible probe developed within this thesis work was applied to full-scale gas-turbine combustor test rigs during high-pressure rig testing and demonstrated its modularity during imaging chemiluminescence measurements and wall temperature measurements with thermographic phosphors. In future designs, the probe could be extended to facilitate simultaneous measurements of spectral and imaging chemiluminescence measurements by incorporating a single-core fiber parallel to the imaging fiber bundle and connecting it to a spectrometer.

Using imaging chemiluminescence measurements in conjunction with the post-processing routine developed, the spatial expansion of the flame was successfully examined in different burners. However, further measurements with defined test point parameters should be carried out to investigate correlations between flame length and additional measurement data such as CO or NO_x exhaust concentration as the current database is not sufficient for an assessment.

Similar results were obtained with regard to flame oscillation measurements. Some operating points could be examined successfully using the evaluation routine developed. However, more data would be required to validate the efficiency of the proposed method. Furthermore, numerical simulations of the operating points should be carried out, where a possible spatial origin of the oscillations was determined. To further increase the benefit of imaging chemiluminescence measurements, it would be crucial to close the interpretation gap between imaging chemiluminescence measurements and CFD simulations by mimicking line-of-sight integration of CFD data during post processing.

Furthermore, especially to avoid the problem of the line-of-sight integration of the chemiluminescence signal, the optical access should be extended to include more simultaneous viewing angles to allow for the reconstruction of the three-dimensional flame shape using computed tomography of chemiluminescence (CTC) [80, 81] to further improve the understanding of the combustion process inside full-scale gas-turbine combustors.

In a further step, the use of imaging fiber bundles could be abandoned and instead, miniaturized CMOS or CCD cameras could be placed directly into the probe head. With correspondingly small camera systems, the dimensions as well as the cooling requirements of the probe could be further reduced.

7 References

[1] *World Energy Outlook 2019, IEA*, https://www.iea.org/reports/world-energy-outlook-2019 (2019)

[2] B. Witzel, *Application of Optical Diagnostics to Support the Development of Industrial Gas Turbine Combustors*. Dissertation (Duisburg, Essen 2016)

[3] C. Lechner, J. Seume, *Stationäre Gasturbinen* (Springer Berlin Heidelberg, Berlin, Heidelberg 2003)

[4] S.A. Greenwood, Proceedings of the 29th Turbomachinery Symposium Texas A&M University. Turbomachinery Laboratories (2000), *Low Emissions Combustion Technology For Stationary Gas Turbines Engines*

[5] B.F. Kock, B. Prade, B. Witzel, H. Streb, M.H. Koenig, Proceedings of the ASME Turbo Expo GT2013-95569 (2013), *Combustion System Update SGT5-4000F: Design, Testing and Validation.*

[6] W. Krebs, P. Flohr, B. Prade, S. Hoffmann, Combustion Science and Technology 174, 99 (2002), *Thermoacoustic Stability Chart for High-Intensity Gas Turbine Combustion Systems*

[7] J. Lepers, W. Krebs, B. Prade, P. Flohr, G. Pollarolo, A. Ferrante, Proceedings of the ASME Turbo Expo GT2005-68246 (2005), *Investigation of Thermoacoustic Stability Limits of an Annular Gas Turbine Combustor Test-Rig With and Without Helmholtz-Resonators*

[8] P. Kaufmann, W. Krebs, R. Valdes, U. Wever, Proceedings of the ASME Turbo Expo GT2008-50755 (2008), *3D Thermoacoustic Properties of Single Can and Multi Can Combustor Configurations*

[9] C.O. Paschereit, B. Schuermans, V. Bellucci, P. Flohr, *Implementation Of Instability Prediction In Design: Alstom Approaches*, in: T.C. Lieuwen, V. Yang (eds), *Combustion Instabilities In Gas Turbine Engines* (American Institute of Aeronautics and Astronautics, Reston ,VA 2006)

[10] U. Gruschka, B. Janus, J. Meisl, M. Huth, S. Wasif, Proceedings of the ASME Turbo Expo GT2008-51208 (2008), *ULN System for the New SGT5-8000H Gas Turbine: Design and High Pressure Rig Test Results*

[11] B. Janus, J. Bigalk, L. Helmers, B. Witzel, Y. Ghermay, M. Huth, C. Johnson, K. Landry, R. Sunshine, Proceedings of the ASME Turbo Expo GT2014-27015 (2014), *Successfully Validated Combustion System Upgrade for the SGT5/6-8000H Gas Turbines: Technical Features and Test Results*

[12] D. Noble, D. Wu, B. Emerson, S. Sheppard, T. Lieuwen, L. Angello, Journal of Engineering for Gas Turbines and Power 143 (2021), *Assessment of Current Capabilities and Near-Term Availability of Hydrogen-Fired Gas Turbines Considering a Low-Carbon Future*

[13] C. Vandervort, D. Leach, D. Walker, J. Sasser, Proceedings of the ASME Turbo Expo GT2019-91594 (2019), *Commercialization and Fleet Experience of the 7/9HA Gas Turbine Combined Cycle*

[14] J. Marra, Final Technical Report, DOE-SEI-42644 (2015), *Advanced Hydrogen Turbine Development*

[15] B. Witzel, J. Heinze, B.F. Kock, G. Stockhausen, H. Streb, J. van Kampen, C. Schulz, C. Willert, C. Fleing, Proceedings of the ASME Turbo Expo GT2012-68965 (2012), *Application of Endoscopic OH^*-Chemiluminescence Measurements at a Full-Scale High-Pressure Gas Turbine Combustion Test Rig*

[16] S. Görs, B. Witzel, J. Heinze, G. Stockhausen, J. van Kampen, C. Schulz, C. Willert, C. Fleing, Proceedings of the ASME Turbo Expo GT2014-26977 (2014), *Endoscopic Chemiluminescence Measurements as a Robust Experimental Tool in High-Pressure Gas Turbine Combustion Tests*

[17] J. Lütge, *Optische Messmethoden an Hochdruckbrennkammerprüfständen*. Master Thesis (Duisburg, Essen 2018)

[18] N. Peters, *Combustion Theory. CEFRC Summer School Princeton, June 28th - July 2nd 2010*

[19] P. Gruhlke, *Towards an improved prediction of CO and NO_x emissions from gas turbines by LES*. Dissertation (Duisburg, Essen 2022)

[20] T. Poinsot, D. Veynante, *Theoretical and numerical combustion* (Edwards, Philadelphia 2005)

[21] I. Glassman, R.A. Yetter, N. Glumac, *Combustion* (Academic Press, London, Waltham, MA 2015)

[22] N. Peters, *Technische Verbrennung. Vorlesungsumdruck, RWTH Aachen*

[23] R. Borghi, Progress in Energy and Combustion Science 14, 245 (1988), *Turbulent combustion modelling*

[24] N. Peters, Journal of Fluid Mechanics 384, 107 (1999), *The turbulent burning velocity for large-scale and small-scale turbulence*

[25] J.W.S. Rayleigh, Nature 18, 319 (1878), *The Explanation of Certain Acoustical Phenomena*

[26] J. O'Connor, V. Acharya, T. Lieuwen, Progress in Energy and Combustion Science 49, 1 (2015), *Transverse combustion instabilities*

[27] V. Sharifi, *Investigation of High-Frequency Thermoacoustic Instabilities*. Dissertation (Duisburg, Essen 2021)

[28] T. Lieuwen, H. Torres, C. Johnson, B.T. Zinn, Journal of Engineering for Gas Turbines and Power 123, 182 (2001), *A Mechanism of Combustion Instability in Lean Premixed Gas Turbine Combustors*

[29] T. Lieuwen, B.T. Zinn, Symposium on Combustion 27, 1809 (1998), *The role of equivalence ratio oscillations in driving combustion instabilities in low NO_x gas turbines*

[30] K.-U. Schildmacher, A. Hoffmann, L. Selle, R. Koch, C. Schulz, H.-J. Bauer, T. Poinsot, W. Krebs, B. Prade, Proceedings of the Combustion Institute 31, 3197 (2007), *Unsteady flame and flow field interaction of a premixed model gas turbine burner*

[31] J.G. Lee, D.A. Santavicca, Journal of Propulsion and Power 19, 735 (2003), *Experimental Diagnostics for the Study of Combustion Instabilities in Lean Premixed Combustors*

[32] T. Dreier, R. Chrystie, T. Endres, C. Schulz, *Laser-Based Combustion Diagnostics*, in: R.A. Meyers (ed), *Encyclopedia of Analytical Chemistry* (John Wiley & Sons, Ltd, Chichester, UK 2006)

[33] H. Krämer, F. Dinkelacker, A. Leipertz, G. Poeschl, M. Huth, M. Lenze, Proceedings of the ASME International Gas Turbine and Aeroengine Congress and Exhibition, 99-GT-135 (1999), *Optimization of the Mixing Quality of a Real Size Gas Turbine Burner With Instantaneous Planar Laser-Induced Fluorescence Imaging*

[34] C. Schulz, V. Sick, Progress in Energy and Combustion Science 31, 75 (2005), *Tracer-LIF diagnostics: quantitative measurement of fuel concentration, temperature and fuel/air ratio in practical combustion systems*

[35] U. Doll, G. Stockhausen, C. Willert, Experiments in Fluids 55 (2014), *Endoscopic filtered Rayleigh scattering for the analysis of ducted gas flows*

[36] U. Doll, G. Stockhausen, J. Heinze, U. Meier, C. Hassa, I. Bagchi, Journal of Engineering for Gas Turbines and Power 139 (2017), *Temperature Measurements at the Outlet of a Lean Burn Single-Sector Combustor by Laser Optical Methods*

[37] R. Kapulla, S.B. Najera, Measurement Science and Technology 17, 221 (2006), *Operation conditions of a phase Doppler anemometer: droplet size measurements with laser beam power, photomultiplier voltage, signal gain and signal-to-noise ratio as parameters*

[38] C. Tropea, Measurement Science and Technology 6, 605 (1995), *Laser Doppler anemometry: recent developments and future challenges*

[39] C. Willert, C. Hassa, G. Stockhausen, M. Jarius, M. Voges, J. Klinner, Measurement Science and Technology 17, 1670 (2006), *Combined PIV and DGV applied to a pressurized gas turbine combustion facility*

[40] C. Willert, G. Stockhausen, J. Klinner, C. Lempereur, P. Barricau, P. Loiret, J.C. Raynal, Measurement Science and Technology 18, 2504 (2007), *Performance and accuracy investigations of two Doppler global velocimetry systems applied in parallel*

[41] B.F. Kock, *Zeitaufgelöste Laserinduzierte Inkandeszens (TR-LII): Partikelgrößenmessung in einem Dieselmotor und einem Gasphasenreaktor* (Cuvillier, Göttingen 2006)

[42] M. Leschowski, *Ruß-Diagnostik in laminaren vorgemischten Hochdruckflammen*. Dissertation (Duisburg, Essen 2016)

[43] L. Shi, T. Endres, J.B. Jeffries, T. Dreier, C. Schulz, Sensors 22 (2022), *A Compact Fiber-Coupled NIR/MIR Laser Absorption Instrument for the Simultaneous Measurement of Gas-Phase Temperature and CO, CO_2, and H_2O Concentration*

[44] W. Stricker, R. Lückerath, U. Meier, W. Meier, Journal of Raman Spectroscopy 34, 922 (2003), *Temperature measurements in combustion-not only with CARS: a look back at one aspect of the European CARS Workshop*

[45] P. Nau, Z. Yin, O. Lammel, W. Meier, Journal of Engineering for Gas Turbines and Power 141 (2019), *Wall Temperature Measurements in Gas Turbine Combustors With Thermographic Phosphors*

[46] P. Nau, S. Görs, C. Arndt, B. Witzel, T. Endres, Journal of Turbomachinery 143 (2021), *Wall Temperature Measurements in a Full-Scale Gas Turbine Combustor Test Rig With Fiber Coupled Phosphor Thermometry*

[47] M.V. Mekhrengin, I.K. Meshkovskii, V.A. Tashkinov, V.I. Guryev, A.V. Sukhinets, D.S. Smirnov, Measurement 139, 355 (2019), *Multispectral pyrometer for high temperature measurements inside combustion chamber of gas turbine engines*

[48] A.G. Gaydon, H.G. Wolfhard, *Flames - Their structure, radiation and temperature* (Chapman and Hall, London 1979)

[49] A. Brockhinke, C. Schulz, Applied Physics B 107, 513 (2012), *Selected papers about chemiluminescence of flames*

[50] M. Kopp, M. Brower, O. Mathieu, E. Petersen, F. Güthe, Applied Physics B 107, 529 (2012), *CO_2^* chemiluminescence study at low and elevated pressures*

[51] H.N. Najm, P.H. Paul, C.J. Mueller, P.S. Wyckoff, Combustion and Flame 113, 312 (1998), *On the Adequacy of Certain Experimental Observables as Measurements of Flame Burning Rate*

[52] B. Higgins, M.Q. McQuay, F. Lacas, J.C. Rolon, N. Darabiha, S. Candel, Fuel 80, 67 (2001), *Systematic measurements of OH chemiluminescence for fuel-lean, high-pressure, premixed, laminar flames*

[53] B. Higgins, M. McQuay, F. Lacas, S. Candel, Fuel 80, 1583 (2001), *An experimental study on the effect of pressure and strain rate on CH chemiluminescence of premixed fuel-lean methane/air flames*

[54] F. Güthe, D. Guyot, G. Singla, N. Noiray, B. Schuermans, Applied Physics B 107, 619 (2012), *Chemiluminescence as diagnostic tool in the development of gas turbines*

[55] E. Petersen, M. Kopp, N. Donato, F. Güthe, Journal of Engineering for Gas Turbines and Power 134, p (2012), *Assessment of Current Chemiluminescence Kinetics Models at Engine Conditions*

[56] J. Kojima, Y. Ikeda, T. Nakajima, Proceedings of the Combustion Institute 28, 1757 (2000), *Spatially resolved measurement of OH^*, CH^*, and $C2^*$ chemiluminescence in the reaction zone of laminar methane/air premixed flames*

[57] Y. Ikeda, J. Kojima, H. Hashimoto, Proceedings of the Combustion Institute 29, 1495 (2002), *Local chemiluminescence spectra measurements in a high-pressure laminar methane/air premixed flame*

[58] J. Kojima, Y. Ikeda, T. Nakajima, Combustion and Flame 140, 34 (2005), *Basic aspects of OH(A), CH(A), and C2(d) chemiluminescence in the reaction zone of laminar methane–air premixed flames*

[59] B. Prabasena, M. Röder, T. Kathrotia, U. Riedel, T. Dreier, C. Schulz, Applied Physics B 107, 561 (2012), *Strain rate and fuel composition dependence of chemiluminescent species profiles in non-premixed counterflow flames*

[60] A. Brockhinke, J. Krüger, M. Heusing, M. Letzgus, Applied Physics B 107, 539 (2012), *Measurement and simulation of rotationally-resolved chemiluminescence spectra in flames*

[61] M. Bozkurt, M. Fikri, C. Schulz, Applied Physics B 107, 515 (2012), *Investigation of the kinetics of OH^* and CH^* chemiluminescence in hydrocarbon oxidation behind reflected shock waves*

[62] Y. Hidaka, S. Takahashi, H. Kawano, M. Suga, W.C. Gardiner, The Journal of Physical Chemistry 86, 1429 (1982), *Shock-tube measurement of the rate constant for excited hydroxyl ($A^2\Sigma^+$) formation in the hydrogen-oxygen reaction*

[63] M. Lauer, T. Sattelmayer, Journal of Engineering for Gas Turbines and Power 132, 61502 (2010), *On the Adequacy of Chemiluminescence as a Measure for Heat Release in Turbulent Flames With Mixture Gradients*

[64] P. Niegemann, M. Fikri, I. Wlokas, M. Röder, C. Schulz, The Review of scientific instruments 89, 55111 (2018), *Methodology for the investigation of ignition near hot surfaces in a high-pressure shock tube*

[65] S. Shawal, M. Goschütz, M. Schild, S. Kaiser, M. Neurohr, J. Pfeil, T. Koch, SAE International Journal of Engines 9 (2016), *High-Speed Imaging of Early Flame Growth in Spark-Ignited Engines Using Different Imaging Systems via Endoscopic and Full Optical Access*

[66] P.G. Aleiferis, Y. Hardalupas, A. Taylor, K. Ishii, Y. Urata, Combustion and Flame 136, 72 (2004), *Flame chemiluminescence studies of cyclic combustion variations and air-to-fuel ratio of the reacting mixture in a lean-burn stratified-charge spark-ignition engine*

[67] L. Ma, Q. Lei, Y. Wu, W. Xu, T.M. Ombrello, C.D. Carter, Combustion and Flame 165, 1 (2016), *From ignition to stable combustion in a cavity flameholder studied via 3D tomographic chemiluminescence at 20 kHz*

[68] W. Hubschmid, R. Bombach, A. Inauen, F. Güthe, S. Schenker, N. Tylli, W. Kreutner, Experiments in Fluids 45, 167 (2008), *Thermoacoustically driven flame motion and heat release variation in a swirl-stabilized gas turbine burner investigated by LIF and chemiluminescence*

[69] F. Güthe, R. Lachner, B. Schuermans, F. Biagioli, W. Geng, A. Inauen, S. Schenker, R. Bombach, W. Hubschmidt, 44th AIAA Aerospace Sciences Meeting and Exhibit, AIAA 2006-437 (2006), *Flame Imaging on the ALSTOM EV-Burner: Thermo Acoustic Pulsations and CFD-Validation*

[70] F. Biagioli, F. Güthe, B. Schuermans, Experimental Thermal and Fluid Science 32, 1344 (2008), *Combustion dynamics linked to flame behaviour in a partially premixed swirled industrial burner*

[71] A. Fischer, F. Bake, J. Heinze, O. Diers, C. Willert, I. Röhle, Measurement Science and Technology 20, 75403 (2009), *Off-line phase-averaged particle image velocimetry and OH chemiluminescence measurements using acoustic time series*

[72] B.D. Bellows, M.K. Bobba, J.M. Seitzman, T. Lieuwen, Journal of Engineering for Gas Turbines and Power 129 (2007), *Nonlinear Flame Transfer Function Characteristics in a Swirl-Stabilized Combustor*

[73] F.M. Berger, T. Hummel, M. Hertweck, J. Kaufmann, B. Schuermans, T. Sattelmayer, Journal of Engineering for Gas Turbines and Power 139 (2017), *High-Frequency Thermoacoustic Modulation Mechanisms in Swirl-Stabilized Gas Turbine Combustors—Part I: Experimental Investigation of Local Flame Response*

[74] J. Peterleithner, R. Basso, F. Heitmeir, J. Woisetschläger, R. Schlüßler, J. Czarske, A. Fischer, Proceedings of the ASME Turbo Expo GT2016-57485 (2016), *Comparison of Flame Transfer Functions Acquired by Chemiluminescence and Density Fluctuation*

[75] K.T. Walsh, M.B. Long, M.A. Tanoff, M.D. Smooke, Symposium on Combustion 27, 615 (1998), *Experimental and computational study of CH, CH^*, and OH^* in an axisymmetric laminar diffusion flame*

[76] K.T. Walsh, J. Fielding, M.B. Long, Optics letters 25, 457 (2000), *Effect of light-collection geometry on reconstruction errors in Abel inversions*

[77] Thomas Fiala, Thomas Sattelmayer, 5th European Conference for Aeronautics and Space Sciences (EUCASS) (2013), *A Posteriori Computation of OH^* Radiation from Numerical Simulations in Rocket Combustion Chambers*

[78] J. Floyd, P. Geipel, A.M. Kempf, Combustion and Flame 158, 376 (2011), *Computed Tomography of Chemiluminescence (CTC)*

[79] J. Floyd, A.M. Kempf, Proceedings of the Combustion Institute 33, 751 (2011), *Computed Tomography of Chemiluminescence (CTC)*

[80] K. Mohri, S. Görs, J. Schöler, A. Rittler, T. Dreier, C. Schulz, A. Kempf, Applied optics 56, 7385 (2017), *Instantaneous 3D imaging of highly turbulent flames using computed tomography of chemiluminescence*

[81] A. Unterberger, M. Röder, A. Giese, A. Al-Halbouni, A. Kempf, K. Mohri, Journal of Combustion 2018, 1 (2018), *3D Instantaneous Reconstruction of Turbulent Industrial Flames Using Computed Tomography of Chemiluminescence (CTC)*

[82] E.L. Dereniak, T.D. Dereniak, *Geometrical and Trigonometric Optics* (Cambridge University Press, Cambridge 2008)

[83] E. Hecht, *Optics* (Pearson Education Inc, Boston 2017)

[84] L. Seidel, Astronomische Nachrichten 43, 289 (1856), *Zur Dioptrik. Ueber die Entwicklung der Glieder 3ter Ordnung, welche den Weg eines ausserhalb der Ebene der Axe gelegenen Lichtstrahles durch ein System brechender Medien bestimmen*

[85] H.H. Hopkins, Proceedings of the Physical Society 58, 92 (1946), *The optical sine-condition*

[86] H. Gross, *Handbook of optical systems* (Wiley-VCH, Weinheim 2011)

[87] J. Hecht, *Understanding fiber optics* (Prentice Hall, Upper Saddle River, NJ, Columbus, Ohio, Columbus, Ohio 1999)

[88] Fujikura Ltd., *Standard Specification for Imagingfibers*

[89] F.M. Mitschke, *Fiber Optics. Physics and Technology* (Springer Berlin Heidelberg, Berlin, Heidelberg 2010)

[90] J.A. Udovich, N.D. Kirkpatrick, A. Kano, A. Tanbakuchi, U. Utzinger, A.F. Gmitro, Applied optics 47, 4560 (2008), *Spectral background and transmission characteristics of fiber optic imaging bundles*

[91] Optikos Corporation, *How to Measure MTF and other Properties of Lenses. Rev. 2.0*

[92] T. Talpur, *Fiber optic endoscopic imaging system*. Report 4.12.2013. University of Stuttgart - Institut for Applied Optics

[93] G.C. Holst, Optical Engineering 50, 52601 (2011), *Imaging system fundamentals*

[94] A. El Moussawi, *Adapting commercially available CMOS image sensors for ultraviolet chemiluminescence imaging of flames*. Master Thesis (Duisburg, Essen 2018)

[95] Cambridge in Colour, *Lens Quality: MTF, Resolution & Contrast*, https://www.cambridgeincolour.com/tutorials/lens-quality-mtf-resolution.htm

[96] L. Bergmann, C. Schaefer, H. Niedrig, H.J. Eichler, *Optik* (W. de Gruyter, Berlin, New York 1993)

[97] LaVision, *Camera Test Certificate, HS IRO*

[98] HIGH TEMP METALS, *Hastelloy X Technical Data*, http://www.hightempmetals.com/techdata/hitempHastXdata.php

[99] Ampco Metal, *Technical Data Sheet AMPCOLOY® 91 Extrusions*, https://www.ampcometal.com/documents/A91_EX_E.pdf

[100] P. Vinnemeier, *Experimental Validation of Different Resonator Designs*. Diploma Thesis (Aachen 2010)

[101] O. Lammel, H. Schütz, G. Schmitz, R. Lückerath, M. Stöhr, B. Noll, M. Aigner, M. Hase, W. Krebs, Journal of Engineering for Gas Turbines and Power 132, 329 (2010), *FLOX® Combustion at High Power Density and High Flame Temperatures*

[102] R. Lückerath, O. Lammel, M. Stöhr, I. Boxx, U. Stopper, W. Meier, B. Janus, B. Wegner, Proceedings of the ASME Turbo Expo GT2011-45790 (2011), *Experimental Investigations of Flame Stabilization of a Gas Turbine Combustor*

[103] S. Görs, *Development and Implementation of a Flame Chemiluminescence Post Processing for Industrial CFD Modeling*. Master Thesis (Aachen 2012)

[104] B. Schmidl, *Validation of advanced CFD-Combustion models for modern lean premixed burners*. Diploma Thesis (Duisburg, Essen 2011)

[105] P. Gruhlke, Mahiques, E., I., S. Dederichs, C. Beck, A.M. Kempf, Proceedings of the European Combustion Meeting (2017), *Investigation of CO and NO_x formation in a jet flame*

[106] U. Stopper, W. Meier, R. Sadanandan, M. Stöhr, M. Aigner, G. Bulat, Combustion and Flame 160, 2103 (2013), *Experimental study of industrial gas turbine flames including quantification of pressure influence on flow field, fuel/air premixing and flame shape*

[107] T. Sattelmayer, *Grundlagen der Verbrennung in stationären Gasturbinen. In: Lechner C., Seume J. (eds) Stationäre Gasturbinen. VDI-Buch.* (Springer Berlin Heidelberg 2003)

[108] B. Wegner, U. Gruschka, W. Krebs, Y. Egorov, H. Forkel, J. Ferreira, K. Aschmoneit, Proceedings of the ASME Turbo Expo GT2010-22241 (2010), *CFD Prediction of Partload CO Emissions Using a Two-Timescale Combustion Model*

[109] J. Warnatz, R.W. Dibble, U. Maas, *Combustion. Physical and Chemical Fundamentals, Modeling and Simulation, Experiments, Pollutant Formation* (Springer-Verlag Berlin Heidelberg, Berlin, Heidelberg 2006)

[110] M. Goschütz, C. Schulz, S.A. Kaiser, SAE International Journal of Engines 7, 351 (2014), *Endoscopic Imaging of Early Flame Propagation in a Near-Production Engine*

[111] N. Otsu, IEEE Transactions on Systems, Man, and Cybernetics 9, 62 (1979), *A Threshold Selection Method from Gray-Level Histograms*

[112] R.C. Gonzalez, R.E. Woods, *Digital image processing* (Pearson/Prentice Hall, Upper Saddle River, NJ 2008)

[113] T. Chanwimaluang, G. Fan, IEEE International Symposium on Circuits and Systems (2003), *An efficient blood vessel detection algorithm for retinal images using local entropy thresholding*

[114] J. Chen, B. Guan, H. Wang, X. Zhang, Y. Tang, W. Hu, IEEE Access 6, 5269 (2018), *Image Thresholding Segmentation Based on Two Dimensional Histogram Using Gray Level and Local Entropy Information*

[115] D.C.T. Nguyen, S. Benameur, M. Mignotte, F. Lavoie, Medical image analysis 48, 58 (2018), *Superpixel and multi-atlas based fusion entropic model for the segmentation of X-ray images*

[116] X. Yin, B.W.-H. Ng, J. He, Y. Zhang, D. Abbott, PloS one 9, e95943 (2014), *Accurate image analysis of the retina using hessian matrix and binarisation of thresholded entropy with application of texture mapping*

[117] C.E. Shannon, Bell System Technical Journal 27, 379 (1948), *A Mathematical Theory of Communication*

[118] T. Pun, Signal Processing 2, 223 (1980), *A new method for grey-level picture thresholding using the entropy of the histogram*

[119] J. Hao, Y. Shen, H. Xu, J. Zou, IEEE Instrumentation and Measurement Technology Conference (2009), *A Region Entropy Based Objective Evaluation Method for Image Segmentation*

[120] R.C. Gonzalez, R.E. Woods, S.L. Eddins, *Digital image processing using MATLAB* (Tata McGraw Hill Education, New Delhi 2011)

[121] C. Yan, N. Sang, T. Zhang, Pattern Recognition Letters 24, 2935 (2003), *Local entropy-based transition region extraction and thresholding*

[122] S.O. Kuznetsov, D.P. Mandal, M.K. Kundu, S.K. Pal, *Pattern Recognition and Machine Intelligence* (Springer Berlin Heidelberg, Berlin, Heidelberg 2011)

[123] H.K. Yuen, J. Princen, J. Illingworth, J. Kittler, Image and Vision Computing 8, 71 (1990), *Comparative study of Hough Transform methods for circle finding*

[124] E.R. Davies, *Machine vision. Theory, algorithms, practicalities* (Elsevier, Amsterdam, Boston 2005)

[125] T.J. Atherton, D.J. Kerbyson, Image and Vision Computing 17, 795 (1999), *Size invariant circle detection*

[126] H. Streb, B. Prade, T. Hahner, S. Hoffmann, Proceedings of the ASME Turbo Expo 2001-GT-0077, *Advanced Burner Development for the Vx4.3A Gas Turbines*

[127] B. Prade, J. Meisl, P. Berenbrink, H. Streb, S. Hoffmann, Proceedings of the ASME Turbo Expo GT2003-38442 (2003), *Burner Development for Flexible Engine Operation of the Newest Siemens Gas Turbines*

[128] *SGT5-4000F heavy-duty gas turbine (50 Hz)*, https://www.siemens-energy.com/global/en/offerings/power-generation/gas-turbines/sgt5-4000f.html (2020)

[129] J. Färber, R. Koch, H.-J. Bauer, M. Hase, W. Krebs, Journal of Engineering for Gas Turbines and Power 132, 2 (2010), *Effects of Pilot Fuel and Liner Cooling on the Flame Structure in a Full Scale Swirl-Stabilized Combustion Setup*

[130] L. Selle, Combustion and Flame 137, 489 (2004), *Compressible large eddy simulation of turbulent combustion in complex geometry on unstructured meshes*

[131] M. Fränkle, POWER-GEN Europe (2017), *Latest Developments in Siemens Large Gas Turbine Portfolio*

[132] V. Nori, J. Seitzman, 46th AIAA Aerospace Sciences Meeting and Exhibit AIAA 2008-953 (2008), *Evaluation of Chemiluminescence as a Combustion Diagnostic Under Varying Operating Conditions*

[133] T. Iijima, T. Takeno, Combustion and Flame 65, 35 (1986), *Effects of temperature and pressure on burning velocity*

[134] Y. Hardalupas, M. Orain, Combustion and Flame 139, 188 (2004), *Local measurements of the time-dependent heat release rate and equivalence ratio using chemiluminescent emission from a flame*

[135] T. Kathrotia, U. Riedel, J. Warnatz, Proceeding of the European Combustion Meeting (2009), *A numerical study on the relation of OH^*, CH^*, and $C2^*$ chemiluminescence and heat release*

[136] C. Panoutsos, Y. Hardalupas, A. Taylor, Combustion and Flame 156, 273 (2009), *Numerical evaluation of equivalence ratio measurement using OH^* and CH^* chemiluminescence in premixed and non-premixed methane–air flames*

[137] L.C. Haber, U. Vandsburger, W. Saunders, V. Khanna, Active Control Technology for Enhanced Performance Operational Capabilities of Military Aircraft, Land Vehicles and Sea Vehicles (2000), *An experimental examination of the relationship between chemiluminescenct light emissions and heat-release rate under non-adiabatic conditions*

[138] F. Güthe, B. Schuermans, Measurement Science and Technology 18, 3036 (2007), *Phase-locking in post-processing for pulsating flames*

[139] Y. Huang, V. Yang, Progress in Energy and Combustion Science 35, 293 (2009), *Dynamics and stability of lean-premixed swirl-stabilized combustion*

[140] B. Schuermans, F. Güthe, W. Mohr, Journal of Engineering for Gas Turbines and Power 132, 81501 (2010), *Optical Transfer Function Measurements for Technically Premixed Flames*

[141] K.T. Kim, J.G. Lee, H.J. Lee, B.D. Quay, D. Santavicca, Proceedings of the ASME Turbo Expo GT2009-60031 (2009), *Characterization of Forced Flame Response of Swirl-Stabilized Turbulent Lean-Premixed Flames in a Gas Turbine Combustor*

[142] B.O. Ayoola, R. Balachandran, J.H. Frank, E. Mastorakos, C.F. Kaminski, Combustion and Flame 144, 1 (2006), *Spatially resolved heat release rate measurements in turbulent premixed flames*

[143] S.A. Farhat, W.B. Ng, Y. Zhang, Fuel 84, 1760 (2005), *Chemiluminescent emission measurement of a diffusion flame jet in a loudspeaker induced standing wave*

[144] T. Fiala, T. Sattelmayer, Experiments in Fluids 56, 1 (2015), *Heat release and UV–Vis radiation in non-premixed hydrogen–oxygen flames*

[145] V.N. Nori, J.M. Seitzman, Proceedings of the Combustion Institute 32, 895 (2009), *CH^* chemiluminescence modeling for combustion diagnostics*

[146] M. Röder, T. Dreier, C. Schulz, Proceedings of the Combustion Institute 34, 3549 (2013), *Simultaneous measurement of localized heat-release with OH/CH_2O–LIF imaging and spatially integrated OH^* chemiluminescence in turbulent swirl flames*

[147] A.M. Tereza, S.P. Medvedev, V.N. Smirnov, Acta Astronautica 163, 18 (2019), *Experimental study and numerical simulation of chemiluminescence emission during the self-ignition of hydrocarbon fuels*

[148] Y. Liu, J. Tan, H. Wang, L. Lv, Acta Astronautica 154, 44 (2019), *Characterization of heat release rate by OH^* and CH^* chemiluminescence*

[149] L. He, Q. Guo, Y. Gong, F. Wang, G. Yu, Combustion and Flame 201, 12 (2019), *Investigation of OH^* chemiluminescence and heat release in laminar methane–oxygen co-flow diffusion flames*

[150] M.J. Bedard, T.L. Fuller, S. Sardeshmukh, W.E. Anderson, Combustion and Flame 213, 211 (2020), *Chemiluminescence as a diagnostic in studying combustion instability in a practical combustor*

[151] M. Lauer, T. Sattelmayer, International Symposium on Applications of Laser Techniques to Fluid Mechanics (2008), *Heat Release Calculation in a Turbulent Swirl Flame from Laser and Chemiluminescence Measurements*

[152] R.B. Randall, *Frequency analysis* (Brüel & Kjaer, Naerum 1987)

[153] J.S. Bendat, A.G. Piersol, *Random data. Analysis and measurement procedures* (Wiley, Hoboken, NJ 2010)

[154] P. Welch, IEEE Transactions on Audio and Electroacoustics 15, 70 (1967), *The use of fast Fourier transform for the estimation of power spectra: A method based on time averaging over short, modified periodograms*

[155] MathWorks, *Signal Processing Toolbox: Reference (R2021b)*, https://de.mathworks.com/help/pdf_doc/signal/signal_ref.pdf (2021)

[156] V. Sharifi, A.M. Kempf, C. Beck, AIAA Journal 57, 327 (2019), *Large-Eddy Simulation of Acoustic Flame Response to High-Frequency Transverse Excitations*

[157] T. García-Armingol, Y. Hardalupas, A. Taylor, J. Ballester, Experimental Thermal and Fluid Science 53, 93 (2014), *Effect of local flame properties on chemiluminescence-based stoichiometry measurement*

[158] T. Kathrotia, M. Fikri, M. Bozkurt, M. Hartmann, U. Riedel, C. Schulz, Combustion and Flame 157, 1261 (2010), *Study of the H+O+M reaction forming OH∗*

[159] M. Deleo, A. Saveliev, L. Kennedy, S. Zelepouga, Combustion and Flame 149, 435 (2007), *OH and CH luminescence in opposed flow methane oxy-flames*

[160] C. Kerr, P. Ivey, Measurement Science and Technology 13, 873 (2002), *An overview of the measurement errors associated with gas turbine aeroengine pyrometer systems*

[161] S.W. Allison, G.T. Gillies, Review of Scientific Instruments 68, 2615 (1997), *Remote thermometry with thermographic phosphors: Instrumentation and applications*

[162] M.D. Chambers, D.R. Clarke, Annual Review of Materials Research 39, 325 (2009), *Doped Oxides for High-Temperature Luminescence and Lifetime Thermometry*

[163] M. Aldén, A. Omrane, M. Richter, G. Särner, Progress in Energy and Combustion Science 37, 422 (2011), *Thermographic phosphors for thermometry: A survey of combustion applications*

[164] J. Brübach, C. Pflitsch, A. Dreizler, B. Atakan, Progress in Energy and Combustion Science 39, 37 (2013), *On surface temperature measurements with thermographic phosphors: A review*

[165] S. Araguás Rodríguez, T. Jelínek, J. Michálek, Á. Yáñez González, F. Schulte, C. Pilgrim, J. Feist, S.J. Skinner, Journal of the Global Power and Propulsion Society 2, S3KTGK (2018), *Accelerated thermal profiling of gas turbine components using luminescent thermal history paints*

[166] J.I. Eldridge, S.W. Allison, T.P. Jenkins, S.L. Gollub, C.A. Hall, D.G. Walker, Measurement Science and Technology 27, 125205 (2016), *Surface temperature measurements from a stator vane doublet in a turbine afterburner flame using a YAG:Tm thermographic phosphor*

[167] J.I. Eldridge, Measurement Science and Technology 29, 65206 (2018), *Single fiber temperature probe configuration using anti-Stokes luminescence from Cr:$GdAlO_3$*

[168] J. Brübach, J. Janicka, A. Dreizler, Optics and Lasers in Engineering 47, 75 (2009), *An algorithm for the characterisation of multi-exponential decay curves*

Appendix Lens Data

Lens Designs *Fujikura FIGR-30k*

10° Input Optics

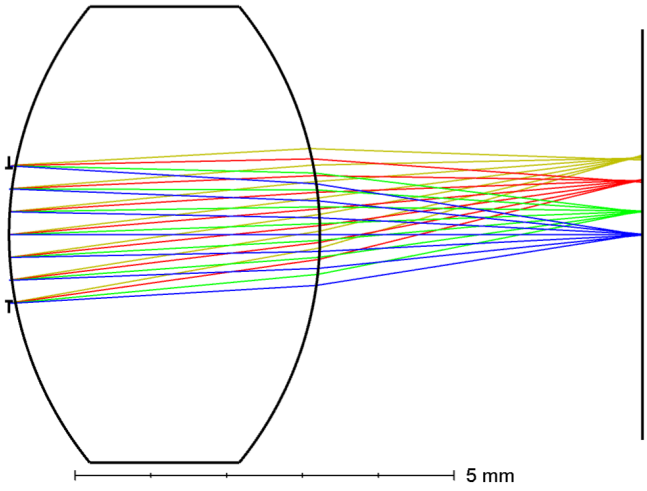

Table A.1: Design data

Surf: Type	Radius / mm	Thickness / mm	Semi-diameter / mm
OBJECT	Infinity	180.000	27.865
STOP	Infinity	0.000	0.875
2	4.760	4.100	0.977
3	−4.760	0.000	1.174
IMAGE	Infinity	4.100	0.929

10° Input Optics

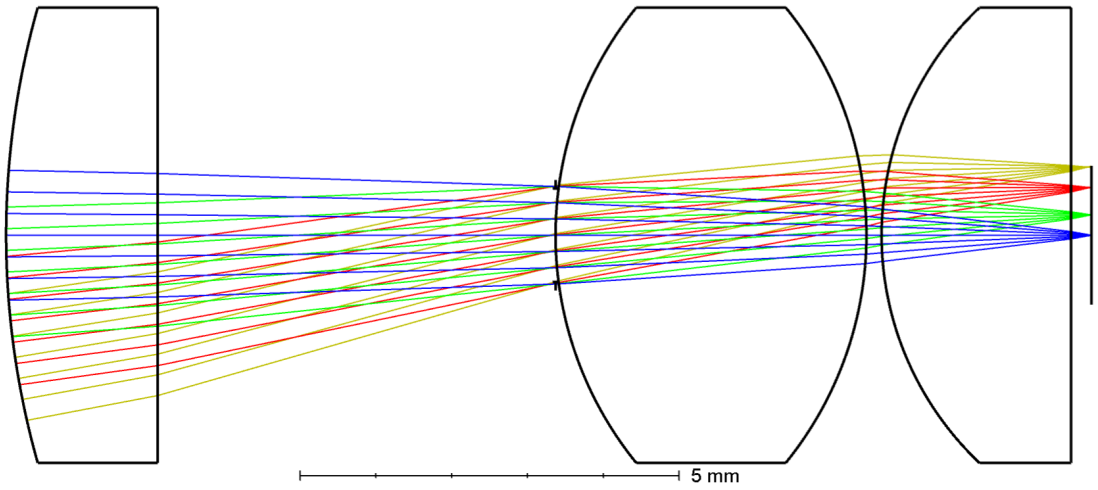

Table A.2: Design data

Surf: Type	Radius / mm	Thickness / mm	Semi-diameter / mm
OBJECT	Infinity	180.000	33.381
1	11.000	2.000	2.404
2	Infinity	5.246	2.078
STOP	Infinity	0.000	0.617
4	4.760	4.100	0.622
5	−4.760	0.200	1.022
6	4.130	2.500	1.044
7	Infinity	0.266	0.929
IMAGE	Infinity	-	0.916

25° Input Optics

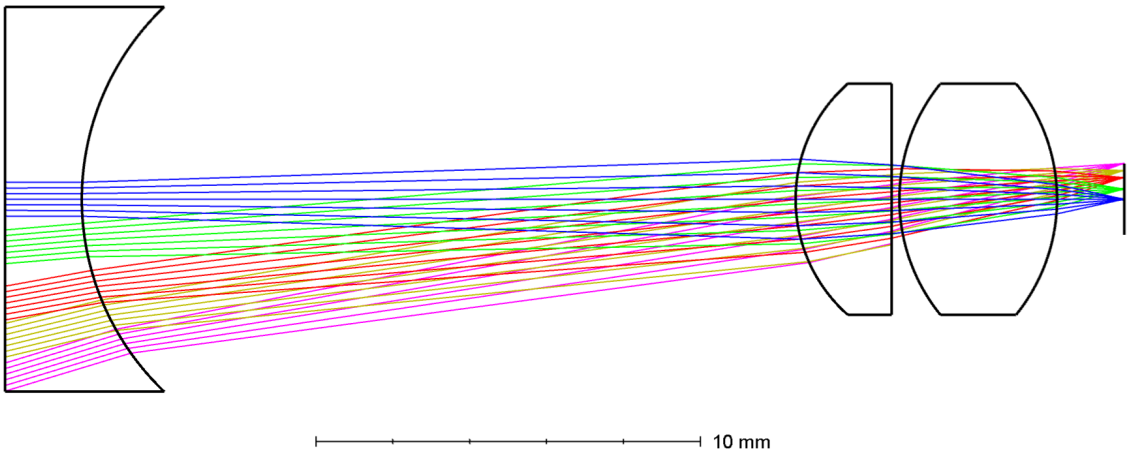

Table A.3: Design data

Surf: Type	Radius / mm	Thickness / mm	Semi-diameter / mm
OBJECT	Infinity	180.000	88.228
1	Infinity	2.000	4.050
2	6.200	18.508	4.500
STOP	4.130	2.500	3.000
4	Infinity	0.000	3.000
5	Infinity	0.370	1.315
6	4.760	4.100	3.000
7	−4.760	1.755	3.000
IMAGE	Infinity	-	0.930

40° Input Optics

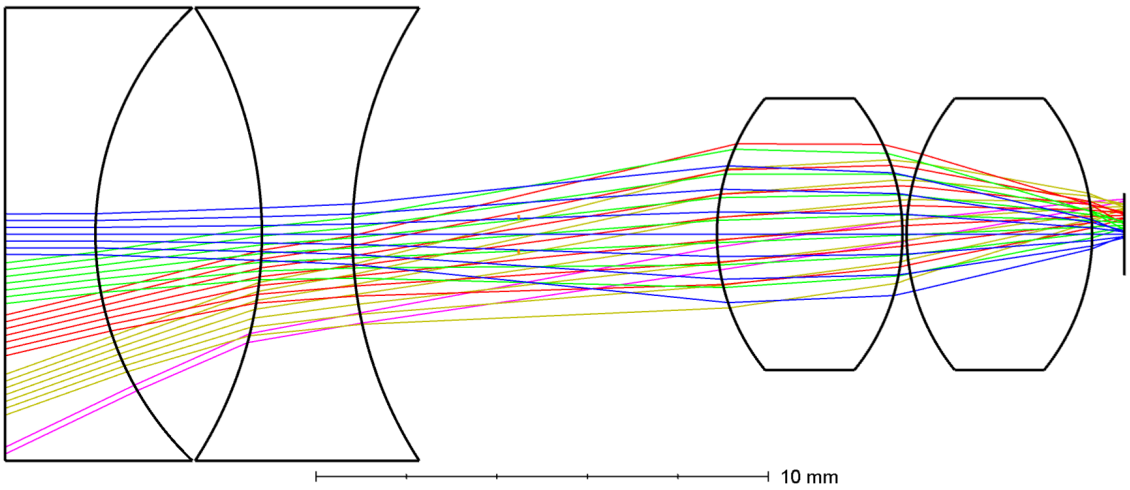

Table A.4: Design data

Surf: Type	Radius (mm)	Thickness (mm)	Semi-Diameter (mm)
OBJECT	Infinity	180.000	156.262
1	Infinity	2.000	4.501
2	6.90	3.679	3.1485
3	Infinity	2.000	1.837
4	−10.380	3.675	1.3183
5	10.380	4.380	0.362
6	4.760	4.100	2.000
7	−4.760	0.092	2.179
8	4.760	4.100	2.000
9	−4.760	0.713	1.103
IMAGE	Infinity	-	0.906

10° Output Optics

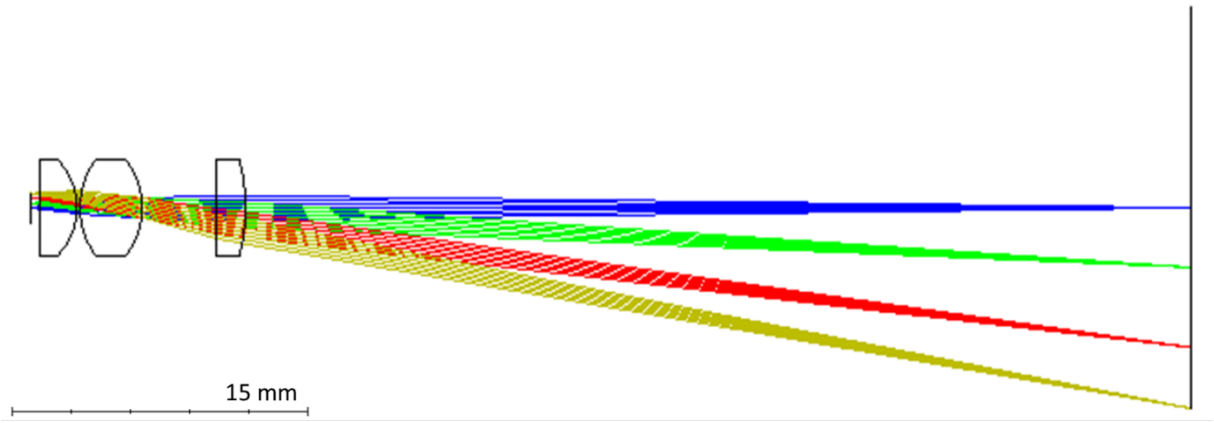

Table A.5: Design data

Surf: Type	Radius / mm	Thickness / mm	Semi-diameter / mm
OBJECT	Infinity	62.500	12.531
1	11.000	2.000	3.000
2	Infinity	4.863	3.000
STOP	Infinity	0.000	0.629
4	4.760	4.100	3.000
5	−4.760	0.200	3.000
6	4.130	2.500	3.000
7	Infinity	0.505	3.000
IMAGE	Infinity	-	0.914

Lens Designs *Nanjing 20k*

10° Input Optics

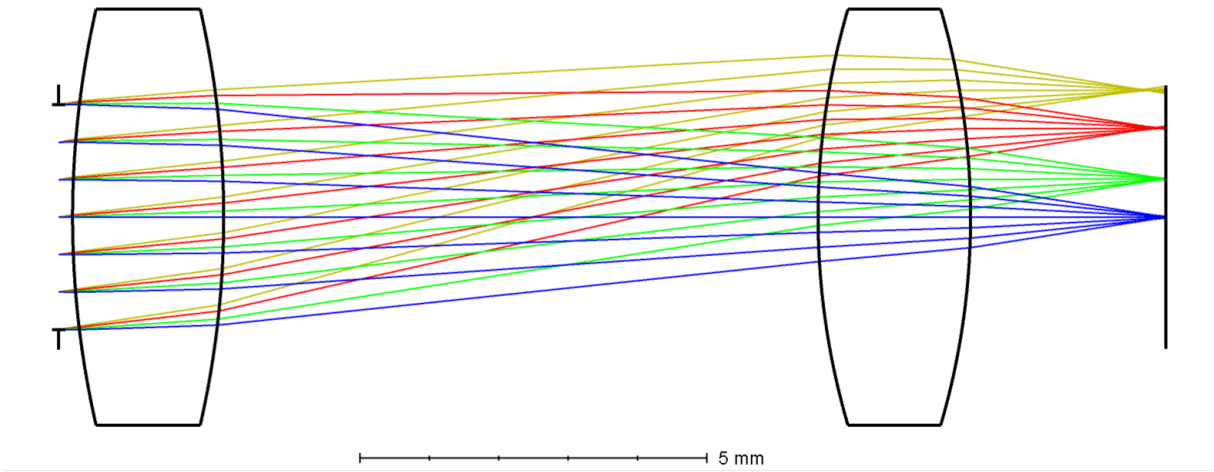

Table A.6: Design data

Surf: Type	Radius / mm	Thickness / mm	Semi-diameter / mm
OBJECT	Infinity	180.000	31.739
STOP	Infinity	0.200	1.620
2	13.440	2.180	3.000
3	−13.440	8.574	3.000
4	16.180	2.000	3.000
5	−16.180	2.818	3.000
IMAGE	Infinity	-	1.902

25° Input Optics

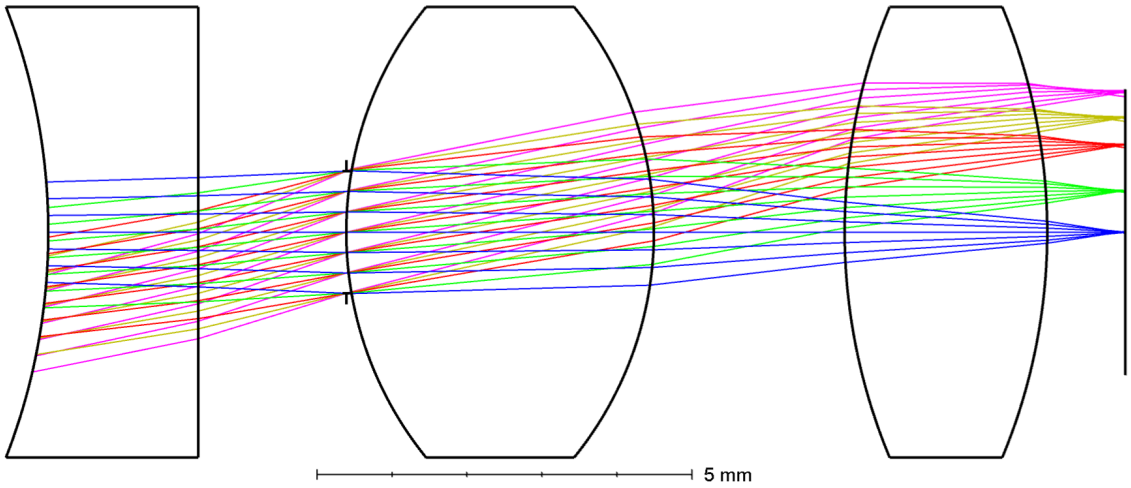

Table A.7: Design data

Surf: Type	Radius (mm)	Thickness (mm)	Semi-Diameter (mm)
OBJECT	Infinity	180.000	85.228
1	−8.250	2.000	3.000
2	Infinity	1.972	3.000
STOP	Infinity	0.000	0.813
4	4.760	4.100	3.000
5	−4.760	2.542	3.000
6	7.800	2.700	3.000
7	−7.800	1.042	3.000
IMAGE	Infinity	-	1.903

25° Output Optics

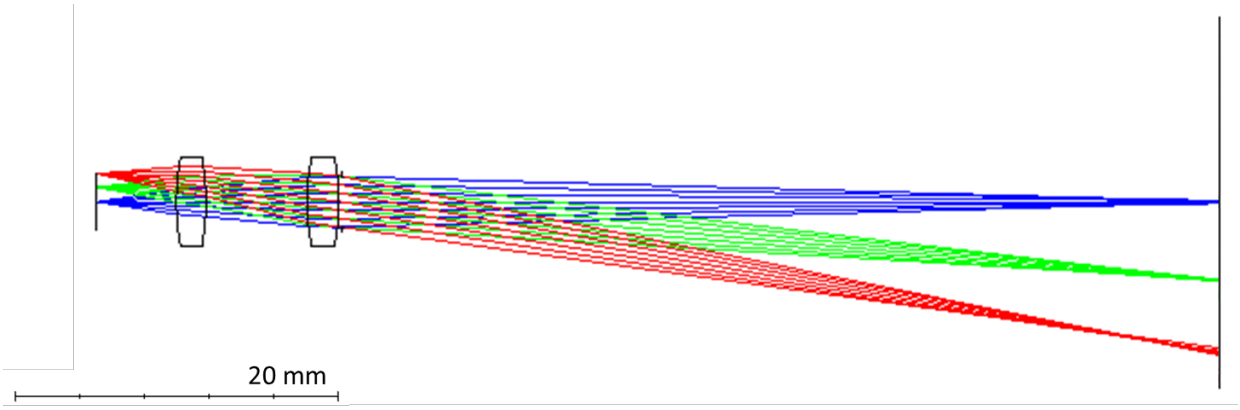

Table A.7: Design data

Surf: Type	Radius /mm	Thickness / mm	Semi-diameter / mm
OBJECT	Infinity	5.391	33.381
1	16.180	2.000	2.404
2	−16.180	6.826	2.078
3	13.440	2.180	0.617
4	−13.440	0.199	0.622
STOP	Infinity	69.99	1.022
IMAGE	Infinity	-	1.044

DOI: 10.17185/duepublico/78274
URN: urn:nbn:de:hbz:465-20230420-111625-9